RECENT DEVELOPMENT IN COMPUTATIONAL SCIENCE

Volume 6

Selected Papers from the International Symposium on Computational Science

International Symposium on Computational Science
Kanazawa University, Japan
February 2015

Editors

Veinardi Suendo
Masato Kimura
Rinovia Simanjuntak
Shinichi Miura

金沢大学
KANAZAWA UNIVERSITY

RECENT DEVELOPMENT IN COMPUTATIONAL SCIENCE

Volume 6

Selected Papers

from International Symposium

on Computational Science

International Symposium on Computational Science
Kanazawa University, Japan
February 2015

Editors

Veinardi Suendo
Masato Kimura
Rinovia Simanjuntak
Shinichi Miura

International Symposium on Computational Science 2015
17-18 February 2015, Kanazawa University, Japan

Volume Editors

- Veinardi Suendo
  Faculty of Mathematics and Natural Sciences, Bandung Institute of Technology, Indonesia
- Masato Kimura
  Faculty of Mathematics and Physics, Kanazawa University, Japan
- Rinovia Simanjuntak
  Faculty of Mathematics and Natural Sciences, Bandung Institute of Technology, Indonesia
- Shinichi Miura
  Faculty of Mathematics and Physics, Kanazawa University, Japan

ISSN 2223-0785

Published on May 31, 2015

Group Photo

February 18, 2015

CONTENTS

Simulation of The Motion of A Droplet on A Plane by The Discrete Morse Flow Method

Weerasak Dee-am[a,b]

[a] Department of Mathematics and Computer Science, Chulalongkorn University, Pathumwan, Bangkok, 10330 Thailand, E-mail: WeerasakDee@student.chula.ac.th
[b]Graduate School of Natural Science and Technology, Kanazawa University, Kakuma, Kanazawa 920-1192 Japan

Abstract. *This research concerns the simulation of the motion of a droplet on a plane. We study the film which represents the surface of the droplet [5]. The evolution of the film is described by the hyperbolic equation with the volume preservation, which means that the volume between the film and the surface where the droplet rests does not change in time. Moreover free boundary appears as a moving boundary of the drop. The hyperbolic free boundary problem under the volume preservation condition is solved by the discrete Morse flow method (DMF).*

Keywords: droplet, volume preservation, free boundary, discrete Morse flow method

1 Introduction

The model of the motion of a droplet on a plane consists of two related parts: the film of the droplet and fluid inside the film. In this work, we only study the film which represents the surface of the droplet. The crucial features of the drop are the volume preservation, free boundary and positive contact angle.

The shape of the surface of the drop can be represented by the graph of a scalar function

$$u : \Omega \times (0, T) \to (0, \infty),$$

where Ω is a domain in $\mathbb{R}^2, T$ is the positive real number and $(0, T)$ is the time interval.

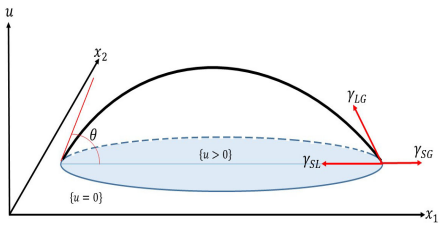

Figure 1: Droplet on a plane.

The contact angle is assumed to be small and depend on the surface tensions described by Young's equation

$$\gamma_{SG} - \gamma_{SL} = \gamma_{LG} \cos\theta.$$

where γ_{SG} is the solid surface tension,γ_{LG} is the liquid surface tension,γ_{SL} is the solid/liquid interfacial surface tension.

Furthermore, the volume preservation of the film is assumtion

$$\int_\Omega u dx = V,$$

where V is the positive constant.

This problem is solved by the discrete Morse flow method.

2 Derivation of the film equation

In this section, we derive the film equation by calculating the first variation of the action function of this phenomena. In order to define the action function, we have to consider the kinetic energy and the potential energy of this problem. For the portential energy, we consider the surface energy of the droplet which can be written as

$$E = \int_\Omega \gamma_g \sqrt{1+|\nabla u|^2}\chi_{u>0} dx + \int_\Omega \gamma_s \chi_{u>0} dx, \tag{1}$$

where $\gamma_g = \gamma_{LG}, \gamma_s = \gamma_{SL} - \gamma_{SG}, \chi_{u>0}$ the characteristic function.

By the assumtion of θ, $|\nabla u|$ remains small. So the following Taylor approximation is available

$$\sqrt{1+|\nabla u|^2} \approx 1 + \frac{1}{2}|\nabla u|^2. \tag{2}$$

Then by the approximation 2, the equation 1 can be approximated as

$$\tilde{E} = \int_\Omega \frac{\gamma_g}{2}|\nabla u|^2 dx + \int_\Omega R^2 \chi_{u>0} dx, \tag{3}$$

where $R^2 = \gamma_s + \gamma_g$.

The kenetic energy of the film given by

$$\int_\Omega \frac{\sigma}{2} u_t^2 \chi_{u>0} dx, \tag{4}$$

where σ is the area density of the surface.

Hence, the Lagrangian of this problem can be expressed as

$$L(u) = \int_\Omega (\frac{\sigma}{2} u_t^2 \chi_{u>0} - \frac{\gamma_g}{2}|\nabla u|^2 - R^2 \chi_\epsilon(u)) dx, \tag{5}$$

where χ_ϵ is the smoothing function of the characteristic function given by

$$\chi_\epsilon(u) = \begin{cases} 1, & u \geq \epsilon, \\ 0, & u \leq 0. \end{cases}$$

and $|\chi'(u)| \leq C/\epsilon$ for $u \in (0, \epsilon)$. In order to avoid the existence of the delta function, we use χ_ϵ instead of $\chi_{u>0}$ [7].

The action function within time interval $(0, T)$ can be written as

$$J(u) = \int_0^T L(u) dt \tag{6}$$

We have to seek a stationary point of the action function 6 in the following set

$$K = \{u \in H^1(\Omega \times (0,T)); u|_{\partial\Omega} = 0, \int_\Omega u\chi_{u>0}dx = V\}.$$

By assuming the existence of a stationary point, the first variation of the action function is

$$\frac{d}{d\epsilon}J(u_\epsilon)|_{\epsilon=0} = 0,$$

with using the following test function and its volume are

$$\varphi \in C_0^\infty((0,T) \times \Omega \cap \{u > 0\}), \qquad \Phi = \int_\Omega \varphi(t,x)dx.$$

and denoting

$$u_\epsilon = V\frac{u + \epsilon\varphi}{V + \epsilon\Phi}.$$

We arrive at the following equation

$$\begin{aligned} 0 &= \int_0^T \int_\Omega (\chi_{u>0}\sigma u_t\varphi_t - \gamma_g \nabla u \nabla\varphi - R^2\chi_\epsilon'(u)\varphi)dxdt \\ &+ \frac{1}{V}\int_0^T \int_\Omega (-\sigma u_t(u\Phi)_t\chi_{u>0} + \gamma_g|\nabla u|^2\Phi + R^2 u\chi_\epsilon'(u)\Phi)dxdt. \end{aligned} \tag{7}$$

Let us consider the last term on the right hand side of the equation 7, we integrate this by parts respect to time, we attain to

$$\begin{aligned} &\frac{1}{V}\int_0^T \int_\Omega (-\sigma u_t(u\Phi)_t\chi_{u>0} + \gamma_g|\nabla u|^2\Phi + R^2 u\chi_\epsilon'(u)\Phi)dxdt \\ &\quad = \frac{1}{V}\int_0^T \int_\Omega (\sigma u u_{tt}\chi_{u>0} + \gamma_g|\nabla u|^2 + R^2 u\chi_\epsilon'(u))\Phi dxdt \end{aligned}$$

By denoting the Lagrange multiplier of this problem as

$$\lambda = \frac{1}{V}\int_\Omega (\sigma u u_{tt}\chi_{u>0} + \gamma_g|\nabla u|^2 + R^2 u\chi_\epsilon'(u))dx.$$

We get the following relation

$$\int_0^T \int_\Omega (-\chi_{u>0}\sigma u_t\varphi_t + \gamma_g\nabla u\nabla\varphi + R^2\chi_\epsilon'(u)\varphi - \lambda\varphi)dxdt = 0. \tag{8}$$

The governing equation of the film is the strong from of above relation which can be expressed as

$$\chi_{u>0}\sigma u_{tt} = \gamma_g\Delta u - R^2\chi_\epsilon'(u) + \lambda, \tag{9}$$

For our problem, we consider the film equation with damping term, $\mu u_t(t,x)$, which is the resistance force acting against the vertical motion of the film. It can be represented by the speed

of the film with constant μ in [5]. By defining $\gamma = 1 + \frac{\gamma_s}{\gamma_g}$ and choosing $\sigma = 1, \gamma_g = 1$. We only consider the positive solution of the following equation with the initial and boundary conditions

$$\begin{cases} \chi_{u>0} u_{tt}(t,x) = -\mu u_t(t,x) + \Delta u(t,x) - \gamma \chi'_\epsilon(u) + \chi_{u>0}\lambda(t) \quad \text{in} \quad (0,T)\times\Omega, \\ u(t,x) = 0 \quad \text{on} \quad (0,T)\times\partial\Omega, \\ u(0,x) = u_0(x) \quad \text{in} \quad \Omega, \\ u_t(0,x) = v_0(x) \quad \text{in} \quad \Omega, \end{cases} \tag{10}$$

where $u_0(x)$ and $v_0(x)$ are the initial shape and the initial velocity, respectively, and the Lagrange multiplier is

$$\lambda = \frac{1}{V}\int_\Omega (u u_{tt} + \mu u_t u + |\nabla u|^2 + \gamma u \chi'_\epsilon(u))dx.$$

3 Discrete Morse flow method

The discrete Morse flow is the variational method used to solved the problem that dependent on time. The method was first presented to solve parabolic problem by N.Kikuchi in [6] and further applied to hyperbolic problem later in [2] and others. Moreover, it was also applied to solve the numerical solution of the free boundary problem in [1],[3] and the volume-preserving problem in [4],[5].

We fix a non negative integer $N > 0$, set the time step $h = T/N$. We seek a sequence $\{u_n\}$ by minimize the following functional for our problem see [5]

$$J_n(u) = \int_\Omega \left(\frac{|u - 2u_{n-1} + u_{n-2}|^2}{2h^2}\chi_{u>0} + \mu\frac{|u-u_{n-1}|^2}{2h} + \frac{|\nabla u|^2}{2} + \gamma\chi_\epsilon(u)\right)dx, \tag{11}$$

on the set

$$K_v = \{u \in H_0^1; \int_\Omega u\chi_{u>0}dx = V\}.$$

where the sequence $\{u_n\}$ determine by u_0 is the initial shape, $u_1 = u_0 + hv_0$ and for $n = 2, 3, 4, ...$ u_n are the minimizer of the functional 11 on the set K_v.

4 Algorithm

We can find the sequence of minimizer, $\{u_n\}$, of our functional 11 by the following algorithm

1. Given the initial shape, u_0 and initial velocity, v_0, put $u_1 = u_0 + hv_0$.
2. For $n = 1, 2, \cdots, N$, we can seek u_{n+1} as follows:
   (a) $p^1 = u_n, k = 1$.
   (b) Repeat the following.
   - search for the minimizer $\tilde{p}^{k+1}$ of J_n,
   - $p^{k+1} = \max(\tilde{p}^{k+1}, 0)$,
   - project p^{k+1} on the volume constraint hyperplane $v^{k+1} := \text{Proj}(\tilde{v}^{k+1})$,
   - if the convergence criterion is fulfilled, leave the loop, else $k = k + 1$.

   (c) $u_{n+1} = p^{k+1}$.

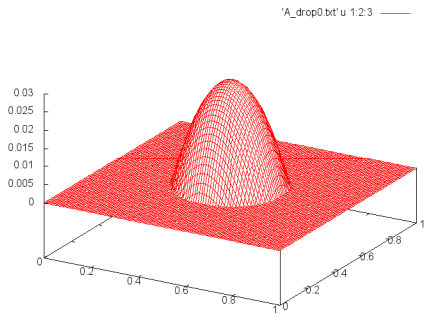

Figure 2: $t = 0$

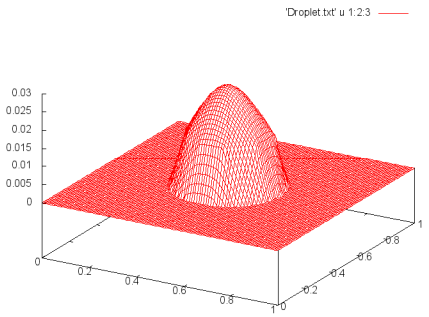

Figure 3: $t = 1$

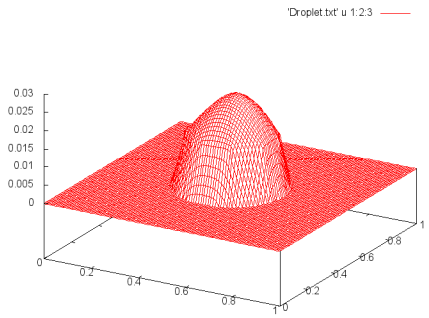

Figure 4: $t = 4$

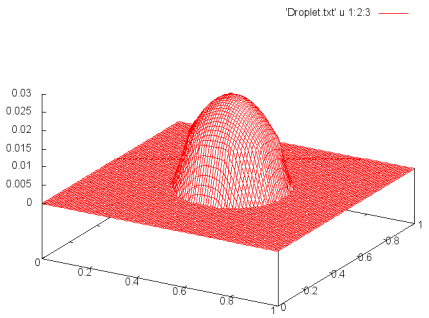

Figure 5: $t = 20$

5 Numerical approach

In this section, we use the spherical cap represented the shape of the drop for the initial shape and given the velocity of the drop into the suitable direction. By using the discrete Morse method for our problem where the radius of the drop is 0.85, the contact angle is 15°, ϵ is 0.01294 and the time step is 7.5×10^{-3} . The results is presented on above.

Acknowledgment

I would like to thank Prof. Seiro Omata and Prof. Norbert Pozar for their discussions and suggestions. This work was supported by the research grant from development and promotion of science and technology talents (DPST) and the institute for the promotion of teaching science and technology (IPST). And that it is indispensable I would like to thank my friends for their support.

References

[1] H. Imai, K. Kikuchi, K. Nakane, S. Omata, T. Tachikawa (2001). A numerical approach to the asymptotic behavior of solutions of a one-dimensional hyperbolic free boundary problem. *JJIAN*, **18**, 43 – 58.

[2] K. Hoshino, N. Kikuchi(199-). On a construction of weak solutions to linear hyperbolic partial differential systems with the higher integrable gradients. *J.Math.Sci.*, **93**, 636 – 652.

[3] K. Kikuchi, S. Omata(1999). A free boundary problem for a one dimensional hyperbolic equation. *Adv.Math.Sci.Appl*, **9**, 775 – 786.

[4] K. Svadlenka and S. Omata (2007). Construction of solutions to heat-type problems with volume constraint via the discrete Morse flow. *Funkc.Ekvac.*, **50**, 261 – 285.

[5] K. Svadlenka (2008). *Mathematical analysis and numerical computation of volume-constrained evolutionary problems, involving free boundaries.* Ph.D thesis, Kanazawa University, Japan.

[6] N. Kikuchi (1991). An approach to the construction of Morse flow for variaional functionals,in "Nematics - Mathematical and Physical Aspects", ed.: J.-M. Ghidaglia, F. Helein, *NATO Adv. Sci. Inst. Ser. C: Math.Phys.Sci.*, **332**, 775 – 786.

[7] N. T. Cong (2013). *Study of a constrained hyperbolic free boundary problem involving fluid motion based on variational approach and partical method.* Ph.D thesis, Kanazawa University, Japan.

Simulation of a Rising Oil Droplet using an Interface-Fluid Coupling

Ullul Azmy[a,b]

[a]Faculty of Mathematics and Natural Sciences, Institut Teknologi Bandung, Jl. Ganesha 10, Bandung 40132 Indonesia
[b]Graduate School of Natural Science and Technology, Kanazawa University, Kakuma, Kanazawa 920-1192 Japan
Email: ullul.azmy@hotmail.com

Abstract. *We develop a coupled interface-network and fluid model to simulate nonsymmetric triple junction motion with arbitrary surface tension in two dimension. The motion of the interface is governed by the gradient flow of a surface energy. For the numerical method, we adapt a vector valued BMO algorithm. To advance the BMO algorithm, we use a vector-type discrete Morse flow that handles the volume constraint via a penalization. Then, we add buoyancy force as an outer force to the interface model. By using this method, we simulate phenomena of a rising oil droplet in water. Lastly, we present the results of numerical experiments.*

Keywords: triple junction motion, mean curvature flow, vector-valued thresholding

1 Introduction

Triple line dynamics appears when triple line, which refers to interface of three immiscible fluids that intersect at one point, is moving due to some factors such as surface energy, fluid motion and inertial effects. Understanding the triple line dynamics is very useful to realize some kind of important motions. An example of such phenomena is the motion of a rising oil droplet. When the oil droplet rise to the water surface, the interface of three different fluids meet at a single point and adjust into the shape of triple line.

Numerical simulation of flows with moving triple line have been developed by using some methods. One of them is so-called Bence-Merriman-Osher (BMO) algorithm. Bence, Merriman, and Osher [1] introduced the original BMO method, an implicit scheme for realizing interfacial motion by mean curvature flow. Svadlenka et al. [2] reformulated the BMO algorithm in vector-valued formulation for multiphase motion. However, it is restricted to the symmetric case. Shofianah et al. [4] modified the original vector-valued BMO algorithm of [2] by generalizing the reference vectors and the way of diffusing so that it can accomodate motions for any triple of surface tensions.

In this work, we consider three evolving curves meeting at a junction and having arbitrary surface tensions. We adapt method in [4] to achieve the simulation of such a triple junction by generalizing the reference vectors.

2 Basic Model

Triple line for two dimension case is actually a triple point which is called also a triple junction. In our case, when the droplet touches the water surface, the triple junction occurs so that we have three immiscible fluids whose interfaces meet at triple junction. Thus, to get the normal velocity and the condition that has to be satisfied at triple junction, we have to consider the total surface energy of the interfaces and compute its variation.

For a fixed smooth region Ω of $\mathbb{R}^2$, we consider three evolving curves $\gamma_i(s), s \in [p_i, q_i], i = 1, 2, 3$. These curves meet the outer boundary $\partial\Omega$ at a right angle and there will be a point, called triple junction $x_T = \gamma_i(q_i), i = 1, 2, 3$, at which the curves meet. Each curve has different surface tension σ_i. Then the surface energy of all curves is given by

$$L(\gamma) = \sum_{i=1}^{3} \int_{\gamma_i} \sigma_i \mathrm{d}l = \sum_{i=1}^{3} \int_{p_i}^{q_i} |\gamma_i'(s)| \mathrm{d}s$$

From its variation, we can find the gradient flow of surface energy. For a smooth vector field $\varphi(s) = (\varphi_1, \varphi_1)$, we compute

$$\begin{aligned} \frac{d}{d\epsilon} L(\gamma + \epsilon\varphi)|_{\epsilon=0} &= \sum_{i=1}^{3} \int_{p_i}^{q_i} \sigma_i \mathbf{t}_i \cdot \frac{d}{ds}(\varphi(\gamma_i)) \mathrm{d}s \\ &= \sum_{i=1}^{3} \left(- \int_{\gamma_i} (\sigma_i \kappa_i \mathbf{n}_i) \cdot \varphi \mathrm{d}l + \sigma_i \mathbf{t}_i \cdot \varphi(x_T) \right) \end{aligned}$$

where $\mathbf{t}_i$ is the tangential vector, κ_i is curvature, and $\mathbf{n}_i$ is outer normal of γ_i with

$$\mathbf{t}_i = \frac{\gamma_i'}{|\gamma_i'|}, \kappa_i = -\frac{\gamma_{ix}' \gamma_{iy}'' - \gamma_{iy}' \gamma_{ix}''}{|\gamma_i'|^3}, \mathbf{n}_i = \frac{1}{|\gamma_i'|}(\gamma_{iy}' - \gamma_{ix}')$$

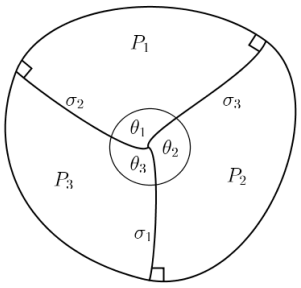

Figure 1: Triple junction

From this result, the motion by gradient flow satisfies

1. The normal velocity of interface
$$v_i = \sigma_i \kappa_i.$$
2. Condition at triple junction
$$\sum_{i=1}^{3} \sigma_i \mathbf{t}_i = 0, \tag{1}$$

The junction condition (1) is the balance of forces which is well-known to be equivalent to the Young's law

$$\frac{\sin\theta_1}{\sigma_1} = \frac{\sin\theta_2}{\sigma_2} = \frac{\sin\theta_3}{\sigma_3},$$

where θ_1, θ_2, and θ_3 are the angles at the junction (see Figure 1). By connecting this formula to the triangle as in [5], we obtain the junction angles by law of cosines:

$$\begin{aligned}\cos(\pi-\theta_1) &= \frac{\sigma_3^2+\sigma_2^2-\sigma_1^2}{2\sigma_2\sigma_3},\\ \cos(\pi-\theta_2) &= \frac{\sigma_1^2+\sigma_3^2-\sigma_2^2}{2\sigma_1\sigma_3},\\ \theta_1+\theta_2+\theta_3 &= 2\pi\end{aligned}$$

Note that as long as any given triple of surface tensions satisfies the triangle inequality, we can compute the stable angles.

3 Numerical Method

3.1 Vector-valued BMO algorithm

The BMO algorithm is a process for realizing mean curvature motion of interfaces. Originally, it takes advantage from the fact that the characteristic function of a region enclosed by an interface is evolved for a small time by the heat equation according to its mean curvature. Then, a step called *truncation* is implemeneted to obtain the new interface (given by the 1/2-level set of the diffused function). The convergence of this algorithm goes to motion by mean curvature as the short-time Δt goes to zero (see [3]).

Svadlenka et al. in [2] modified the BMO algorithm with different approach so that it can treat any number of phases in any dimension and can be extended to more general motions such motion with transport. By reformulating this algorithm into vector-type setting, then:

1. Define reference vectors $\mathbf{p}_i$, each corresponding to a phase P_i for $i = 1, 2, 3$.
2. Given regions P_i, $i = 1, 2, 3$, set $\mathbf{u}_0(x) = \mathbf{p}_i$ for $x \in P_i$.
3. Solve the vector-valued heat equation with initial condition $\mathbf{u}_0(x)$

$$\begin{aligned}\mathbf{u}_t(x,t) &= \Delta\mathbf{u}(x,t) \quad && \text{for } (t,x)\in(0,\Delta t]\times\Omega\\ \frac{\partial\mathbf{u}}{\partial\mathbf{n}} &= 0 && \text{on } (0,\Delta t]\times\partial\Omega\\ \mathbf{u}(x,0) &= \mathbf{u}_0(x) && \text{in } \Omega\end{aligned} \tag{2}$$

4. Update $\mathbf{u}_0$ by identifying the reference vector which is closest to the solution $\mathbf{u}(x, \Delta t)$ (see Figure 2 for illustration)

$$\mathbf{u}_0 = \mathbf{p}_j, \text{ where } \mathbf{p}_j\cdot\mathbf{u}(x,\Delta t) = \max_{i=0,1,\ldots,k}\mathbf{p}_i\cdot\mathbf{u}(x,\Delta t)$$

   The redistribution of reference vectors determines the configuration of each phase after time Δt.

5. Repeat from step three for the next time step until desired time.

However, this method is only related to symmetric junctions. For arbitrary junction angles, the reference vectors have to be generalized. The main ideas of the generalization were already explained in [4] and will be outlined in the following part.

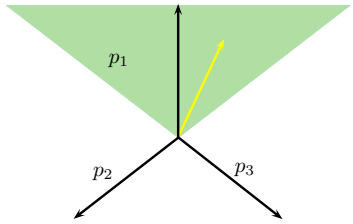

Figure 2: Reidentification of reference vector which is closest to the solution (yellow line)

3.2 Junction stability

Based on the stable configuration for triple junction that was explained in [4], we get

$$\theta_1 \mathbf{p}_1 + \theta_2 \mathbf{p}_2 + \theta_3 \mathbf{p}_3 = \mathbf{0}. \tag{3}$$

Since the reference vectors are determined up to rotation and scaling, we can choose one reference vector arbitrarily, e.g., we set $\mathbf{p}_3 = (1, 0)$. This closes system containing equation (3) and condition of $\mathbf{p}_i, i = 1, 2, 3$, whose lengths must be equal, then we get the reference vectors:

$$\mathbf{p}_1 = \left(1 - \frac{2\pi}{\theta_1\theta_3}(\pi - \theta_2), \pm\frac{2}{\theta_1\theta_3}\sqrt{\pi(\pi-\theta_1)(\pi-\theta_2)(\pi-\theta_3)}\right)$$
$$\mathbf{p}_2 = \left(1 - \frac{2\pi}{\theta_2\theta_3}(\pi - \theta_1), \mp\frac{2}{\theta_2\theta_3}\sqrt{\pi(\pi-\theta_1)(\pi-\theta_2)(\pi-\theta_3)}\right)$$

The possible choices for the sign of the second component follow from the invariance of the reference vectors with respect to flipping.

3.3 Minimizing movements

The heat equation is solved by using vector-type discrete Morse flow (DMF). For a given $N > 0$, we solve (2) by discretizing time $\Delta t = h \times N$ at each step and successively minimizing the following functionals for $n = 1, \cdots, N$ over $H^1(\Omega; R^2)$

$$J_n(\mathbf{u}) = \int_\Omega \left(\frac{|\mathbf{u} - \mathbf{u}_{n-1}|^2}{h} + |\nabla \mathbf{u}|^2\right) dx$$

The minimizers are found by conjugate gradient method.

In the volume constrained case, the minimization formulation of the vector-valued algorithm allows the inclusion of volume constraints via a penalization. In particular, instead of the functional J_n, we minimize

$$F_n(\mathbf{u}) = J_n(\mathbf{u}) + \frac{1}{\epsilon}\sum_{i=1}^{3} |V_i - \text{meas}(P_i^u)|^2,$$

where $\epsilon > 0$ is a small penalty parameter, V_i is the prescribed volume of region P_i.

For the buoyancy effect, we include the transport term to the minimization formulation as in [4], so we minimize

$$\widetilde{F}_n(\mathbf{u}) = F_n(\mathbf{u}) + \int_\Omega \frac{\boldsymbol{f}\cdot\mathbf{u}}{\sqrt{4\pi n h}},$$

where

$$\boldsymbol{f} = \begin{cases} p\dfrac{(\mathbf{p}_i\cdot\mathbf{p}_j - 1)}{|\mathbf{p}_i - \mathbf{p}_j|^2}(\mathbf{p}_i - \mathbf{p}_j), & \text{if} \quad \operatorname{dist}(x,\gamma_{ij}) < \delta_1, \\ & \qquad \operatorname{dist}(x,P_k) > \delta_2 \\ 0, \quad \text{otherwise.} \end{cases}$$

Here, $\gamma_k, (k \neq i,j)$ is the interface between phase P_i and P_j. δ_1, δ_2 are small positive constants (usually taken as several times the mesh size), p is fluid pressure, and $\mathbf{p}_i, \mathbf{p}_j$ are the BMO reference vectors.

4 Numerical Tests

Now, we present some numerical examples of the method. In this section, all numerical examples are conducted on a $[0,1]\times[0,1]$ domain with time step $\Delta t = 0.002$ and DMF partition $N = 25$. We present the behaviour of the triple junction motion for two cases (with and without axial symmetry) with types of setting as in Table 1.

Table 1: Numerical parameters for case 1 and case 2

parameter		case 1	case 2
surface tensions	σ_1	$\frac{1}{2}$	$\frac{\sqrt{2}}{2}$
	σ_2	1	1
	σ_3	$\frac{\sqrt{3}}{2}$	$\frac{\sqrt{2}}{2}$
angles	θ_1	150°	135°
	θ_2	90°	90°
	θ_3	120°	135°
reference vectors	$\boldsymbol{p}_1$	$(-0.8,-0.6)$	$(-0.777,-0.628)$
	$\boldsymbol{p}_2$	$(0,1)$	$(-0.333,-0.943)$
	$\boldsymbol{p}_3$	$(1,0)$	$(1,0)$

For examining the behaviour of the triple junction motion, we start with an initial condition where a T-shaped interface is rotated 90° counterclockwise and the T-junction is at point (0.25,0.5). We take the region that is on the left of the line $x = 0.25$ as P_2, and another top and bottom region as P_1 and P_3 respectively. Here, the domain is triangulated into uniform grid with $\Delta x = 0.00625$. Then, we investigate the evolution of the triple junction for both cases.

1. $150^\circ - 90^\circ - 120^\circ$ angle condition
   For the first case, we plot the evolution of the initial T-junction for each time as in Figure 3.

   For the first 20 time steps, the junction angles rapidly adjusts to approximate the $150^\circ - 90^\circ - 120^\circ$ angle conditions. Note that the interface move to the region with the smallest surface tension over time.

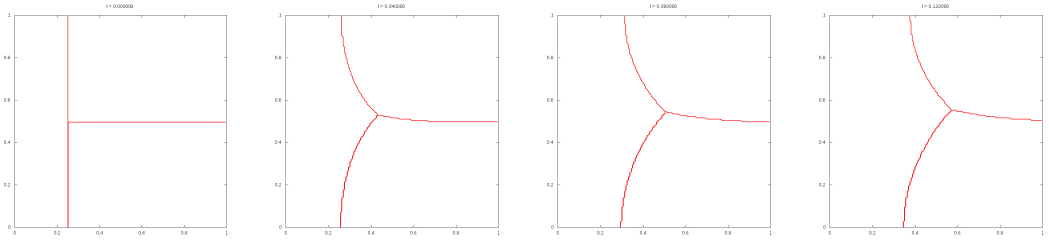

(a) $t = 0s$ (b) $t = 0.04s$ (c) $t = 0.08s$ (d) $t = 0.12s$

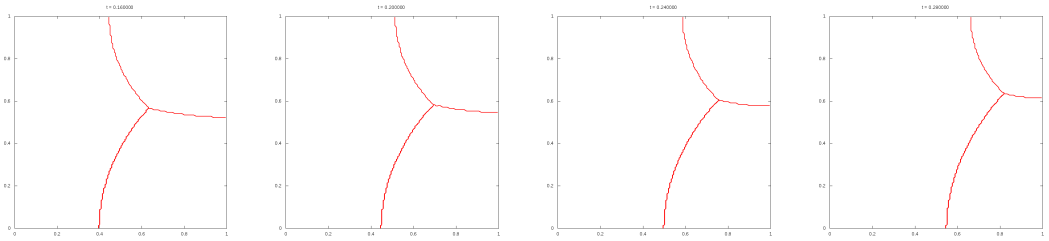

(e) $t = 0.16s$ (f) $t = 0.2s$ (g) $t = 0.24s$ (h) $t = 0.28s$

Figure 3: Evolution of triple junction for case 1

2. $135° - 90° - 135°$ angle condition
   Now we look at the behaviour of the junction motion with the parameter as on the second condition. We expect these interfaces will evolve symmetrically with respect to the horizontal line $y = 0.5$ since the surface tensions on the $1 - 2$ and $2 - 3$ interfaces are equal. This is in accordance with the numerical result shown in Figure 4.

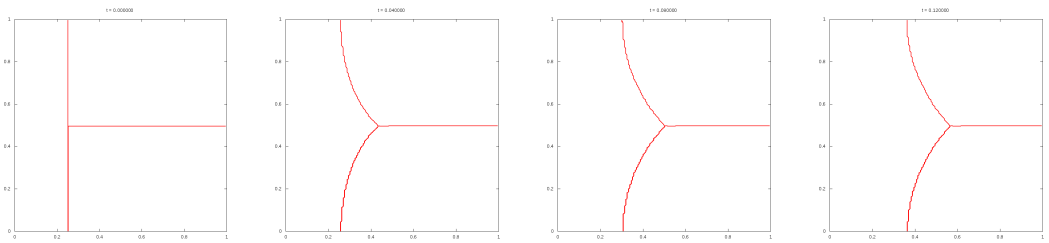

(a) $t = 0s$ (b) $t = 0.04s$ (c) $t = 0.08s$ (d) $t = 0.12s$

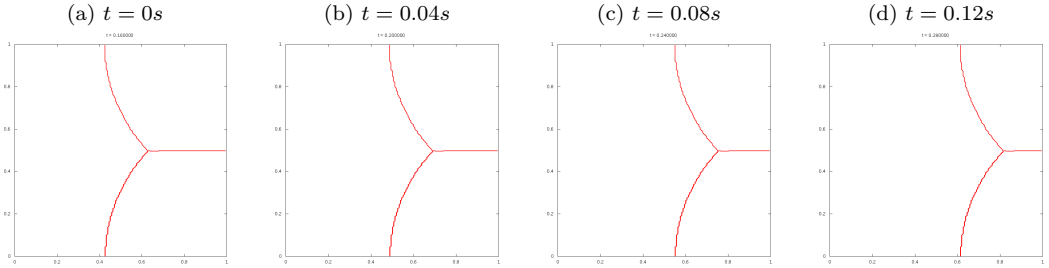

(e) $t = 0.16s$ (f) $t = 0.2s$ (g) $t = 0.24s$ (h) $t = 0.28s$

Figure 4: Evolution of triple junction for case 2

Note that the triple junction rapidly adjusts to approximate the $135° - 90° - 135°$ angle

conditions after the first 20 time steps. Afterwards, the interface gradually is begun to move horizontally to the right.

5 Conclusion

The triple junction motion with T-shaped interface as initial condition was presented. We took two cases of parameters to know the behaviour of this motion. As remarks the test, the method seems working well, so we would like to apply it for three dimensional rising droplet simulation including the buoyancy force also.

Acknowledgment

The author would like to thank to Prof. Seiro Omata and Prof. Norbert Pozar for the guidance during this research. The work of the author is financially supported by the Japanese Government (Monbukagakusho: MEXT) Scholarship Grant.

References

[1] B. Merriman, J. K. Bence, S. J. Osher (1993). Motion of multiple junctions: a level set approach. *Journal of Computational Physics*, **112**, 334-363.

[2] K. Svadlenka, E. Ginder, and S. Omata (2014). A Variational method for multiphase volume-preserving interface motions. *Journal of Computational and Applied Mathematics*, **257**, 157-179.

[3] L. Evans (1993). Convergence of an algorithm for mean curvature motion. *Indiana Univ. Math. Journals*, **42**, 533-557.

[4] N. Shofianah, R. Z. Mohammad, and K. Svadlenka (2014). On a numerical method for the simulation of contact angle dynamics, *Proceeding of Computational Engineering Conference, Vol. 19*.

[5] X. Chen, J. Guo (2007). Self-similar solution of a 2-D multi-phase curvature flow. *J. Comp. Physics*, D 229, 22-34.

A Particle Based Solver for the Three Dimensional Fluid Flow through an Elastic Porous Medium

Herlan Setiadi[ab]

[a]Faculty of Mathematics and Natural Sciences, Institut Teknologi Bandung, Jl. Ganesha 10, Bandung 40132 Indonesia
[b]Graduate School of Natural Science and Technology, Kanazawa University, Kakuma, Kanazawa 920-1192 Japan
E-mail: herlan.setiadi@students.itb.ac.id

Abstract. *Fluid flow through elastic porous medium is an interesting and complex problem in fluid dynamics. Its complexity arises due to the necessity to take into account both the stress and the strain in the structure of the elastic solid as it interacts with the fluid. In our work, we simulate this phenomenon by using the Smoothed Particle Hydrodynamics (SPH) method. In the SPH method, the fluid and the elastic solid are represented using particles in the Lagrangian frame. We compare various formulations of the interaction between the fluid an the elastic solid on a few test cases, and we present the results of our simulations.*

Keywords: Smoothed Particle Hydrodynamics, Elastic solid, Fluid-structure interaction, Porous medium

1 Introduction

Fluid flow through an elastic porous medium is an interesting topic encountered in many research fields of science and engineering. It has many application such as filtration process, blood vessel, reservoir characterization, etc. Here we want to investigate the phenomenon with a simple model of the sponge.

We try to simulate the fluid pass through the porous of the solid body. The position of the fluid is on the top of the solid body. The fluid goes down because of the gravitation (body force). The deformation of the elastic solid (sponge) occurred due to action of the fluid. We consider the fluid-structure interaction to model the action of the fluid to the solid body, vice versa.

In addition, we simulate this phenomenon by using Smoothed Particle Hydrodynamics (SPH) method. SPH is a meshless Lagrangian particle method to obtain numerical solutions of the fluid dynamics equations. The method was introduced in [5] to solve an astrophysical problem. Recently, the SPH method was developed in many application in computational fluid dynamics. We give a brief introduction about the basic SPH method in this paper.

Moreover, we model the case with different parameter discretization and size of pore radius of the sponge. It will show us the robustness of our method to solve this problem.

2 Governing Equations

We consider the governing equations of the motion of the fluid and solid body in isothermal condition. It consists of continuity and momentum equation.

2.1 Continuity equation

We use the continuity equation in Lagrangian framework. It can be written as,

$$\frac{D\rho}{Dt} + \rho\left(\nabla \cdot \mathbf{v}\right) = 0 \tag{1}$$

where ρ is density, t is time, $\mathbf{v}$ is the velocity. Here $\frac{D}{Dt}$ is a material derivative. It is equal to $\frac{\partial}{\partial t} + (\mathbf{v} \cdot \nabla)$. The last term in material derivative is called a convection derivative part. This equation guarantee the mass conservation.

2.2 Momentum equation

The governing equation of momentum equation or the equation of motion can be written as,

$$\rho\frac{D\mathbf{v}}{Dt} = \nabla \cdot \sigma + \rho\mathbf{g} \tag{2}$$

where σ is the Cauchy stress tensor. It consists of pressure and deviatoric stress tensor. The last term in equation (2) is body force term. The body force that we use in this case is gravitational force.

2.2.1 Momentum equation of the fluid

Since we model the motion of the incompressible Newtonian fluid, the equation (2) can be shown as,

$$\rho_f\frac{D\mathbf{v}_f}{Dt} = -\nabla p_f + \eta\Delta\mathbf{v}_f + \rho_f\mathbf{g}_f \tag{3}$$

where p_f and η denote the pressure and the dynamic viscosity. Note $(.)_f$ represents the physical quantity of the fluid. The term ∇p_f is pressure gradient term and the $\eta\Delta\mathbf{v}_f$ is dissipation or viscosity term.

2.2.2 Momentum equation of the solid body

The motion of the solid body is described by the following equation,

$$\rho_f\frac{D\mathbf{v}_s}{Dt} = -\nabla p_s + \nabla \cdot \mathbf{S}_s + \rho_s\mathbf{g}_s \tag{4}$$

where $\mathbf{S}_s$ is deviatoric stress tensor. Note $(.)_s$ represents the physical quantity of the solid body. This equation is obtained by the stress tensor decomposition into its isotropic and deviatoric parts:

$$\sigma^{ij} = -p_s\delta^{ij} + S_s^{ij}$$

from the equation (2). In [3] Monaghan proposed the following equation to compute the rate change of deviatoric stress,

$$\frac{DS_s^{ij}}{Dt} = 2G_s\left(\dot{\epsilon}_s^{ij} - \frac{1}{3}\delta^{ij}\dot{\epsilon}_s^{ij}\right) + \sum_k S_s^{ik}\Omega_s^{jk} + \Omega_s^{ik}S_s^{kj} \tag{5}$$

where

$$\dot{\epsilon}_s^{ij} = \frac{1}{2}\left(\frac{\partial v_s^i}{\partial x_s^j} + \frac{\partial v_s^j}{\partial x_s^i}\right) \tag{6}$$

is the rate of deformation tensor

$$\Omega_s^{ij} = \frac{1}{2}\left(\frac{\partial v_s^i}{\partial x_s^j} - \frac{\partial v_s^j}{\partial x_s^i}\right) \tag{7}$$

is the spin tensor. Then, we use the equation of state to obtain pressure in the fluid and the solid body,

$$p = \frac{\rho_0 c^2}{\gamma}\left(\left(\frac{\rho}{\rho_0}\right)^{\gamma} - 1\right) \tag{8}$$

where ρ_0 is the reference density, c is the speed of sound, and γ is a constant parameter.

3 Numerical Methods

3.1 Basic of SPH method

SPH approximate the Dirac delta function in an integral representation of a function by a smoothing function $W^h(d)$,

$$f(\mathbf{r}) = \int_\Omega f(\mathbf{r}')W^h(d)d\Omega(\mathbf{r}') \tag{9}$$

for

$$d = \|\mathbf{r} - \mathbf{r}'\|$$

where f is the function of a position vector, h is the length of the smoothing function, and $d\Omega(\mathbf{r}')$ represents a finite control volume in three dimensional space.

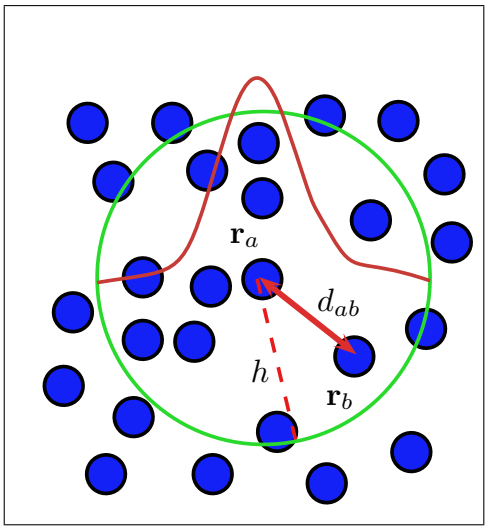

Figure 1: Two dimensional ilustration of a smoothing function over a support domain

By using SPH particle approximation, we substitute the finite control volume $d\Omega(\mathbf{r}')$ with the particle $\frac{m_b}{\rho_b}$, the equation (9) can be written as,

$$f(\mathbf{r}_a) = \sum_b \frac{m_b}{\rho_b} f(\mathbf{r}_b)W^h(d_{ab}) \tag{10}$$

The quantity of the smoothing function depend on the distance between the particles d_{ab}. m_b and ρ_b denote mass and density of each particle. The illustration can be shown in figure 1. More details about the SPH method can be found in [2] and [4].

3.2 Approximation of governing equations by SPH method

The SPH approximation of the continuity equation (1) for fluid and solid particles is,

$$\frac{D\rho_a}{Dt} = \sum_b m_b \mathbf{v}_{ab} \cdot \nabla_a W_{ab} \tag{11}$$

By using this equation we can update the density of each particle. This equation shows that the time rate of density change of each particle is proportional to the relative velocities between the center particle a and its neighbour particles b.

According to the equation (3), the SPH approximation for the material derivative of the velocity of particle a is,

$$\frac{Dv_a^i}{Dt} = -\sum_{b\in\Omega_f} m_b \left(\frac{p_a}{\rho_a^2} + \frac{p_b}{\rho_b^2}\right) \nabla_a W_{ab} + \frac{\eta}{\rho_a} \sum_{b\in\Omega_f} m_b \mathbf{v}_{ab} \nabla_a^2 W_{ab} + \mathbf{g} \tag{12}$$

where

$$W_{ab} = W^h(d_{ab}) \qquad \text{and} \qquad \mathbf{v}_{ab} = \mathbf{v}_a - \mathbf{v}_b$$

The summation of the equation (12) is just for the fluid particles Ω_f. This symmetric formulation satisfies the action-reaction principle between the center particle a and particle b. To compute the pressure gradient term we use smoothing function which has been proposed by [6],

$$W^h_{spiky}(d) = \frac{15}{\pi h^6} \begin{cases} (h-d)^3, & \text{if} \quad 0 \le d \le h \\ 0, & \text{otherwise} \end{cases} \tag{13}$$

It is called spiky kernel. The gradient of this kernel will not vanish near the center. The kernel can generates the repulsive force if the particles get too close to each other when we compute the pressure gradient term[7].

To compute the viscosity term in equation (12) we use use this following smoothing function which has been introduced by [7],

$$W^h_{viscosity}(d) = \frac{15}{2\pi h^3} \begin{cases} -\frac{d^3}{2h^3} + \frac{d^2}{h^2} + \frac{h}{2d} - 1, & \text{if} \quad 0 \le d \le h \\ 0, & \text{otherwise} \end{cases} \tag{14}$$

The SPH approximation of the momentum equation (4) of the solid particle a, which yields

$$\frac{Dv_a^i}{Dt} = \sum_{b\in\Omega_s} m_b \sum_j \left(\frac{\sigma_a^{ij}}{\rho_a^2} + \frac{\sigma_b^{ij}}{\rho_b^2} + \Pi_{ab}\delta^{ij} + \left(\frac{R_a^{ij}}{\rho_a^2} + \frac{R_b^{ij}}{\rho_b^2}\right) f_{ab}^n\right) \frac{\partial W_{ab}}{\partial x_a^j} + \mathbf{g} \tag{15}$$

The summation of the equation (15) is just for the solid particles Ω_s. The term $\Pi_{ab}\delta^{ij}$ is a dissipation term which has been proposed by [1]. It is used to remove velocity oscillations and prevent unphysical penetration when the particles get too close each other in the SPH method. We compute the dissipation term by using the following equation,

$$\Pi_{ab} = \begin{cases} \frac{\alpha c_0 \mu_{ab}}{\rho_{ab}}, & \text{if} \quad \mu_{ab} < 0 \\ 0, & \text{otherwise} \end{cases} \tag{16}$$

$$\mu_{ab} = \frac{h(\mathbf{v}_a - \mathbf{v}_b) \cdot (\mathbf{r}_a - \mathbf{r}_b)}{d_{ab}^2 + (0.1h)^2}$$

In [3], Monaghan proposed artificial stress to removes tensile instability in the SPH method. Tensile instability is the clustering phenomenon that can be happened when the solid particles is stretched each other. The idea is by adding the repulsive force in terms of the kernel function and the stress tensor when the particles in tensile stress condition. We obtain the artificial stress by these following equations,

$$R_a^{ij} = -\varepsilon \begin{cases} \sigma_a^{ij}, & \text{if} \quad \sigma_a^{ij} > 0 \\ 0, & \text{otherwise} \end{cases} \tag{17}$$

and

$$f_{ab} = \frac{W^h(d_{ab})}{W^h(\Delta s)} \tag{18}$$

is the repulsive force which increases as the distance decreases and Δs is initial distance between solid particles.

We use the XSPH velocity correction from [4] to compute the strain tensor $\dot{\epsilon}$ and the spin tensor Ω^{ij} in RHS of (5) and (11). The equation is given by

$$\hat{\mathbf{v}}_a = \mathbf{v}_a + 0.5 \sum_{b \in \Omega_s} \frac{m_b}{\bar{\rho}_{ab}} \mathbf{v}_{ba} W_{ab} \tag{19}$$

When compute velocity correction in (19), we use a smoothing function from [3],

$$W_{poly6}^h(d) = \frac{315}{64\pi h^9} \begin{cases} (h^2 - d^2)^3, & \text{if} \quad 0 \leq d \leq h \\ 0, & \text{otherwise} \end{cases} \tag{20}$$

Then to obtain the velocity gradient of the particle in the equation (6) and (7) is given by

$$\frac{\partial \hat{v}_a^i}{\partial x_a^j} = -\sum_{b \in \Omega_s} \frac{m_b}{\rho_b} \hat{v}_{ab}^i \frac{\partial W_{ab}}{\partial x_a^j} \tag{21}$$

3.3 Fluid-structure interaction

To solve FSI problem, Antoci in [1] considered the shape of the solid body to compute the pressure gradient. The results satisfy the experimental data. But it can be a big problem if the method deals with a complex shape and deformation of the solid body.

However, we model the interaction between the fluid and the solid particles by using the SPH approximation of the continuity and the momentum equation of the fluid particles. The FSI problem is modeled by using these following rules:

- treat the solid particles as the fluid particles when we update the density of the fluid particles, vice versa

$$\frac{d\rho_a}{dt} = \sum_b m_b \mathbf{v}_{ab} \cdot \nabla_a W_{ab} \tag{22}$$

- treat the solid particles as the fluid particles when we compute the force exerted on the fluid particles due to the solid particles,

$$\mathbf{f}_{a(s \to f)} = -\sum_{b \in \Omega_s} m_b \rho_b \left(\frac{p_a}{\rho_a^2} + \frac{p_b}{\rho_b^2} \right) \nabla_a W_{ab} + \eta \sum_{b \in \Omega_s} m_b \mathbf{v}_{ba} \nabla_a^2 W_{ab} \tag{23}$$

- add repulsive force which has been introduced by [8] to the equation (22),

$$\mathbf{f}_{a_{repulsive}} = K_f \sum_{b \in \Omega_s} \frac{m_a m_b}{\rho_a \rho_b} \nabla_a W_{ab} \tag{24}$$

- The force exerted on the solid particles due to the fluid particles is obtained by this rule,

$$\mathbf{f}_{a(f \to s)} = -\mathbf{f}_{a(s \to f)} \tag{25}$$

In [9], Amini et al. modified the repulsive force of (24) because he used the cubic spline kernel. The gradient of the kernel will vanish near the center. Since we use the kernel which has non zero value near the center, we do not have to modified the repulsive force in (24).

4 Implementations of the SPH method and discussions

The position of the fluid is on the top of the solid body (sponge). The initial distance between the bottom of the fluid particles and the top of the solid particles is 0.0045m. The thickness of the sponge is 0.004m. It is attached to right and left side of the wall. The gravitation (g=9.8m/s) is applied to all particles.

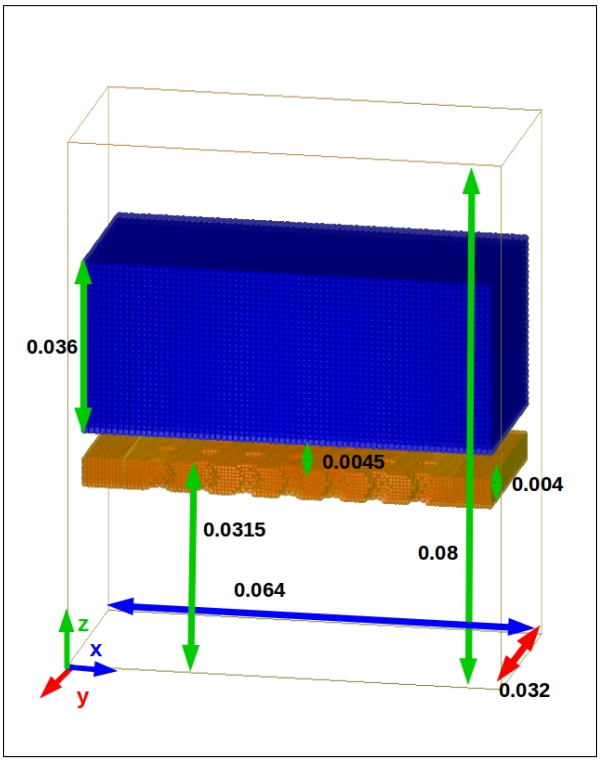

Figure 2: Geometry of the simulation

Water is used as the fluid with density $\rho_f = 1000\text{kg/m}^3$. The small sound speed of the water is chosen c_f=30m/s and dynamic viscosity of the water is η=3.5x10^{-3}kg/ms. The dimension of the water as shown in figure 2.

The sponge is modeled with density $\rho_s = 950\text{kg/m}^3$. The small sound speed of the sponge is chosen c_s=31.6m/s. Also the shear modulus G_s=2x10^{-6}N/m^2. The shape of the pore as shown in figure 3.

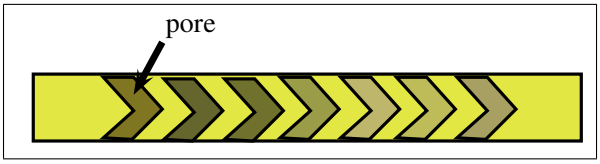

Figure 3: Side view of the sponge

There are two kind of the simulations in this paper. The first one, we try to simulate the case with different ratio of the pore radius r_{pore} to kernel length h. The top view of the sponge as shown in figure 4. The other one, we try to simulate the case with different kernel length but same size of the pore.

4.1 The case with different size of the pore radius

We use the ratio of the pore radius to the length kernel to set the different size of the sponge pore. There are four value for the ratio including 0.5, 1, 1.5 and 2. Each sponge has the regular size of the pore and identical number of the porous. The parameter of the sponge is setted equal for every simulation in this case. Then, we compare the average displacement of the solid particles each time interval between the sponges.

The length of the kernel function h=0.001, the distance between fluid particles d_{fluid}=8x10^{-4} and solid particles d_{solid}=5x10^{-4} are chosen. Also, the number particles for the fluid n_{fluid}=68231 and the solid n_{solid}: 43696 (r_{pore}=0.5h), 41533 (r_{pore}=h), 37978 (r_{pore}=1.5h), and 33160 (r_{pore}=2h). The time interval Δt=10^{-5}s is adopted.

We obtain the average displacement dis_{avg} of the solid particles of the sponge at certain time t by using the following equation,

$$dis_{avg} = \frac{1}{N}\sum_{i=1}^{N}(r_i - r_0)$$

where N is the number of solid particles, r_i is the position of the solid particle at time t and r_0 is the position of the solid particle at initial position. The results as shown in figure 5. The largest

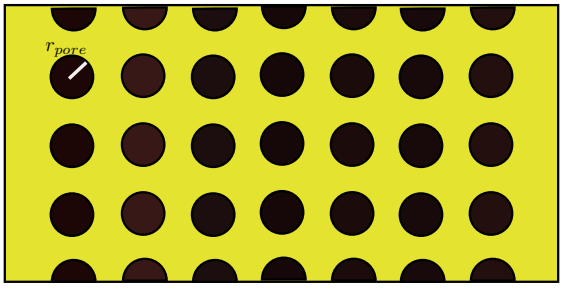

Figure 4: An illustration of the sponge from the top

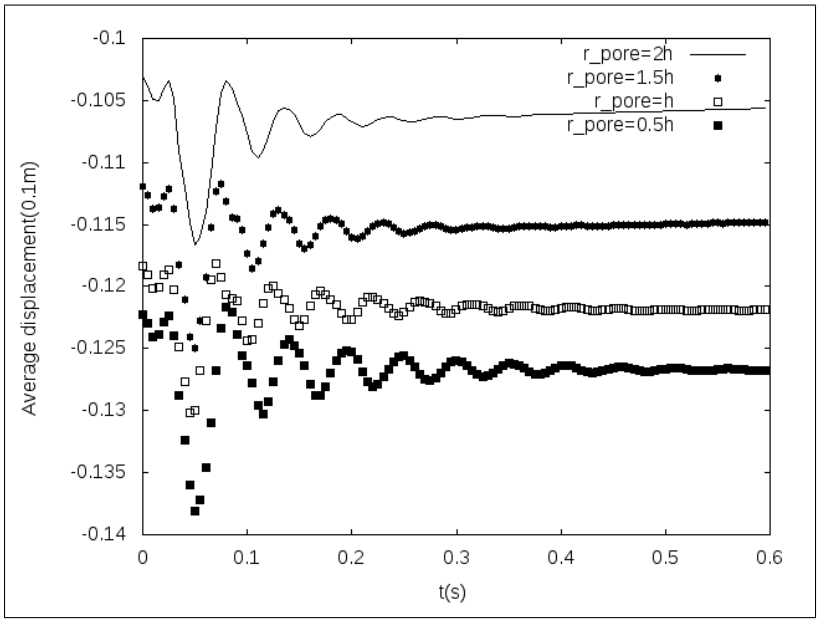

Figure 5: The displacement of the solid particles relative to its initial position for different size of pore radius

average displacement of the solid particles is the sponge with the size of pore radius equal to $0.5h$. The smallest average displacement of the solid particles is the sponge with the size of pore equal to $2h$. The different results is because the fluid which pass through the pore of the sponge r_{pore}=$2h$ is easier than the pore of the sponge which smaller than $2h$.

In addition, we can see the figure 6 as the explanation of the results. At the beginning t=0s the amount of the fluid is equal each case. At t=0.05s the solid particles is stretched because of the force from the fluid particles. The amount of the solid particles which passed through the solid particles for r_{pore}=$2h$ is greater than r_{pore}=$1.5h$ at t=0.075s. Moreover, at t=0.1s the strain of the sponge r_{pore}=$1.5h$ is greater than the sponge r_{pore}=$2h$.

Hence, we conclude that the result for this case depends on the ratio of the kernel length to the radius of pore.

4.2 The case with different length of the kernel

In this case, we want to test the robustness of our method. A robustness requirement aims to ensure that the method does not depend on the discretization parameter h. The physical parameter that we use same as the first case with r_{pore}=0.0015m. The different with the first case is just we only change the kernel length. The value of h=0.0013, 0.0012, 0.0011, and 0.001m are adopted.

In Figure 7 shows the average displacement of the solid particles relative to its initial position. It can be seen the results at time 0 until 0.15 seconds is quietly similar. But at time 0.15 until 0.5 seconds the displacement of some sponges are different.

Our FSI method depends on the repulsive force parameter in (24). Here, we fix the value of $K_f = 10^8$. To get the best results we have to adjust the parameter K_f in terms of h.

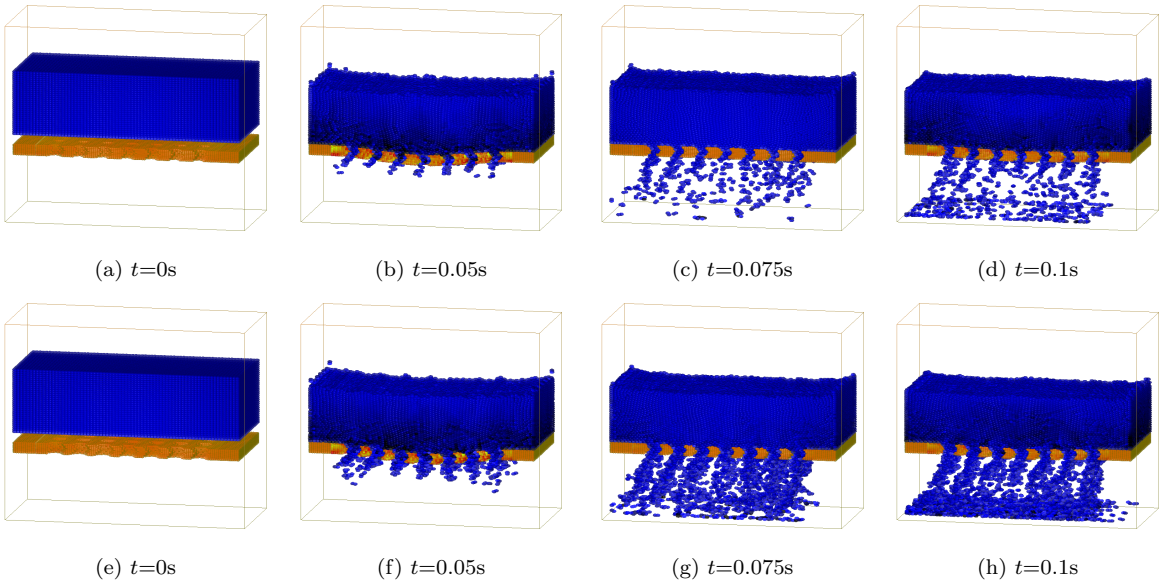

(a) t=0s (b) t=0.05s (c) t=0.075s (d) t=0.1s

(e) t=0s (f) t=0.05s (g) t=0.075s (h) t=0.1s

Figure 6: The snapshots of the simulations for r_{pore}=1.5h (a-d) and r_{pore}=2h (e-h)

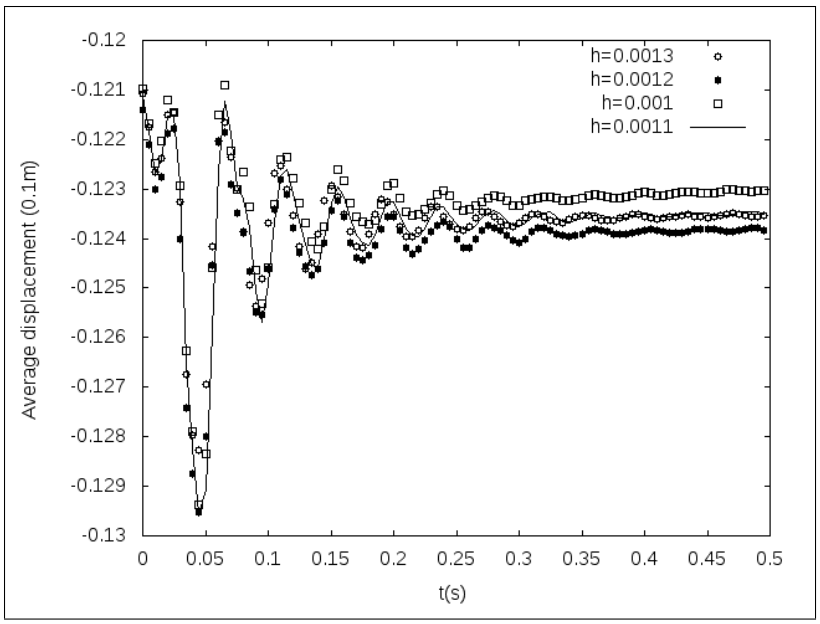

Figure 7: The displacement of the solid particles relative to its initial position for different length of h

5 Conclusions

We have presented SPH method for the fluid flow simulation through porous medium with various radius of pore. In addition our method to simulate fluid-structure interaction and deformation of the elastic solid (sponge) due to action of the fluid has been proposed. We should investigate the relation between K_f and h to achieve the robustness of our method. In future work, the fluid-structure interaction method can be extend to simulate the multi-phase flow through porous medium (e.g. oil-filled pores), solidification process, etc.

Acknowledgment

I would like to thank Prof. Seiro Omata and Prof. Norbert Pozar for the discussion about this research in Kanazawa University. Financial support from JASSO is acknowledged.

References

[1] C. Antoci, M. Gallati, and S. Sibilla (2007). Numerical simulation of fluid-structure interaction by SPH. *J. Comp. Struc.*, **85**, 879 – 890.

[2] J.J. Monaghan (1992). Smoothed particle hydrodynamics. *Annu. Rev. Astron. Astrophys.*, **30**, 543 – 574.

[3] J.J. Monaghan (2000). SPH without a tensile instability. *J. Comp. Phys.*, **159**, 290 – 311.

[4] J.J. Monaghan (2005). Smoothed particle hydrodynamics. *Rep. Progr. Phys.*, **68**, 1703 – 1759.

[5] L.B. Lucy (1977). A numerical approach to the testing of the fission hypothesis. *Astron. J.*, **82**, 1013 – 1024.

[6] M. Desbrun and M. P. Cani (1996). Smoothed particles: A new paradigm for animating highly deformable bodies. *Proceeding of EG Workshop on Animation and Simulation*, 61 – 76.

[7] M. Muller, D. Charypar, and M. Gross (2003). Particle-based fluid simulation for interactive applications. *Proceeding of ACM SIGGRAPH Symposium on Computer Animation*, 154 – 159.

[8] R. Vignjevic, T. De Vuyst, and J. Campbell (2002). The use of an homogeneous repulsive force for contact treatment in SPH, WCCM V, Fifth world congress of comp. mech., Vienna, Austria, 7 – 12.

[9] Y. Amini, H. Emdad, and M. Farid (2011). A new model to solve fluid-hypo-elastic solid interaction using the smoothed particle hydrodynamics (SPH) method. *European J. Mech. B/Fluids*, **30**, 1984 – 1994.

Simulation of A Soap Film Catenoid

Pornchanit Subvilai[a,b]

[a]Graduate School of Natural Science and Technology, Kanazawa University, Kakuma, Kanazawa 920-1192 Japan
[b]Department of Mathematics, Faculty of Science, Chulalongkorn University, Pathumwan, Bangkok 10330 Thailand
E-mail: hippoarale@gmail.com

Abstract. *There are many interesting phenomena concerning soap film. One of them is the soap film catenoid. The catenoid is the equilibrium shape of the soap film that is stretched between two circular rings. When the two rings move farther apart, the radius of the neck of the soap film will decrease until it reaches zero and the soap film is split. In our simulation, we show the evolution of the soap film when the rings move apart before the film splits. We use the BMO algorithm for the evolution of a surface accelerated by the mean curvature.*

Keywords: soap film catenoid, minimal surface, hyperbolic mean curvature flow, BMO algorithm

1. Introduction

The phenomena that concern soap bubble and soap films are very interesting. For example when soap bubbles are blown with any shape of bubble blowers, the soap bubbles will be round to be a minimal surface that is the minimized surface area. One of them that we are interested in is a soap film catenoid. The catenoid is the minimal surface and the equilibrium shape of the soap film stretched between two circular rings.

In the observation of the behaviour of the soap bubble catenoid [3], if two rings move farther apart, the radius of the neck of the soap film will decrease until it reaches zero. Then the soap film is split and a small bubble will appear.

In this simulation, the soap film catenoid was simulated when the rings move apart before the film split by adapting BMO algorithm for the evolution of a surface accelerated by the mean curvature.

2. Derivation of the equation

When the force act to the interface in the normal direction, the equation of interfacial dynamics [2] is given by

$$A = -\kappa n, \tag{1}$$

where A is the interfacial normal acceleration, κ is the mean curvature, and n is the unit normal vector to the interface.

The differential equation for the evolution (1) is

$$\begin{cases} \alpha_{tt}(t,x) \;=\; -\kappa(x) & \text{in } (0,T) \;\times\; \Omega \\ \alpha_t(t=0,x) \;=\; v_0(x) & \text{in } \Omega \\ \alpha(t=0,x) \;=\; \gamma(x) & \text{in } \Omega, \end{cases}$$

where α is a position function, v_0 is an initial velocity and γ is a parametrized curve.

3. BMO algorithm for the evolution of a surface accelerated by the mean curvature

The original BMO was proposed by Bence, Merriman, and Osher in [1]. The BMO is useful for computing motion of a soap film by mean curvature. In this paper, we use the idea of BMO for the evolution of a surface accelerated by the mean curvature [2] because the the soap film catenoid has the force that act on the interface to reduce its area.

At a given time T, $h = T/M$, where $0 < h \ll 1$ and M is a positive number. For $k = 0, 1, ..., M$

Let Γ_k be a smooth curve and E_k be region enclosed by Γ_k and boundary at time k.

We use two signed distance functions for initial condition.

$$d_0(x) = \begin{cases} \inf\limits_{y\in\Gamma_0} \|x-y\| & \text{if } x \in E_0 \\ \text{-}\inf\limits_{y\in\Gamma_0} \|x-y\| & \text{otherwise,} \end{cases}$$

$$d_{-1}(x) = \begin{cases} \inf\limits_{y\in\Gamma_0 - v_0 h} \|x-y\| & \text{if } x \in E_{-1} \\ \text{-}\inf\limits_{y\in\Gamma_0 - v_0 h} \|x-y\| & \text{otherwise.} \end{cases}$$

1) Set $u_0(x) = 2d_k - d_{k-1}$, where

$$d_k(x) = \begin{cases} \inf\limits_{y\in\Gamma_k} \|x-y\| & \text{if } x \in E_k \\ \text{-}\inf\limits_{y\in\Gamma_k} \|x-y\| & \text{otherwise.} \end{cases}$$

2) Solve the wave equation with zero initial velocity and initial condition u_0 at a time h

$$\begin{cases} u_{tt} = \triangle u & \text{in } (0,\, h) \times \Omega \\ \frac{\partial u}{\partial \nu} = 0 & \text{on } (0,\, h) \times \partial\Omega \\ u(t = 0,\, x) = u_0 & \text{in } \Omega \\ u_t(t = 0,\, x) = 0 & \text{in } \Omega. \end{cases}$$

3) Update the interface and the region.

4) Calculate d_{k+1}.

4. Model of a soap bubble catenoid

4.1 Derivation of the equation concerning a soap bubble catenoid

For the soap bubble catenoid, there is the force that act on the interface to reduce its area because the catenoid is the minimal surface. The force act on the interface that the curvature is $1/r$, where r is the radius of the circle in the catenoid for each grid point. Adding $1/r$ in the equation (1), we get

$$A = (-\kappa + 1/r)n. \tag{2}$$

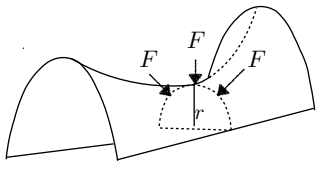

Figure 1. The half of catenoid

The differential equation concerning the soap bubble catenoid (2) is

$$\begin{cases} \alpha''(t,x) = -\kappa(x) + 1/r(x) & \text{in } (0,T) \times \Omega \\ \alpha'(t=0,x) = 0 & \text{in } \Omega \\ \alpha(t=0,x) = \gamma(x) & \text{in } \Omega, \end{cases}$$

where $\gamma(x)$ is a closed curve that be parametrised and initial velocity is zero.

4.2 BMO algorithm for a soap film catenoid

At a given time T, $h = T/M$, where $0 < h \ll 1$ and M is a positive number. For $k = 0, 1, ..., M$

1) Set $u_0(x) = d_k$.

2) Compute the radius in the catenoid for each grid point.

3) Solve the equation with zero initial velocity and initial condition u_0 at a time h

$$\begin{cases} u_{tt} = \triangle u + 1/r & \text{in } (0,\ h) \times \Omega \\ u = u_0 & \text{on } (0,\ h) \times \partial\Omega \\ u(t = 0,\ x) = u_0 & \text{in } \Omega \\ u_t(t = 0,\ x) = 0 & \text{in } \Omega. \end{cases} \tag{5}$$

4) Update the interface and the region.

5) Calculate d_{k+1}.

5. The equation solving

We solve the equation (5) by using finite difference method(central difference method for the second derivative). Let $u^k_{i,j}$ be an approximate solution at (t_k, x_i, y_j), $\Delta t = t_k - t_{k-1}$, $\Delta x = x_i - x_{i-1}$, $\Delta y = y_j - y_{j-1}$ and $\Delta x = \Delta y$. Then the approximate solution is

$$u^{k+1}_{i,j} = 2u^k_{i,j} - u^{k-1}_{i,j} + \left(\frac{\Delta t}{\Delta x}\right)^2 \left(u^k_{i+1,j} + u^k_{i-1,j} + u^k_{i,j+1} + u^k_{i,j-1} - 4u^k_{i,j}\right) + \Delta t^2 / r^k_{i,j}.$$

6. Numerical results

This simulation that we show is only some part of soap film catenoid.

400×400 grids, time discretisation is 0.001/10.

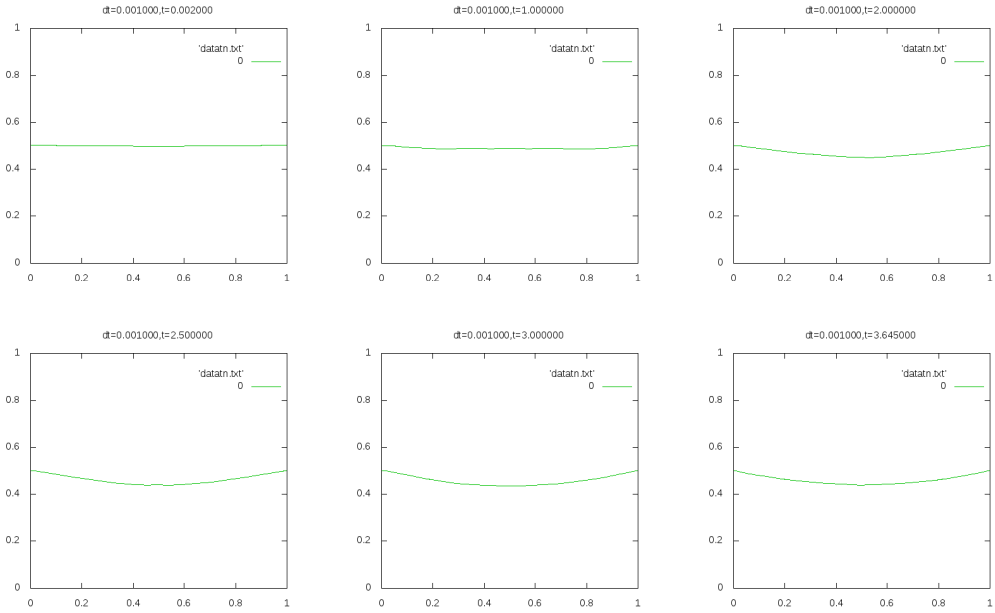

Acknowledgment

This work was supposed by Japan student services organization (JASSO). I would like to express my gratitude to Prof. Seiro Omata and Prof. Norbert Pozar for their many suggestions. I also acknowledge my friends for all their support.

References

1. B. Merriman, J. Bence, S. Osher (1994), Motion of Multiple Junctions: A Level Set Approach, *J. Comp. Phys.* **112**, 334-363.
2. E. Ginder and K. Svadlenka (2014), On an algorithm for curvature-dependent interfacial acceleration, *Proceedings of Computational Engineering Conference*, vol. 19
3. M. Ito and T. Sato (2010), In situ observation of a soap-film catenoid—a simple educational physics experiment, *Eur. J. Phys.*, **31**, 357-365.

Triple junction simulation using acceleration dependent BMO

Reza F. Arifin [a,b]

[a]Faculty of Mathematics and Natural Sciences, Institut Teknologi Bandung, Jl. Ganesha 10, Bandung 40132 Indonesia
[b]Institute of Science and Engineering, Kanazawa University, Kakuma, Kanazawa 920-1192 Japan
E-mail: reza_1622@students.itb.ac.id

Abstract. *We develop a method to simulate multiple bubbles and the triple junction motion in two dimensions driven by the mean curvature acceleration. The core of this method is the acceleration dependent BMO algorithm in a vector-valued formulation. To avoid a discontinuity in the vector-valued function, we adopt a signed distance vector formulation. Moreover we also develop the method for the area preserving motion.*

Keywords: BMO algorithm, acceleration dependent BMO, triple juction, mean curvature acceleration, hyperbolic mean curvature flow.

1 Introduction

Bubbles motion phenomenon has become an interesting research objective and there are many models and methods to approach such motions. One of the methods is called Bence-Merriman-Osher (BMO) algorithm. The original BMO algorithm [1] was introduced for realizing interfacial motion by mean curvature flow. Ginder and Svadlenka [2] introduced the modified version of the BMO algorithm for curvature-dependent interfacial acceleration. The method uses mean curvature acceleration instead of mean curvature flow on the surfaces to evolve.

In particular we consider the motion of interface governed by equation below

$$A = -\kappa \mathbf{n} \tag{1}$$

where A is acceleration of interface, κ is the mean curvature and $\mathbf{n}$ is unit normal vector.

We compare this method with Runge-Kutta fourth order for shrinking circle problem to see behaviour of the result. In this research, we also implement the method for multiple bubbles. In such phenomenon, we have to deal with triple junction. In order to handle multiple bubbles, we implement vector-valued BMO.

2 General model

In general we assume that the interface of bubble on certain point is moving accelerated by its mean curvature. The direction of its movement is on the opposite direction of normal vector. We can write the problem as bellow.

Let α be a position function and $\mathbf{n}$ be a unit normal vector, then

$$\begin{cases} \alpha_{tt} = -\kappa \mathbf{n}, \\ \alpha_t(t=0,s) = v_0(s), \quad s \in [0,1) \\ \alpha(t=0,s) = \gamma(s), \quad s \in [0,1). \end{cases} \tag{2}$$

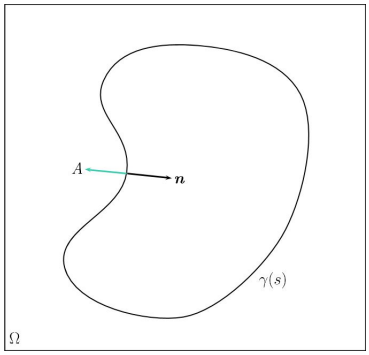

Figure 1: General model

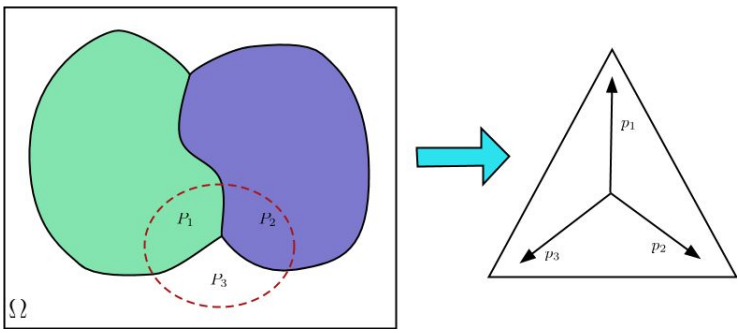

Figure 2: Three regions

where $\gamma(s)$ is a parameterized closed curve with initial velocity v_0 and κ is the mean curvature.

For multiple bubbles, each region P_i is assigned by reference vector p_i(see Figure.2). The way to construct reference vector we can see further at [3]. Each reference vector represent corresponding region. Analog with characteristic function in the original BMO [1], 0 and 1 represent two different regions.

3 Method

We approximate the motion with thresholding the solution to the wave equation which evolves from its initial condition. For one bubble case, it uses signed distance function constructed by its initial region. In the similar ways, for two or more bubbles, we implement signed distance vector [4] defined by,

Definition 3.1 *(Signed distance vector)* For m number of region and $\varepsilon > 0$, we define the *signed distance vector* $\mathbf{d}_\varepsilon : \mathbb{R}^N \to \mathbb{R}^{m-1}$ by:

$$\mathbf{d}_\varepsilon(x) := \sum_{i=1}^{m} \left[1 - \min\left(1, \frac{d_i(x)}{\varepsilon}\right)\right]\mathbf{p}_i,$$

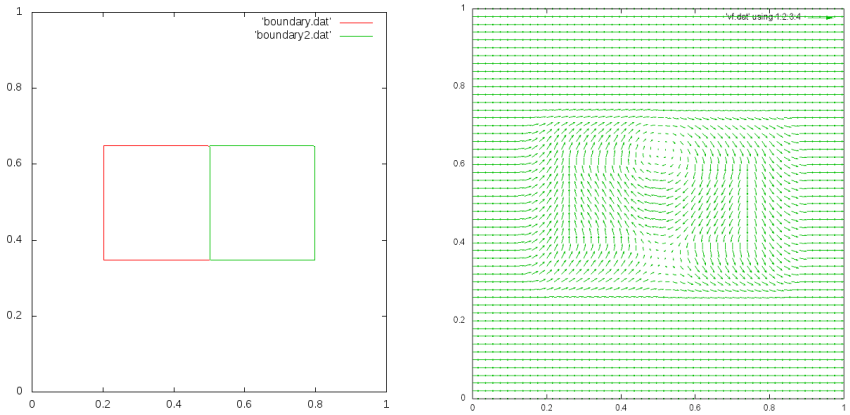

Three phases region Three phases SDV

Figure 3: Signed distance vector

where $d_i(\cdot) := \text{dist}(\cdot, P_i)$ is distance to region P_i and $\mathbf{p}_i$ is reference vector corresponding to each region P_i. For example we can see three region signed distance vector at Figure.3.

3.1 Acceleration dependent BMO algorithm

Here is the algorithm for Acceleration dependent BMO.

- For given time T, take $h = T/M$, where M is positive integer.
- Define $n-1$ dimensional reference vectors $\mathbf{p}_i$ for each corresponding to region P_i, $i = 1, 2, ..., n$.
- Set the signed distance vector using initial condition $\mathbf{d}_0$ and prepare $\mathbf{d}_{-1}$ obtained from the initial velocity along the interface.
- For $k = 0, 1, ..., M$
  1. Set $\mathbf{u}_0(x) = 2\mathbf{d}_k - \mathbf{d}_{k-1}$.
  2. Solve the vector-valued wave equation with initial condition $\mathbf{u}_0$ for time interval h and zero initial velocity
$$\begin{cases} \mathbf{u}_{tt} = \Delta \mathbf{u} & \text{in } (0,h) \times \Omega \\ \frac{\partial \mathbf{u}}{\partial \nu} = 0 & \text{on } (0,h) \times \partial\Omega \\ \mathbf{u}(t=0,x) = \mathbf{u}_0 & \text{in } \Omega \\ \mathbf{u}_t(t=0,x) = 0 & \text{in } \Omega \end{cases}$$
  3. Update each regions and set signed distance vector $\mathbf{d}_{k+1}$.

To update region, here we use "closest vector" to the reference vector. For illustration we can see Figure.4. Here we have $\mathbf{u}(h,x)$ as a solution of wave equation, then we update $\mathbf{u}_0$ as

$$\mathbf{u}_0 = p_j, \text{where } \mathbf{p}_j \cdot \mathbf{u}(h,x) = \max_{i=1,2,...,n} \mathbf{p}_i \cdot \mathbf{u}(h,x)$$

After we determine phase region each nodes on the domain, we set signed distance vector by Definition.3.1.

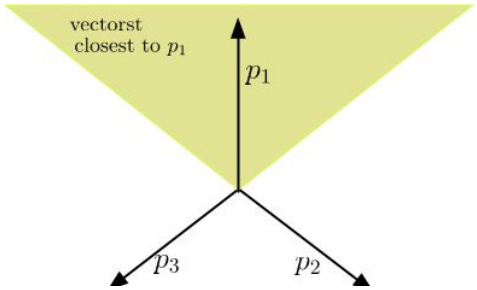

Figure 4: Updating region to closest vector

3.2 Minimizing movements

To solve wave equation, we implement the discrete Morse flow method. Let $\tau = h/N$ be a time discretization for given positive integer N. For each $n = 1, \ldots, N$, functional $\mathcal{J}_n(\mathbf{u})$ defined over $H^1(\Omega; \mathbb{R}^{n-1})$:

$$\mathcal{J}_n(\mathbf{u}) = \int_\Omega \left(\frac{|\mathbf{u} - 2\mathbf{u}_{n-1} + \mathbf{u}_{n-2}|^2}{2\tau^2} + \frac{|\nabla \mathbf{u}|^2}{2} \right) dx, \tag{3}$$

where $\mathbf{u}_{n-1}$ and $\mathbf{u}_{n-2}$ are given functions. To preserve the area, we include a constraint via penalization,

$$\mathcal{F}_n(\mathbf{u}) = \mathcal{J}_n(\mathbf{u}) + \frac{1}{\varepsilon} \sum_{i=1}^{3} |V_i - \text{meas}(P_i^{\mathbf{u}})|^2 \tag{4}$$

where $\varepsilon > 0$ is a small penalty parameter and V_i is prescribed area of region P_i.

We approximate the functional (3) and (4) by using piecewise linear finite element. To find minimizer of the functional here we use conjugate gradient method.

4 Numerical Result

Before we see numerical result, we do a numerical test for the method by comparing with Runge-Kutta fourth order for shrinking circle problem.

4.1 Numerical Test

The shrinking circle problem satisfies (5),

$$\begin{cases} r_{tt}(t) = -\frac{1}{r(t)}, & t \in [0, T) \\ r_t(0) = 0, \\ r(0) = 0.3, \end{cases} \tag{5}$$

For testing numerical result, we use various of parameters resolution and space/time. We measure the error by computing time-average of the absolute difference between radius of numerical result and Runge-Kutta fourth order. For Runge-Kutta fourth order, we use very small time step so it can represent the exact solution.

Table 1: Comparison with Runge-Kutta fourth order

resolution	space/time	average radius error
40×40	4	0.00666
40×40	8	0.00521
40×40	16	0.00537
80×80	4	0.00259
80×80	8	0.00278
80×80	16	0.00328
160×160	4	0.00164
160×160	8	0.00156
160×160	16	0.00145

From the comparison result at Table.1, we can see that the accuracy roughly increase almost twice as we increase the resolution twice. And the error is smaller than corresponding space discretization Δx.

4.2 Numerical Simulation

1. This is the simulation of two phases case without area preservation, resolution 160×160 and time discretization $\tau = 0.005/10$. For initial condition, here we use such kind of area because we want to see inertia effect while it evolve.

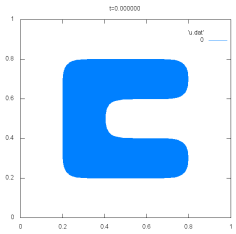

$t = 0.000$

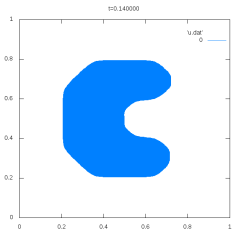

$t = 0.140$

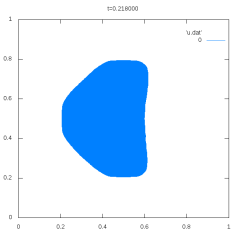

$t = 0.215$

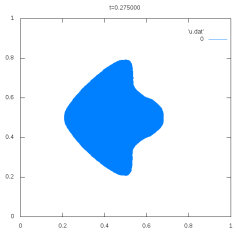

$t = 0.345$

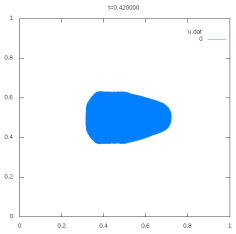

$t = 0.495$

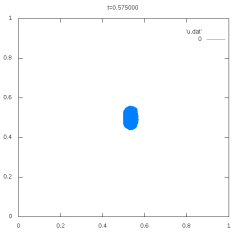

$t = 0.555$

2. This is the simulation of two phases case with area preservation, resolution 160×160 and time discretization $\tau = 0.005/10$. We use two ellipses area as initial condition. Because these two bubbles have the same phase, as the result it merges at certain time and remain as one

region. And the area is also preserved.

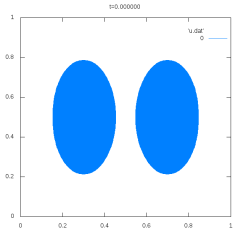

$t = 0.000$

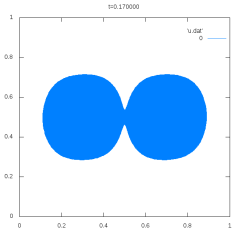

$t = 0.170$

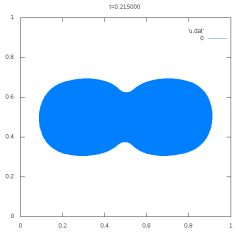

$t = 0.215$

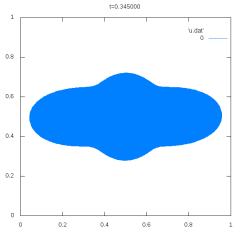

$t = 0.275$

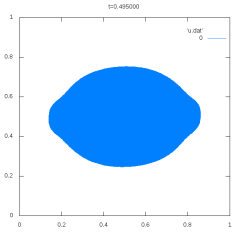

$t = 0.42$

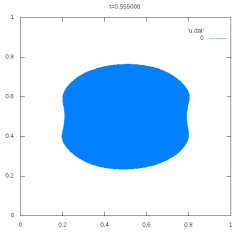

$t = 0.575$

3. This is the simulation of three phases case without area preservation, resolution 160×160 and time discretization $\tau = 0.005/10$. For initial condition here we use symmetric area of two squares. We can see inertia effect at the edge of the square.

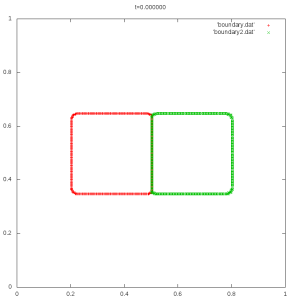

$t = 0$

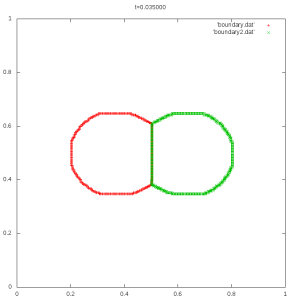

$t = 0.035$

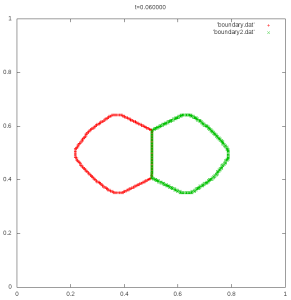

$t = 0.060$

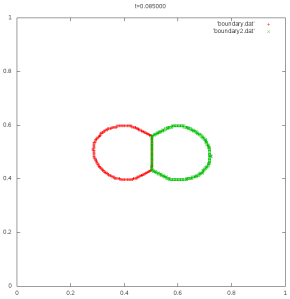

$t = 0.085$

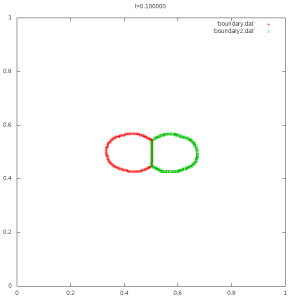

$t = 0.100$

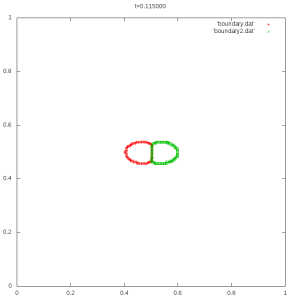

$t = 0.115$

5 Conclusion

As conclusion, we implemented the acceleration dependent BMO method for simulating bubble motion. We compared the numerical result for shrinking circle problem with Runge-Kutta fourth order. We also implemented the method for area preservation and for multiple bubbles (three area regions). For future work, this method can be applied for three dimensional bubble motion simulation that involve external force also.

6 Acknowledgment

I would like to thank Prof. Seiro Omata and Prof. Norbert Pozar for guiding me during this research in Japan. Financial support from DIKTI is acknowledged. Also big thanks to all DDP students for their support.

References

[1] B. Merriman, J. Bence, S. Osher (1994). Motion of multiple Junction: a level set approach. *J.Comp.Physics.*, textbf112, 334–363.

[2] E.Ginder, K.Svadlenka (2014). On algorithm for curvature-dependent interfacial acceleration. *Proceeding of Computational Engineering Conference.*, **19**.

[3] K.Svadlenka, E. Ginder, S. Omata (2014). A variational method for multiphase volume-preserving interface motion. *Journal of Computational and Applied Mathematics.*, **257**, 157–179

[4] N. Sofianah, R.Z. Mohammad, K. Svadlenka (2014). On a numerical method for the simulation of contact angle dynamics. *Proceeding of Computational Engineering Conference.*, **19**.

[5] P. LeFloch, K. Smoczyk (2008). The hyperbolic mean curvature flow. *Journal de Mathematiques Pures et Appliques.*, textbf90, 591–614.

[6] R.Z. Mohammad (2014). Numerical analysis of multiphase curvature-driven interface evolution with volume constraint. *Ph.D. Dissertation of Kanazawa University.*

[7] S. Omata (1997). A Numerical method based on the discrete Morse semiflow related to parabolic and hyperbolic equation. *Nonlinear Analysis.*, **30**, 2181-2187.

Numerical Construction of Energy-Theoretic Crack Propagation based on a Localized Francfort-Marigo Model

Armanda Ikhsan[a,b], Masato Kimura[b], Takeshi Takaishi[c], Maharani Ahsani Ummi[a,b]

[a]Faculty of Mathematics and Natural Sciences, Institut Teknologi Bandung, Jl. Ganesha 10, Bandung 40132 Indonesia, E-mail: armandaikhsan@gmail.com, maharaniahsaniummi@gmail.com
[b]Institute of Science and Engineering, Kanazawa University, Kakuma, Kanazawa 920-1192 Japan, E-mail: mkimura@se.kanazawa-u.ac.jp
[c]Faculty of Information Design, Hiroshima Kokusai Gakuin University, Nakano, Aki-ku, Hiroshima 739-0321 Japan, E-mail: t.takaishi@hkg.ac.jp

Abstract. *We simulate straight crack propagation using idea from the classical Griffith theory and Francfort-Marigo energy. According to the energy-theoretic model proposed by Francfort and Marigo, propagation of a straight crack is described by means of sum of elastic and surface energies. We modify the Francfort-Marigo model by replacing the global minimum by a local one in order to be consistent with the Griffith theory. We numerically construct some energy-theoretic propagation of straight cracks using finite element method and show some discontinuous growth behaviour of the crack.*

Keywords: crack propagation, elasticity problem, finite element method

1 Introduction

Crack propagation can cause serious problems. Therefore, to understand the crack propagation phenomenon is important. Griffith's theory [3] tells that a crack will propagate only if the elastic energy released during the crack growth is greater than or equal to the surface energy which is proportional to the area of the new crack surfaces.

Francfort and Marigo [2] proposed a crack propagation model based on the total energy which is a sum of elastic energy and surface energy. They extended the classical Griffith theory and proposed the model to describe crack propagation. This is one of the most naive models for crack propagation, but is not suitable for numerical simulation.

Although a number of crack propagation models and numerical algorithms have been proposed in engineering and physics, as far as the authors know, any mathematically closed model which can be numerically computable has not been established. Among the models, in particular, phase field model proposed in [4] is remarkable for its easy numerical treatment. It is described as a gradient flow of an approximate energy of the Francfort-Marigo energy by using the idea of Ambrosio-Tortorelli regularization [1]. Since it has a similar form of the reaction-diffusion equation, its numerical simulation is relatively easier than the other models. However, the accuracy of this model has not been studied well due to the lack of an established model.

As a theoretically reliable model, we investigate the energy-theoretic one and numerically construct some crack propagation. Which will be used as a reference solution to check the accuracy of other crack propagation models such as the phase field model.

The outline of this paper is as follows. In the second section, we will give a two dimensional setting of an antiplane displacement and mode III crack propagation with brief explanation about the classical Griffith theory and the Francfort-Marigo model and how we use it to make simulation. In the third section we will propose a localized Francfort-Marigo model and show some numerical examples. In the last section we will give conclusions and future work.

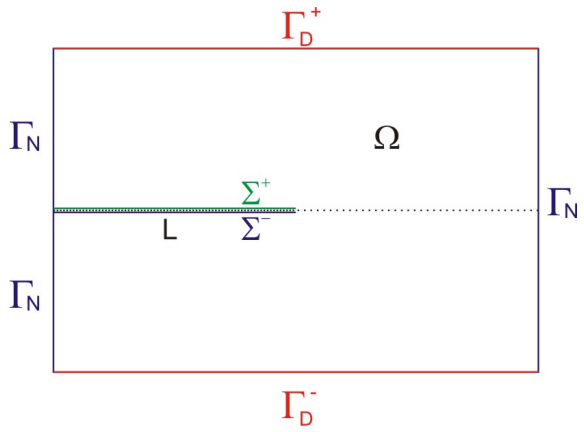

Figure 1: Domain

2 Classical Griffith Theory and the Francfort-Marigo Model

We consider a mode III crack propagation in a plate by the deformation perpendicular to the plate. The plate is supposed to be an isotropic elastic material with constant thickness. We suppose that $x = (x_1, x_2) \in \mathbb{R}^2$ is a Cartesian coordinate parallel to the plate, and that x_3 is a coordinate perpendicular to the plate. We assume that the deformation of the plate is limited to the x_3-direction. Therefore, we treat the problem as a two dimensional domain Ω. We assume a displacement field $\bar{u}$ has the following form :

$$\bar{u}(x_1, x_2, x_3) = (0, 0, u(x_1, x_2))^T$$

Let Ω be a bounded two dimensional domain, with a piecewise smooth boundary $\Gamma = \partial\Omega$. We suppose that Γ_D is a non empty open portion of Γ and set $\Gamma_N := \Gamma \setminus \Gamma_D$. A crack in Ω is denoted by $\Sigma \subset \Omega$ and its upper and lower sides are denoted by Σ^+ and Σ^- respectively. We suppose Σ is a straight crack of length L with only one tip in Ω as shown in Figure 1.

According to [4], the antiplane displacement u satisfies the following equations :

$$\begin{cases} \Delta u = 0 & \text{in } \Omega \setminus \Sigma \\ u = g & \text{on } \Gamma_D \\ \dfrac{\partial u}{\partial n} = 0 & \text{on } \Gamma_N \cup \Sigma^{\pm} \end{cases} \tag{1}$$

We denote the solution u to (1) by $\hat{u}(L, g) \in H^1(\Omega \setminus \Sigma)$. We define a corresponding bilinear form and an elastic energy :

$$a(u, v; \Omega \setminus \Sigma) := \frac{\mu}{2} \int_{\Omega \setminus \Sigma} \nabla u \cdot \nabla v \, dx,$$

$$E(L, g) := \min_{u|_{\Gamma_D} = g} a(u, u; \Omega \setminus \Sigma) = a\left(\hat{u}(L, g), \hat{u}(L, g); \Omega \setminus \Sigma\right),$$

where $\mu > 0$ is a rigidity constant.

We suppose that the Dirichlet boundary condition depends on time t, that is $u = g(t) = g(\cdot, t)$ on Γ_D. The classical Griffith's criterion for the crack propagation is derived from a balance of the

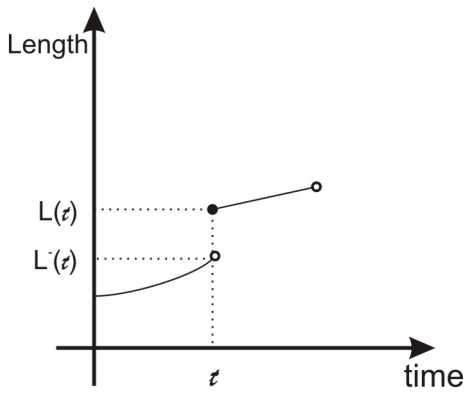

Figure 2: A discontinuous crack propagation

released energy and the created crack length. According to the theory, so-called energy release late G is defined as

$$G := -\frac{\partial E}{\partial L}(L, g(t)) \geq 0.$$

The crack Σ can propagate only if

$$G \geq \gamma. \tag{2}$$

Where the constant $\gamma > 0$ is called fracture toughness. This is called Griffith's criterion. Francfort and Marigo introduced the following total energy in (1):

$$\mathcal{E}(L, g) := E(L, g) + \gamma L \qquad (L := |\Sigma|),$$

which is a sum of the elastic energy $E(L, g)$ and a surface energy γL. The condition (2) is also equivalent to

$$\frac{\partial \mathcal{E}}{\partial L}(L, g(t)) \leq 0. \tag{3}$$

They proposed the following simple crack propagation model as an extension of the Griffith theory. They considered that $L(t) = |\Sigma(t)|$ is given by

$$\begin{cases} L(t) := \underset{L^-(t) \leq L \leq L_\infty}{\arg\min} \mathcal{E}(L, g(t)) \\ L^-(t) := \sup_{s<t} L(s), \end{cases} \tag{4}$$

where L_0 is the width of Ω. We call (4) Francfort-Marigo model in this paper. We remark that $L(t)$ is a non-decreasing function, but can be discontinuous as shown in Figure 2.

We suppose that the boundary condition $g(t)$ on Γ_D is given in the following form :

$$g(t) = tg_0(x) \ (x \in \Gamma_D),$$

where $x = (x_1, x_2)$ denotes the space variable. Since $\hat{u}(L, tg_0)$ is given as $\hat{u}(L, tg_0) = t\hat{u}(L, g_0)$, we get

$$E(L, tg_0) = a(t\hat{u}(L, g_0), t\hat{u}(L, g_0), \Omega \setminus \Sigma) = t^2 a(\hat{u}(L, g_0), \hat{u}(L, g_0), \Omega \setminus \Sigma) = t^2 E(L, g_0).$$

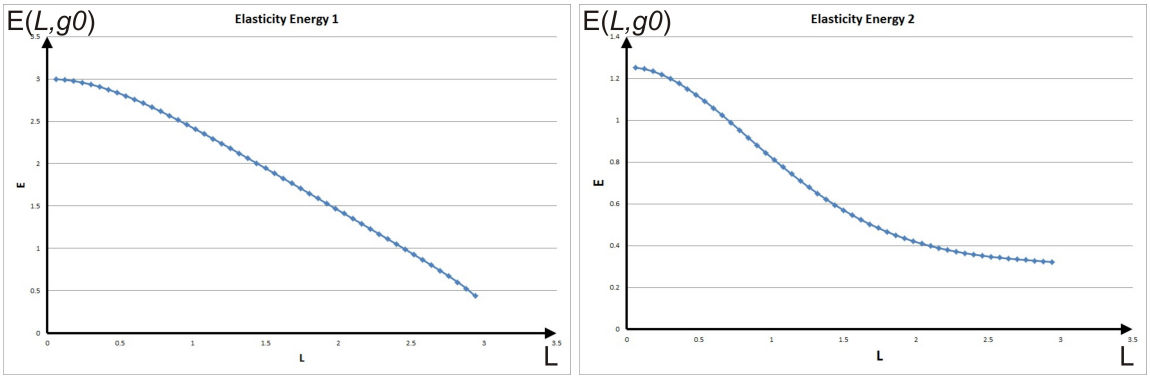

Figure 3: Graphs of elastic energy $E(L, g_0)$ with $g_0 = 1$ (left) and $g_0 = \cos^2(\frac{\pi x_1}{2L_\infty})$ (right)

Therefore the total energy becomes

$$\mathcal{E}(L, t\ g_0) = t^2 E(L, g_0) + \gamma L.$$

In this paper, for simplicity, we assume $\Omega = (0, L_\infty) \times (-l, l)$ and $\Sigma(t) = (0, L(t)] \times \{0\}$ as shown in Figure 1 and set $\mu = 2$. Under the symmetry condition $g_0(x_1, -l) = -g_0(x_1, l)$ on Γ_D, for the initial condition $g_0 = 1$ and $g_0 = \cos^2(\frac{\pi x_1}{2L_\infty})$, we get graphs of $E(L, g_0)$ as seen in Figure 3. These graphs are computed by using FreeFem++ software [5].

From Figure 3, we can see the difference of the profiles of $E(L, g_0)$ between $g_0 = 1$ and $g_0 = \cos^2(\frac{\pi x_1}{2L_\infty})$. On the left figure, the graph is concave. But on the right one, the graph has two parts, concave and convex. These shapes essentially affect the type of crack propagation as will be seen later.

3 Localized Francfort-Marigo model

From the Griffith theory, we know that a crack cannot propagate if (3) is not reached. But, as we will see later, the Francfort-Marigo model (4) allows a crack to have a jump even if Griffith's criterion is not satisfied. So, we need to modify (4) to make it consistent to the classical Griffith's criterion.

In order to replace the global minimum in (4), we define a notion of a nearest local minimum. We assume $f \in C^1([a, b])$, we define a nearest local minimum of f in $[a, b]$ as follows :

$$\underset{a \le x \le b}{\text{arg loc-min}}\, f(x) := \begin{cases} a & (\text{ if } f'(a) \ge 0), \\ \sup\left\{x \in (a, b];\ f'(y) < 0\ ({}^\forall y \in [a, x))\right\} & (\text{ if } f'(a) < 0). \end{cases}$$

We propose the following modification of the Francfort-Marigo model.

Problem 3.1 (localized Francfort-Marigo model)**.** *Let L_∞ be the maximum length of the straight crack in Ω. For a given initial crack Σ_0 of length $L_0 \in (0, L_\infty)$, find $\Sigma(t)$ of length $L(t)$ for $t \ge 0$ such that*

$$L(t) = \underset{L^-(t) \le L \le L_\infty}{\text{arg loc-min}}\, \mathcal{E}(L, g(t))(t \ge 0),$$

where

$$L^-(t) := \begin{cases} L_0 & (t = 0), \\ \sup\limits_{0 \le s < t} L(s) & (t > 0). \end{cases}$$

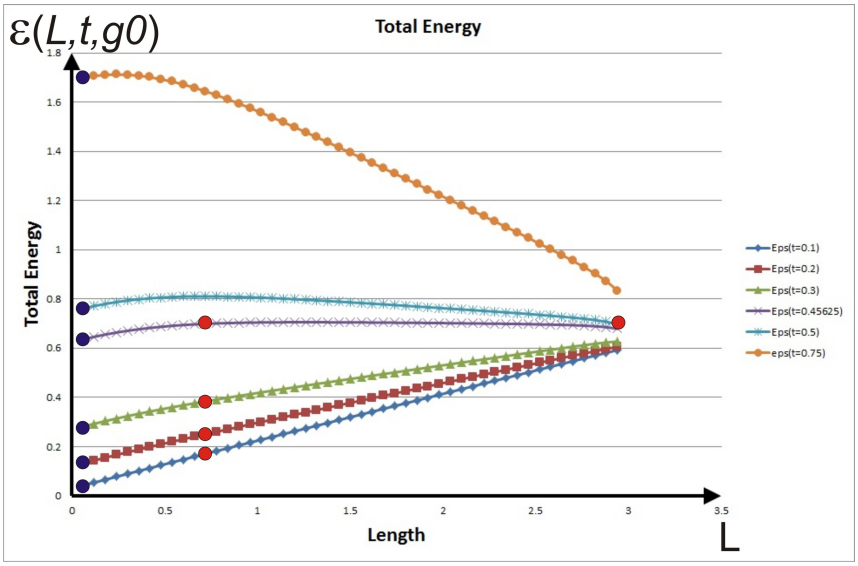

Figure 4: Graph of total energy $\mathcal{E}(L, t\ g_0)$ with $g_0 = 1$

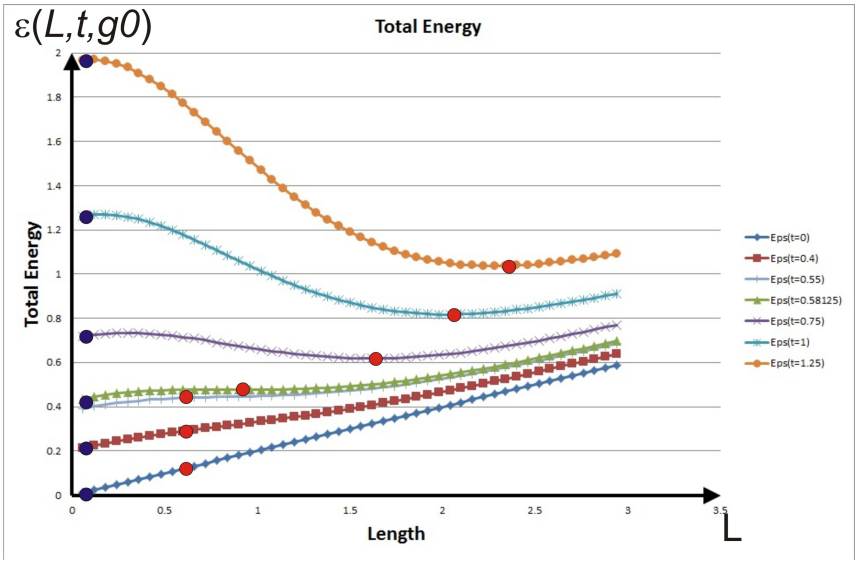

Figure 5: Graph of total energy $\mathcal{E}(L, t\ g_0)$ with $g_0 = \cos^2(\frac{\pi x_1}{2L_\infty})$

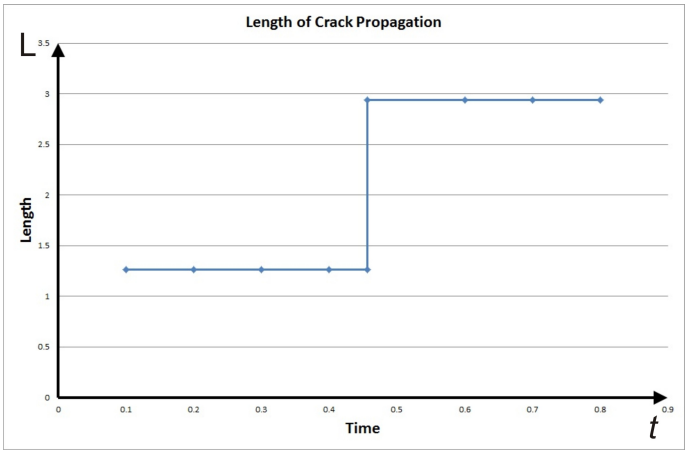

Figure 6: Length of crack propagation with $g_0 = 1$

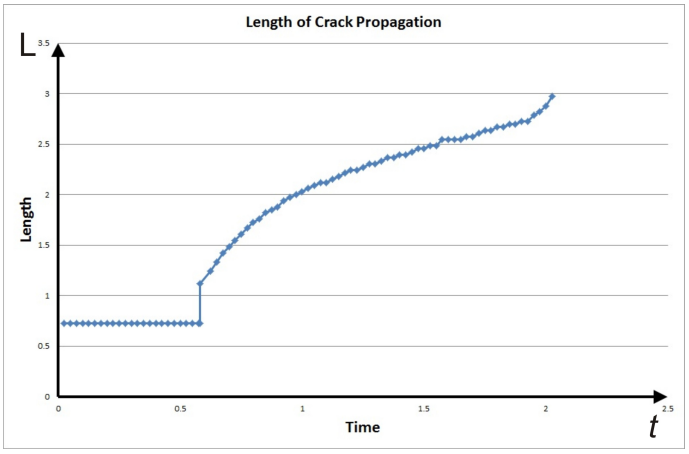

Figure 7: Length of crack propagation with $g_0 = \cos^2(\frac{\pi x_1}{2L_\infty})$

We set $\gamma = 0.5$ then using relation $\mathcal{E}(L, t\ g_0) = t^2 E(L, g_0) + \gamma L$, we get graphs of the total energies as shown in Figures 4 and 5. In both cases in Figures 4 and 5, if the initial crack length L_0 is small enough as drawn by dots, the condition (4) is not reached until the end of these simulations. We remark that a solution of Problem 3.1 does not propagate too, but one of the original Francfort-Marigo model (4) does. But if we take L_0 near 0.6 as drawn by square, length suddenly jumps to the end, in one time for the case of $g_0 = 1$.

On the other hand, in the case of $g_0 = \cos^2(\frac{\pi x_1}{2L_\infty})$ there is a little jump and after that the crack starts propagating smoothly until the end of length. The obtained solutions to Problem 3.1 are shown in Figures 6 and 7. We remark that the difference of the behaviors of these solutions arises from the difference of the profiles of $E(L, g_0)$ as shown in Figure 3.

4 Conclusions and Future work

We studied energy-theoretic crack propagation models analytically and numerically in this paper. We computed the elastic energy $E(L, g_0)$ for each L by using FreeFem++. For the Francfort-Marigo model, we investigated the relations of the behaviour of a solution and the profile of the graph of $E(L, g_0)$. We pointed out that the solution can propagate with a jump even if Griffith's criterion is not satisfied. We proposed a localized Francfort-Marigo model to make it more consistent to the classical Griffith's criterion and numerically constructed some solutions. We observed that they exhibit several discontinuous behaviours but are consistent to Griffith's criterion.

The behaviour of the solutions of Problem 3.1 which were constructed numerically in this paper is expected to represent theoretical straight crack propagation in an ideal setting. They will be useful for checking the accuracy and reliability of other models, such as the phase field model. Some comparison results with Takaishi-Kimura model will be reported in our forthcoming paper.

Acknowledgment

One of the authors would like to thank MEXT scholarship of SGU for the financial support in his research.

References

[1] L. Ambrosio and V.M. Tortorelli (1992). On the approximation of free discontinuity problems. *Boll. Un. Mat. Ital.*, **7**, 6-B, 105 – 123.

[2] G.A. Francfort and J.-J. Marigo (1998). Revisiting brittle fracture as an energy minimization problem. *J. Mech. Phys. Solids*, **46**, 1319 – 1342.

[3] A.A. Griffith (1920). The phenomenon of rupture and flow in solids. *Phil. Trans. Royal Soc. London A*, **221**, 163 – 198.

[4] T. Takaishi and M. Kimura (2009). Phase field model for mode III crack growth in two dimensional elasticity. *Kybernetika*, **45**, no.4, 605 – 614.

[5] F. Hecht (2012). New development in FreeFem++. *J. Numer. Math.*, **20**, no.3-4, 251 – 265.

Shape Optimization Approach to a Free Boundary Problem

Maharani Ahsani Ummi[a,b], Masato Kimura[b],
Hideyuki Azegami[c], Kohji Ohtsuka[d], Armanda Ikhsan[a,b]

[a]Faculty of Mathematics and Natural Sciences, Institut Teknologi Bandung, Jl. Ganesha 10, Bandung 40132 Indonesia, E-mail: maharaniahsani@gmail.com, armandaikhsan@gmail.com
[b]Institute of Science and Engineering, Kanazawa University, Kakuma, Kanazawa 920-1192 Japan, E-mail: mkimura@se.kanazawa-u.ac.jp
[c]Graduate School of Information Science, Nagoya University, Furo-cho, Chigusa-ku, Nagoya, 464-8601 Japan, Email: azegami@is.nagoya-u.ac.jp
[d]Department of Computer Science, Hiroshima Gakuin University, Aki-ku, Nakano, Hiroshima,739-0321 Japan, Email: ohtsuka@hgk.ac.jp

Abstract. *We take a shape optimization approach to solve a free boundary problem of the Poisson equation numerically. A numerical method called traction method invented by one of the authors are applied. We begin by changing the free boundary problem to a shape optimization problem and define a least square functional as a cost function. Then shape derivative of the cost function is derived by using Lagrange multiplier method. Detail structures and profiles of exact solutions to a concrete free boundary problem due to A. Henrot are also illustrated with proofs. They are used to check the efficiency of the traction method.*

Keywords: *shape optimization, free boundary problem, traction method*

1 Introduction

Free Boundary Problem (FBP) deals with solving partial differential equations in a domain whose boundary is partially unknown; that the portion of boundary is called a free boundary. The study about free boundary problem is an important branch of partial differential equations (PDEs). In most cases, it is difficult to obtain analytical exact solution of free boundary problem. Therefore numerical analysis is needed to compute the approximation of the solutions.

Shape optimization approach can be used as one of the methods to solve free boundary problem numerically. A numerical method called traction method was developed for solving many shape optimization problems. However, the exact solution (optimal shape) is usually unknown even for a simple problem since this method is often applied only in engineering field. Our aim in this paper is to apply the traction method to obtain a numerical solution of free boundary problems. Then to check the efficiency of the traction method, we consider the following free boundary problem, since its exact solutions are analytically derived by using conformal mapping due to the idea of A. Henrot [2].

Problem 1.1 *Let μ be a given function in $\mathbb{R}^2$ with compact support. Find (u, Ω) such that $supp(\mu) \subset \Omega$ and*

$$\begin{cases} -\Delta u = \mu & \text{in } \Omega \\ u = 0 & \text{on } \Gamma := \partial\Omega \\ \dfrac{\partial u}{\partial n} = -1 & \text{on } \Gamma. \end{cases}$$

where μ is a combination of Dirac functions

$$\mu := \sum_{j=1}^{N} \alpha_j \delta_{\xi_j},$$

with $\alpha_j > 0$ and $\xi_j \in \mathbb{C} \cong \mathbb{R}^2$.

The organization of this paper is as follows. In Section 2, the detail structures and profiles of exact solutions to a concrete free boundary problem due to A. Henrot [2] are illustrated with proofs. Then we change this free boundary problem to a shape optimization problem by defining a cost function. Cost function is a function that we want to minimize it. Afterwards, we derive variation formula of the cost function using Lagrange multiplier method and an adjoint problem. Finally we can apply the traction method and compare its result with the exact solutions from the previous section.

2 Exact Solutions

We solve Problem 1.1 analytically by using conformal mapping. In this section, we identify $\mathbb{R}^2 \cong \mathbb{C}$. Especially, we denote a $\mathbb{R}^2$-coordinate in Ω by $x = (x_1, x_2)$ and its complex representation by $\xi = x_1 + ix_2 \in \mathbb{C}$. But we often mix these notation if no confusion occurs. For a complex variable $\xi = x_1 + ix_2 \in \mathbb{C}$, we denote the two dimensional Lebesgue measure by $d\mathcal{L}^2_\xi$. Let

$$G_0 := \{\Omega \,|\, \Omega \text{ is a bounded open set in } \mathbb{R}^2,\ \mathrm{supp}(\mu) \subset \Omega, \partial\Omega \text{ is Lipschitz}\}.$$

We define a cut-off function $\eta \in \mathbb{C}^\infty(\Omega)$ such that $\eta(x) = 1$ in a neighborhood of $\partial\Omega$ and $\eta(x) = 0$ in neighborhood of $\mathrm{supp}(\mu)$. We call (u, Ω) a weak solution of Problem 1.1 if $\Omega \in G_0$ and they satisfy,

$$\begin{cases} \displaystyle\int_\Omega \nabla u \cdot \nabla \varphi \, dx = -\int_{\partial\Omega} \varphi ds \quad (\forall \varphi \in H^1(\Omega), \mathrm{supp}(\mu) \cap \mathrm{supp}(\varphi) = \emptyset) \\ \displaystyle u(x) - \sum_{j=1}^{N} \alpha_j E(x - \xi_j) \text{ is harmonic function in } \Omega \\ \eta u \in H^1_0(\Omega), \end{cases}$$

where $E(x) = -\frac{1}{2\pi} \log |x|$ is the fundamental solution for $-\Delta$.

Lemma 2.1 *Let Ω_1 and Ω_2 are bounded domains. We suppose that $u \in H^1_0(\Omega_1)$ and set $\Phi(z)$ as a conformal mapping that maps Ω_0 to Ω_1, and $w(z) := u(\Phi(z))$ for $z \in \Omega_0$. Then $w \in H^1_0(\Omega_0)$.*

Proof. We first remark the following equality:

$$\|\nabla(f \circ \Phi)\|_{L^2(\Omega_0)} = \|\nabla f\|_{L^2(\Omega_1)}.$$

For $z \in \Omega_0$, we set $\xi = \Phi(z) \in \Omega_1$. Then $d\mathcal{L}^2_\xi = |\Phi'(z)|^2 d\mathcal{L}^2_z$ holds. Since $|\nabla(f \circ \Phi)(z)| = |\nabla f(\xi)||\Phi'(z)|$, we have

$$\begin{aligned}\|\nabla(f \circ \Phi)\|_{L^2(\Omega_0)} &= \int_{\Omega_0} |\nabla(f \circ \Phi)(z)|^2 d\mathcal{L}^2_z \\ &= \int_{\Omega_0} |\nabla f(\xi)|^2 |\Phi'(z)|^2 d\mathcal{L}^2_z \\ &= \int_{\Omega_1} |\nabla f(\xi)|^2 d\mathcal{L}^2_\xi \\ &= \|\nabla f\|^2_{L^2(\Omega_1)}.\end{aligned}$$

We choose a sequence $\{u_n\} \subset C_0^\infty(\Omega_1)$ which satisfies

$$\lim_{n\to\infty} \|u - u_n\|_{H^1(\Omega_1)} = 0$$

and define $w_n := u_n \circ \Phi \in C_0^\infty(\Omega_0)$. Since $\{u_n\}$ is a Cauchy sequence in $H^1_0(\Omega_1)$, from the Poincaré inequality we have

$$\begin{aligned}\|w_m - w_n\|_{H^1(\Omega_0)} &\le C(\Omega_0)\|\nabla(w_m - w_n)\|_{L^2(\Omega_0)} \\ &= C(\Omega_0)\|\nabla(u_m - u_n)\|_{L^2(\Omega_1)} \\ &\le C(\Omega_0)\|(u_m - u_n)\|_{H^1(\Omega_1)},\end{aligned}$$

and it follows that $\{w_n\}$ is a Cauchy sequence in $H^1(\Omega_0)$. Hence, there exists $w_* \in H^1_0(\Omega_0)$ such that

$$\lim_{n\to\infty} \|w_* - w_n\|_{H^1(\Omega_0)} = 0.$$

For an arbitrary subdomain D with $\bar{D} \subset \Omega_0$, we have

$$\begin{aligned}\|w - w_*\|_{L^2(D)} &\le \|w - w_n\|_{L^2(D)} + \|w_n - w_*\|_{L^2(D)} \\ &\le \|w - w_n\|_{L^2(D)} + \|w_n - w_*\|_{H^1(\Omega_0)},\end{aligned}$$

where the second term tends to 0 as $n \to \infty$. On the other hand, the first term also converges to 0 as $n \to \infty$ as follows:

$$\begin{aligned}\|w - w_n\|^2_{L^2(D)} &= \int_D |(w - w_n)(z)|^2 \, d\mathcal{L}^2_z \\ &= \int_{\Phi(D)} |(u - u_n)(\xi)|^2 \frac{1}{|\Phi'(z)|} \, d\mathcal{L}^2_\xi \\ &\le C_D^2 \int_{\Phi_D} |u - u_n|^2 \, d\mathcal{L}^2_\xi \\ &= C_D^2 \|(u - u_n)(\xi)\|^2_{L^2(\Phi(D))} \\ &\le C_D^2 \|u - u_n\|^2_{L^2(\Omega_1)},\end{aligned}$$

where $C_D = (\min_{z\in\bar{D}} |\Phi'(z)|)^{-1}$. Hence we have $w = w_*$ in $L^2(D)$ for an arbitrary domain D with $\bar{D} \subset \Omega_0$. This implies

$$w(z) = w_*(z) \qquad \mathcal{L}^2_z\text{-a.e. } z \in \Omega_0,$$

and we conclude that $w \in H_0^1(\Omega_0)$. ■

The following theorems are given in [2] without detail of their proofs. We give a proof here for the readers convenience.

Theorem 2.1 (A. Henrot [2]) *Suppose $N = 1$. Then (u, Ω) is a weak solution of Problem 1.1, if and only if $\alpha_1 > 0$ and*

$$\begin{cases} \Omega = \left\{ x \in \mathbb{R}^2 \middle| \, |x - \xi_1| < \dfrac{\alpha_1}{2\pi} \right\} \\ u = \dfrac{\alpha_1}{2\pi} \log \dfrac{\alpha_1}{2\pi |x - \xi_1|}. \end{cases} \tag{1}$$

Proof. It is easy to show that (1) is a solution of Problem 1.1. We suppose that (u, Ω) is a weak solution of Problem 1.1. We show that Ω is connected. Let Ω_0 is an open component of Ω with $\xi_1 \notin \Omega_0$, then $\Delta u = 0$ on Ω_0 and

$$\int_{\Omega_0} \nabla u \cdot \nabla \varphi \, dx = - \int_{\partial \Omega_0} \varphi \, ds \qquad \forall \varphi \in H^1(\Omega_0).$$

We choose $\varphi = 1$ in Ω_0, then we have

$$-|\partial \Omega_0| = - \int_{\partial \Omega_0} \varphi \, ds = \int_{\Omega_0} \nabla u \cdot \nabla \varphi \, dx = 0.$$

This contradicts to $|\partial \Omega_0| > 0$. Hence, all of the component of Ω has to include ξ_1. Therefore, Ω is connected.

Let $\Phi(z)$ be a conformal mapping from the unit disc $D_0 := \{ z \in \mathbb{C} \big| |z| < 1 \}$ to Ω with $\Phi(0) = \xi_1$ and $\Phi'(0) > 0$. We define

$$\Psi(z) := \begin{cases} \dfrac{\Phi(z) - \Phi(0)}{z} & (z \neq 0, z \in D_0) \\ \Phi'(0) & (z = 0), \end{cases} \tag{2}$$

then $\Psi(z)$ is holomorphic in D_0 and $\Psi(z) \neq 0$ for $z \in D_0$.
We define $w(z) = u(\Phi(z))$ $(z \in D_0)$. From the conditions $\Delta u_0 = 0$ in Ω,

$$u(\xi) = \alpha_1 E(\xi - \xi_1) + u_0(\xi) \qquad (\xi \in \Omega \setminus \{\xi_1\}),$$

we have

$$\begin{aligned} w(z) &= \alpha_1 E(\Phi(z) - \xi_1) + u_0(\Phi(z)) \\ &= \alpha_1 E(\Phi(z) - \Phi(0)) + u_0(\Phi(z)) \\ &= \alpha_1 E(z\Psi(z)) + u_0(\Phi(z)) \\ &= \alpha_1 E(z) - \frac{\alpha_1}{2\pi} \log |\Psi(z)| + u_0(\Phi(z)). \end{aligned}$$

Since the second and third terms of the equation above are harmonic in D_0, we obtain $-\Delta w = \alpha_1 \delta_0$ in D_0. We define $\tilde{w}(z) := \eta(\Phi(z)) w(z) = (\eta u) \circ \Phi(z)$. From Lemma 2.1, $\tilde{w} \in H_0^1(D_0)$. Since $\tilde{w} = w$

in a neighborhood of ∂D_0 and is harmonic, from the theory of elliptic regularity [4], w is smooth up to ∂D_0 and $w = 0$ on ∂D_0. Hence, the following equations holds

$$\begin{cases} -\Delta w = \alpha_1 \delta_0 & \text{in } D_0 \\ w = 0 & \text{on } \partial D_0 \\ \dfrac{\partial w}{\partial n} = -|\nabla w| = -|\nabla u||\Phi'| = -|\Phi'| & \text{on } \partial D_0. \end{cases} \tag{3}$$

From the first two equations of (3), we have $w(z) = \alpha_1 E(z)$ and

$$\frac{\partial w}{\partial n} = -\frac{\alpha_1}{2\pi}\Big(\frac{\partial}{\partial r}\log r\Big)\Big|_{r=1} = -\frac{\alpha_1}{2\pi}.$$

By the third condition of (3), we obtain $|\Phi'(z)| = \frac{\alpha_1}{2\pi}$ on ∂D_0. We set $v(x,y) := \mathrm{Re}[\log|\Phi'(z)|] = \log|\Phi'(z)|$ and $v(z)$ is harmonic since Φ is holomorphic and $\Phi'(z) \neq 0$ in D_0 . Then $\Delta v = 0$ in D_0 and $v = \log\frac{\alpha_1}{2\pi}$ on ∂D_0 hold and these imply that $v = \log\frac{\alpha_1}{2\pi}$ in D_0. Since $\mathrm{Re}[\log\Phi'(z)] = v = \log\frac{\alpha_1}{2\pi}$ in D_0, we obtain that $\log\Phi'(z) = \log\frac{\alpha_1}{2\pi} + i\beta$ for $\beta \in \mathbb{R}$. From the condition $\Phi'(0) > 0$, $\beta = 0$ follows. Hence we have $\Phi'(z) = \frac{\alpha_1}{2\pi}$ and conclude that

$$\Phi(z) = \frac{\alpha_1}{2\pi}z + \xi_1,$$

where we used $\Phi(0) = \xi_1$. Therefore by the conformal mapping $\Phi(z)$ we obtain

$$\Omega = \{x \in \mathbb{R}^2 \big| |x - \xi_1| < \frac{\alpha_1}{2\pi}\}$$

as a solution of Problem 1.1.

We know that $u = 0$ on $\partial\Omega$, then we have $u_0 = \frac{\alpha_1}{2\pi}\log\frac{\alpha_1}{2\pi}$. Hence we can conclude that

$$u(x) = -\frac{\alpha_1}{2\pi}\log|x - \xi_1| + \frac{\alpha_1}{2\pi}\log\frac{\alpha_1}{2\pi} = \frac{\alpha_1}{2\pi}\log\frac{\alpha_1}{2\pi|x - \xi_1|}.$$

■

Let us consider the case $N = 2$. We suppose that $c > 0$ and $\xi_1, \xi_2 \in \mathbb{C} \cong \mathbb{R}^2$ are given as $\xi_1 = c$ and $\xi_2 = -c$. We denote the Dirac function at ξ_1 and ξ_2 by δ_c and δ_{-c}, respectively, we consider

$$\mu = \alpha\delta_c + \alpha\delta_{-c} \tag{4}$$

for same $\alpha > 0$. Then we define a conformal mapping on D_0

$$\Phi_a(z) := \frac{\alpha(1 - a^4)}{4\pi a^2}\left[\frac{-2z}{z^2 - 1/a^2} + a\log\frac{1/a + z}{1/a - z}\right] \tag{5}$$

for $0 < a < 1$.

Theorem 2.2 (A.Henrot [2]) *We suppose a function μ as in* (4),

1. *(u, Ω) is a weak solution to Problem 1.1 and Ω is connected, if and only if there exists $a \in (0,1)$ such that $c = \Phi_a(a)$, $\Omega = \Phi_a(D_0)$, and $u(\xi) = w(\Phi_a^{-1}(\xi))$, $\xi \in \Omega$, where*

$$w(z) := \frac{\alpha}{2\pi}\log\left|\frac{1 - a^2z^2}{z^2 - a^2}\right| \qquad (z \in D_0). \tag{6}$$

2. *(u, Ω) is a weak solution to Problem 1.1 and Ω is disconnected if and only if $\frac{\alpha}{2\pi} < c$ and the solution is given by*

$$\begin{cases} \Omega = B\Big(\xi_1, \dfrac{\alpha}{2\pi}\Big) \cup B\Big(\xi_2, \dfrac{\alpha}{2\pi}\Big), \\ u = \begin{cases} \dfrac{\alpha}{2\pi} \log \dfrac{1}{|x-\xi_1|} & \Big(x \in B\Big(\xi_1, \dfrac{\alpha}{2\pi}\Big)\Big) \\ \dfrac{\alpha}{2\pi} \log \dfrac{1}{|x-\xi_2|} & \Big(x \in B\Big(\xi_2, \dfrac{\alpha}{2\pi}\Big)\Big). \end{cases} \end{cases} \tag{7}$$

Proof. Let $\tilde{g}$ be a conformal mapping from $D_0 := \{z \in \mathbb{C} : |z| < 1\}$ to Ω with $\tilde{g}(0) = \xi_1$, and set $\tilde{g}(\xi_2) = be^{i\theta}$ $(0 < b < 1)$. We define $g(z) := \tilde{g}(e^{i\theta_0} z)$ and $f : D_0 \to D_0$ be a Möbius transform. Since $f(a) = 0$ and $f(-a) = b$

$$\begin{aligned} a &:= \frac{1 - \sqrt{1-b^2}}{b} \in (0,1), \\ f(z) &:= \frac{a - z}{1 - az}. \end{aligned}$$

We can define a conformal mapping $\Phi(z) := g(f(z))$ which maps D_0 to the domain Ω with $\Phi(a) = \xi_1$ and $\Phi(-a) = \xi_2$. Set $w(z) = u \circ \Phi(z) = u(\Phi(z))$, then by using the similar argument in the proof of Theorem 2.1, we have

$$\begin{cases} -\Delta w = \alpha\delta_a + \alpha\delta_{-a} & \text{in } D_0 \\ w = 0 & \text{on } \partial D_0 \\ \dfrac{\partial w}{\partial n} = -|\nabla w| = -|\nabla u||\Phi'| = -|\Phi'| & \text{on } \partial D_0. \end{cases} \tag{8}$$

We define

$$w_0(z) := \frac{1}{\alpha} w(z) - E(z-a) - E(z+a) \qquad (z \in D_0).$$

Then $w_0(z)$ becomes a harmonic function in D_0. Since $w(z) = 0$ on the boundary, for $z \in \partial D_0$, we obtain

$$\begin{aligned} w_0(z) &= -E(z-a) - E(z+a) \\ &= \frac{1}{2\pi}(\log|z-a| + \log|z+a|) \\ &= \frac{1}{2\pi} \log|z^2 - a^2| \\ &= \frac{1}{2\pi} \log|1 - a^2 z^2|. \end{aligned}$$

Hence we have $w_0(z) = \frac{1}{2\pi} \log|1 - a^2 z^2|$ in D_0. Then

$$w(z) = \frac{\alpha}{2\pi} \log \frac{1}{|z-a|} + \frac{\alpha}{2\pi} \log \frac{1}{|z+a|} + \frac{\alpha}{2\pi} \log|1 - a^2 z^2| = \frac{\alpha}{2\pi} \log \frac{|1 - a^2 z^2|}{|z^2 - a^2|}.$$

holds. From the third condition of (8), for $z = e^{i\theta} \in \partial D_0$, we have

$$\begin{aligned}
|\Phi'(z)| &= -\frac{\partial w}{\partial n}(z) \\
&= -\frac{\partial}{\partial r} w(re^{i\theta})\Big|_{r=1} \\
&= -\frac{\partial}{\partial r}\left(\frac{\alpha}{2\pi}\log\left|\frac{1-a^2r^2e^{2i\theta}}{r^2e^{2i\theta}-a^2}\right|\right)\Big|_{r=1} \\
&= -\frac{\alpha}{2\pi}\frac{\partial}{\partial r}\left(\log|1-a^2r^2e^{2i\theta}| - \log|r^2e^{2i\theta}-a^2|\right)\Big|_{r=1} \\
&= -\frac{\alpha}{4\pi}\left(\frac{\partial}{\partial r}(\log|1-2a^2r^2\cos 2\theta + a^4r^4| - \log|r^4 - 2a^2r^2\cos 2\theta + a^4|)\right)\Big|_{r=1} \\
&= -\frac{\alpha}{4\pi}\left(\frac{4a^2(a^2-\cos 2\theta) - 4(1-a^2\cos 2\theta)}{|e^{2i\theta}-a^2|^2}\right) \\
&= \frac{\alpha}{\pi}\frac{1-a^4}{|1-a^2z^2|^2}.
\end{aligned}$$

Similarly to the proof of Theorem 2.1, the harmonic function $v(z) := \mathrm{Re}[\log \Phi'(z)]$ in D_0 satisfies

$$v(z) = \mathrm{Re}\Big[\log\Big(\frac{\alpha}{\pi}\frac{1-a^4}{|1-a^2z^2|^2}\Big)\Big] \qquad (z \in \partial D_0).$$

Hence it follows that

$$\log \Phi'(z) = \log(\frac{\alpha}{\pi}\frac{1-a^4}{(1-a^2z^2)^2}) + i\beta \ (z \in D_0),$$

for some $\beta \in \mathbb{R}$. Then we have

$$\Phi'(z) = \frac{\alpha}{\pi}e^{i\beta}\frac{1-a^4}{(1-a^2z^2)^2}. \tag{9}$$

We define

$$\Phi_0(z) = \frac{(1-a^4)}{4\pi a^2}\left[\frac{-2z}{z^2-1/a^2} + a\log\frac{1/a+z}{1/a-z}\right].$$

Then, integrating (9), we have $\Phi(z) = e^{i\beta}\Phi_0(z) + \gamma$, where $\gamma \in \mathbb{C}$. Since $\Phi(\pm a) = \pm c$, using $\Phi_0(a) + \Phi_0(-a) = 0$, we obtain

$$0 = \Phi(a) + \Phi(-a) = e^{i\beta}\alpha(\Phi(a)_0 + \Phi_0(-a)) + 2\gamma = 2\gamma,$$

and $\gamma = 0$. Also from $\Phi_0(a) > 0$ (see Figure 1), $\beta = 0$ follows. Therefore we have

$$\Phi(z) = \Phi_a(z),$$

where $\Phi_a(z)$ is defined in (5).

It is easy to show that (u, Ω) defined in (7) is a solution of Problem 1.1 with μ as in (4) for $\frac{\alpha}{2\pi} < c$. Let us suppose (u, Ω) is a weak solution and Ω is disconnected. Then, from the same

argument of the proof of Theorem 2.1, each open component of Ω should contain ξ_1 or ξ_2 and Ω should have exactly two components Ω_1 and Ω_2 ($\xi_1 \in \Omega_1$, $\xi_2 \in \Omega_2$). Then from Theorem 2.1, we obtain (7). ■

Remark In the Henrot's paper [2], equation (6.5) has a typo. The correct expression of (6.5) is

$$\begin{cases} \Delta v = 0 & \text{in } \Omega_0 \\ v = \log\left(\dfrac{\alpha}{\pi}\dfrac{1-a^4}{|1-a^2z^2|^2}\right) & \text{on } \partial\Omega_0. \end{cases}$$

We define $l = 2c$, based on the conformal mapping Φ_a in (5), we know that $\frac{\alpha}{l} = \frac{1}{2\Phi_0(a)}$. Then we can plot a graph α/l versus a as in Figure 1.

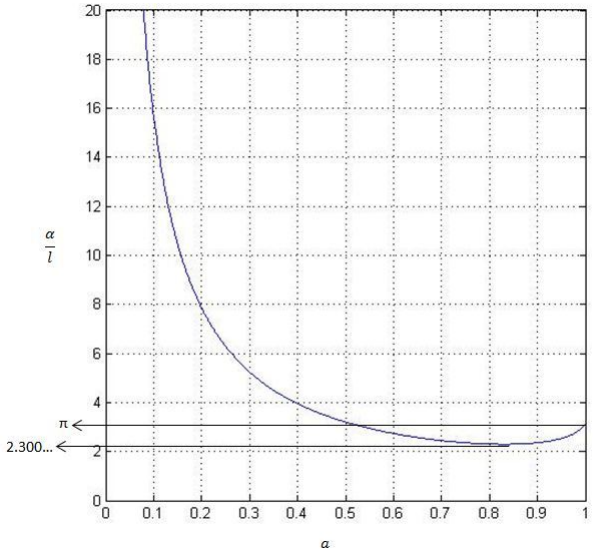

Figure 1: α/l vs a graph

From the graph in Figure 1, we can see that for $2.300.. < \alpha/l < \pi$ there exist two connected solution and that for $\alpha/l > \pi$ there exists a unique solution (which is connected). Table 1 shows the number of the exact solutions of Problem 1.1 where μ as in (3). Although this table was shown in [2], we present it in more detailed form, particularly for the values $\alpha/l = 2.300...$ and $\alpha/l = 2.827....$ According to [2], Ω is convex if and only if $a \leq 1/\sqrt{3}$. We have $\frac{\alpha}{l} = 2.827...$ for $a = 1/\sqrt{3}$.

Table 1: Table of number of the solutions

α/l	0	...	2.300...	...	2.827...	...	π	...
# connected convex solution	0	0	0	0	1	1	1	1
# connected non-convex solution	0	0	1	2	1	1	0	0
# connected solution	0	0	1	2	2	2	1	1
# disconnected solution	0	1	1	1	1	1	0	0

Example of connected solutions are given in Figure 2 - 7 for $\alpha = 3$, where we use MATLAB to draw them. We change $\alpha/l = 2.3007, 2.400, 2.827, 3.000, \pi, 3.300$. Then the number of solutions becomes $1, 2, 2, 2, 1, 1$ for each figure.

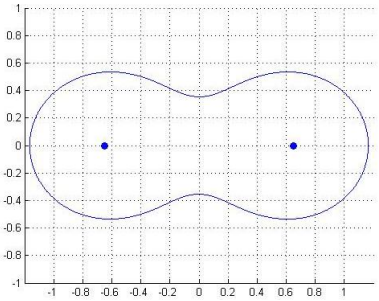

Figure 2: $\alpha/l = 2.300$

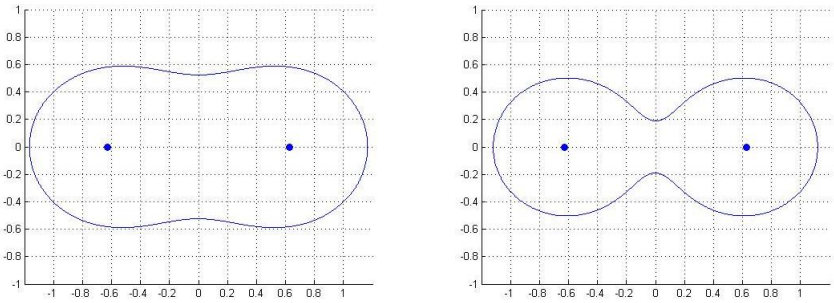

Figure 3: $\alpha/l = 2.400$

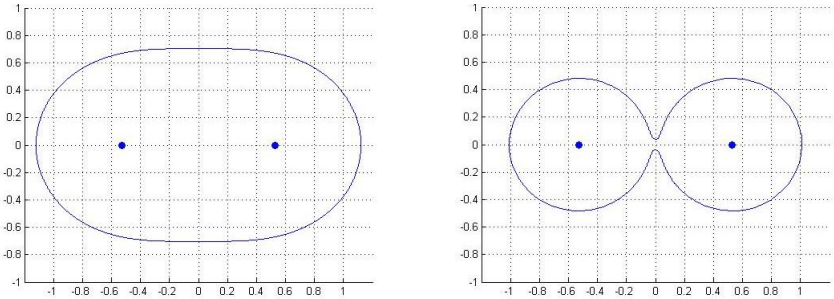

Figure 4: $\alpha/l = 2.827$

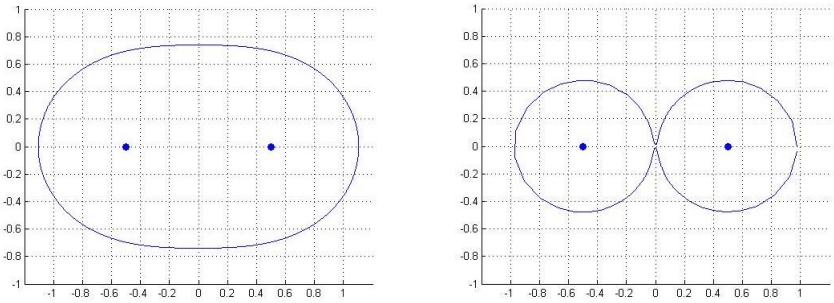

Figure 5: $\alpha/l = 3.000$

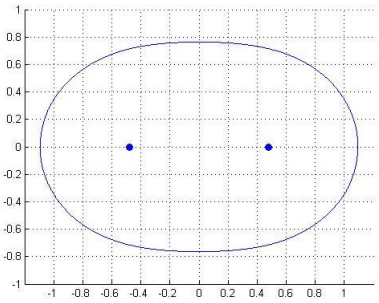

Figure 6: $\alpha/l = \pi$

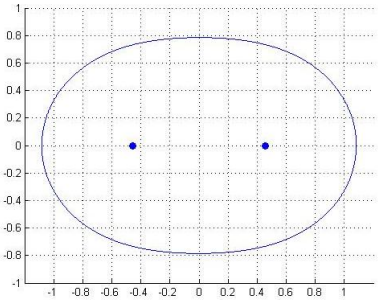

Figure 7: $\alpha/l = 3.300$

3 Shape Optimization Approach

We consider Problem 1.1 with μ as in (4). Then we replace μ by

$$\mu(x) = \alpha\delta^{\varepsilon}(x - \xi_1) + \alpha\delta^{\varepsilon}(x - \xi_2) \tag{10}$$

for sufficiently small $\varepsilon < 0$, where

$$\delta^{\varepsilon}(x) := \begin{cases} \dfrac{1}{\pi\varepsilon^2} & |x| < \varepsilon \\ 0 & |x| \geq \varepsilon. \end{cases}$$

We remark that the problems for $\mu = \alpha(\delta_c + \delta_{-c})$ and for (10) are equivalent except for $u(x)$ in $D := B(\xi_1, \varepsilon) \cup B(\xi_2, \varepsilon)$.

We fix $\beta > 0$, and rewrite Problem 1.1 in the following equivalent form with a Robin boundary condition

$$\begin{cases} -\Delta u = \mu & \text{in } \Omega \\ u = 0 & \text{on } \Gamma \\ \beta u + \dfrac{\partial u}{\partial n} = -1 & \text{on } \Gamma. \end{cases}$$

We define

$$G := \{\Omega \,|\, \Omega \text{ is a bounded domain in } \mathbb{R}^2,\ \bar{D} \subset \Omega,\ \partial\Omega :\ \text{Lipschitz }\}.$$

Then for given $\Omega \in G$ with $\Gamma = \partial\Omega$, we can find a unique solution $u_\Omega \in H^1(\Omega)$ to the following problem

$$u_\Omega : \begin{cases} -\Delta u = \mu & \text{in } \Omega \\ \beta u + \dfrac{\partial u}{\partial n} = -1 & \text{on } \Gamma. \end{cases}$$

If $u_\Omega = 0$ on Γ then (u_Ω, Ω) is a solution for Problem 1.1. Then we define a cost function as follows

$$J(\Omega) = \frac{1}{2}\int_\Gamma |u_\Omega|^2 ds.$$

We want to minimize $J(\Omega)$ among $\Omega \in G$. We remark here that (Ω, u) is a solution if and only if $J(\Omega) = 0$ and $u = u_\Omega$.

4 Variation Formula of Cost Function

We use Lagrange multiplier method [5] to derive the variation formula of cost function $J(\Omega)$ with respect to the domain $\Omega \in G$. For a vector field $\mathbf{V} \in W^{1,\infty}(\mathbb{R}^2, \mathbb{R}^2)$, we define

$$\Omega(t) := \{x + t\mathbf{V}(x) \big| x \in \Omega\} \qquad (0 \le t < t_0).$$

Then we introduce an adjoint problem as follows

$$v_\Omega : \begin{cases} \Delta v = 0 & \text{in } \Omega \\ \beta v + \dfrac{\partial v}{\partial n} = -u_\Omega & \text{on } \Gamma. \end{cases}$$

By using the Lagrange multiplier method and the adjoint problem, under some regularity conditions, we obtain a variation formula of the cost function $J(\Omega)$:

$$\frac{d}{dt}J(\Omega(t))\Big|_{t=0} = \int_\Gamma \Big((\mathbf{V}\cdot\mathbf{n})f + \mathbf{V}\cdot\nabla g + (\mathbf{V}_s\cdot\tau)g\Big)ds, \tag{11}$$

where τ is a counter clockwise tangential unit vector on Γ, $\mathbf{V}_s = \frac{\partial \mathbf{V}}{\partial \tau}$, and

$$f = \nabla u_\Omega \cdot \nabla v_\Omega$$
$$g = \frac{1}{2}u_\Omega^2 + \alpha u_\Omega v_\Omega + v_\Omega.$$

A proof of (11) will be given in our forthcoming paper.

5 Traction Method

The main idea of traction method is to treat the domain Ω as an elastic body and iterate small deformation by a boundary traction given by the variational formula of $J(\Omega)$. In order to solve Problem 1.1 using the traction method, we have to solve the following artificial elasticity problem

$$\begin{cases} -\text{div } \sigma[w] = 0 & \text{in } \Omega \setminus \overline{D} \\ \sigma[w]n = -B & \text{on } \Gamma \\ w = 0 & \text{on } \partial D, \end{cases} \tag{12}$$

where $w(x) \in \mathbb{R}^2$ is a displacement field on $\bar{\Omega}$.

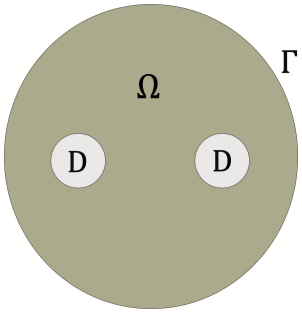

Figure 8: The initial domain

We put B as boundary force, which is implicitly defined by

$$\int_\Gamma B \cdot \mathbf{V} = \frac{d}{dt} J(\Omega(t)) = \int_\Gamma \Big((\mathbf{V} \cdot \mathbf{n}) f + \mathbf{V} \cdot \nabla g + (\mathbf{V}_s \cdot \tau) g \Big) ds \qquad ({}^\forall \mathbf{V} \in \mathrm{W}^{1,\infty}(\mathbb{R}^2, \mathbb{R}^2)).$$

The complete procedure of solving Problem 1.1 by using the traction method can be summarized as follows:

1. Define an initial domain Ω as in figure (8) and generate a finite element mesh on Ω.

2. Solve u_Ω and v_Ω by finite element method.

3. Solve the artificial elasticity problem (12) by finite element method.

4. Modify the domain $\Omega_{new} := \{x + \eta w(x) | x \in \Omega\}$ for sufficiently small $\eta > 0$, together with the nodal points of the mesh.

5. Repeat step 2-4 until the domain Ω converges.

6 Numerical Examples

To study the efficiency of the traction method, we apply it into a free boundary problem as in Problem 1.1 with μ as in (4). Figure 9 shows the numerical result of Problem 1.1 with $\alpha = 3$ and $c = 0.47727$ ($\alpha/l = \pi$) where we use FreeFem++ [3] for the simulation. We also summarize the value of the cost function for some iterations in Table 2.

Table 2: Table of the cost function

Iteration	500	1000	1500	2000	2500	2964
Cost function	0.00355...	0.000273...	0.0000541...	0.0000279...	0.0000218...	0.00000513...

From Table 2 we can see that the cost function becomes smaller with more iterations and it is almost equal to zero ($J(\Omega) = 0.00000513...$) after 2964 iteration.

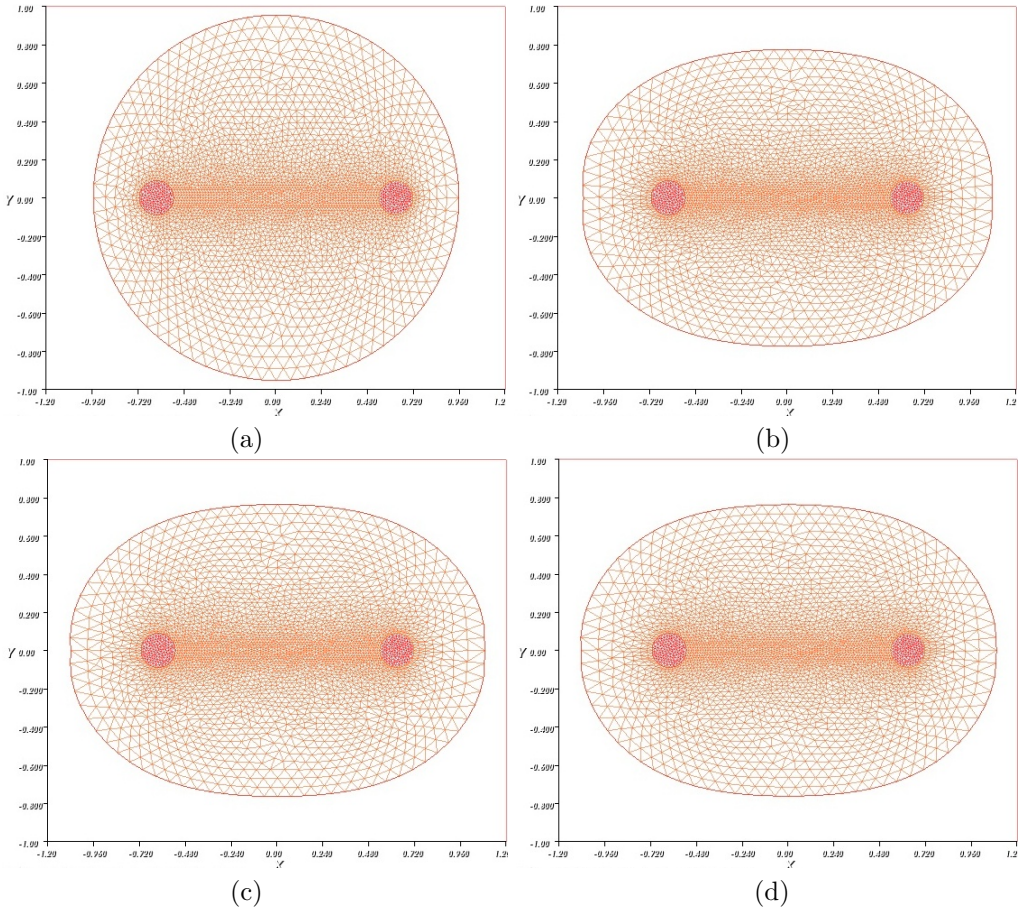

Figure 9: Numerical result of Problem 1.1 with $\alpha = 3$ and $c = 0.47727$ (a) initial domain (b) iteration 1000 (c) iteration 2000 (d) iteration 2964

Comparing with the exact solution in Figure 6, we can observe that the numerical result after 2964 iteration in Figure 9 gives an accurate solution.

7 Conclusion

This paper has presented a complete construction of exact solutions of a free boundary problem by means of the conformal mapping based on the paper of A. Henrot [2]. We could classify all the exact solution into connected/disconnected and convex/non-convex ones and specified the number of each solutions for the case that μ is the combination of two Dirac function as shown in Theorem 2.2 and Table 1. The figures of some exact solutions are also presented in this paper using MATLAB. Hence we can use it as an comparison to the numerical result.

We also solved Problem 1.1 numerically using a shape optimization approach, specifically using the traction method. First we changed the free boundary problem in Problem 1.1 to a shape optimization problem as described in section 3. Then we derived the variation formula of the cost function $J(\Omega)$. Under some regularity, the variation formula in (11) could be obtained using the Lagrange multiplier method and the adjoint problem. The numerical result of Problem 1.1 (where

μ is a combination of two Dirac function with same coefficient α) for $\alpha/l = \pi$ obtained by the traction method was shown in Figure 9. It was observed that by comparing with the exact solution in Figure 6, the traction method could give the numerical result with good accuracy.

Acknowledgment

This research was made possible by Indonesian Directorate General of Higher Education (DGHE) scholarship. We are grateful to the DGHE for the scholarship which enabled one of the authors to undertake a Master double degree program at the Kanazawa University and Institut Teknologi Bandung. The authors also thank Dr. Michiaki Onodera, Kyushu University, who suggested us the reference [2].

References

[1] H. Azegami and K. Takeuchi (2006). A smoothing method for shape optimization: traction method using the robin condition. *International Journal of Computational Methods*, Vol. 3, No. 1, 21 – 33.

[2] A. Henrot (1994). Subsolutions and supersolutions in a free boundary problem. *Ark. Mat.*, **32**, 78 – 98.

[3] F. Hecht (2012). New development in FreeFem++. *J. Numer. Math.*, **20**, no. 3-4, 251265. 65Y15.

[4] D. Gilbarg and N. Trudinger (1998).*Elliptic partial differential equations of second order.* Springer - Verlag, Berlin Heidelberg.

[5] J. Jahn (1996). *Introduction to the theory of non-linear optimization. 2nd rev. ed.*. Springer - Verlag, Berlin New York.

Shallow Water - Navier-Stokes Coupling Method in Ocean Wave Simulation

IRYANTO[a,b]

[a]Graduate School of Natural Sciences and Technology, Kanazawa University, Kakuma, Kanazawa 920-1192 Japan

[b]Faculty of Mathematics and Natural Sciences, Institut Teknologi Bandung, Bandung, Indonesia, E-mail: iryanto.math@gmail.com

Abstract. *Modeling ocean wave propagation using particle method faces difficulty due to its high computational cost, especially when it is computed in large domains. By coupling a cheap model in the large deep sea region and a precise model near the shoreline, we can reduce this difficulty. There had been already proposed models coupling Navier-Stokes equations with a Boussinesq model. Herein we propose to couple a finite difference Shallow Water Equation (SWE) model for the deep sea with a Smoothed Particle Hydrodynamics Navier-Stokes Equation (NSE) model close to the shoreline where the waves break and overturn. The cheap SWE model represents the large computational domain whereas the NSE model is necessary to deal with the complex behavior of the free-surface at the shoreline. We present results of simulations of water waves for a flat bottom and an inclined bottom as a representation of coastal area.*

Keywords: Coupled Model, Ocean Wave Propagation, Navier-Stokes Equations, Shallow Water Equations, Smoothed Particle Hydrodynamics, Staggered Conservative Scheme

1 Introduction

The study of ocean waves is a very important field, including significant applications in coastal engineering, such as tsunami and coastal protection. Many models and numerical methods based on grid and particle approach were proposed to solve ocean wave problems in order to predict the phenomena and prevent devastation.

However, an accurate simulation of the issues still poses a problem, especially when it is computed in a large domain. Particle-based methods can describe the wave behavior, including complex aspects such as the free surface at the shoreline where the waves break and overturn. Nevertheless, these methods still require high computational resources. On the other hand, the computational cost of grid-based methods is cheaper than that of particle methods, but these methods cannot handle the above mentioned complex behaviors.

The computational cost problem can be reduced while keeping the quality of the result by coupling a cheap model for the deep sea with a precise model near the shoreline. The coupled model has been studied recently by several authors. Coupling smoothed particle hydrodynamics (SPH) with a 1-D Boussinesq-type wave model was proposed in [1] and [9].

In this research, we propose to couple a finite difference Shallow Water Equation (SWE) model with a 2-D Smoothed Particle Hydrodynamics Navier-Stokes Equation (NSE) model. The cheap SWE model represents the large computational domain whereas the NSE model is necessary to deal with the complex behavior of the free surface at the shoreline. We use a standard SPH formulation to solve the NSE model and staggered conservative scheme to solve the SWE model.

The purpose of our research is to reduce the computational cost of simulating ocean wave propagation from deep sea by coupling a finite difference shallow water model with a smoothed

particle hydrodynamics Navier-Stokes model. We compare the computational cost of the coupled model with computational cost of the pure Navier-Stokes model.

The outline of this paper is as follows. We introduce our governing equations in section 2. Discretization of the governing equations is explained in section 3. Section 4 is about the coupled model, including coupling strategies and algorithm. In the following section, we present numerical examples of flat and inclined bottom water wave simulations as well as a comparison between the pure SWE model with the coupled model. We summarize our research in the last section.

2 Governing Equations

2.1 Navier-Stokes Equations

The Navier-Stokes equations (NSE) are the basic governing equations for incompressible fluid flow over time t,

$$\begin{cases} \nabla \cdot \mathbf{u} = \mathbf{0} \\ \rho \left(\frac{\partial}{\partial t} + \mathbf{u} \cdot \nabla \right) \mathbf{u} = \nabla p + \mu \nabla \cdot (\nabla \mathbf{u}) + \mathbf{f}, \end{cases} \tag{1}$$

where ρ is the density of the fluid, $\mathbf{u}$ is the velocity, p is the pressure, μ is the viscosity, and $\mathbf{f}$ is the total of external forces acting on the fluid.

We consider inviscid fluid ($\mu = 0$) and assume that the external force comes only from gravity. We solve the governing equations using smoothed particle hydrodynamics, where the fluid is treated as slightly compressible. In this case we can rewrite the equations (1) as follows

$$\begin{cases} \frac{D\rho}{Dt} = -\rho \nabla \cdot \mathbf{u} \\ \frac{D\mathbf{u}}{Dt} = -\frac{1}{\rho} \nabla p + \mathbf{g}, \end{cases} \tag{2}$$

where $\frac{D}{Dt}$ is the material derivative and $\mathbf{g}$ is the gravitational acceleration vector. The equations (2) are also known as Euler equations.

2.2 Shallow Water Equations

The shallow water equations (SWE) are model of fluid flows below a pressure surface (it can be a free surface but it is not necessary). The SWE can be derived from the NSE under the main assumption that the horizontal length scale is much greater than the vertical length scale [6]. As the sea becomes shallower, the vertical velocity of the fluid particles becomes more and more oval-shaped and at the shallow sea level the vertical velocity is assumed to be zero. Another assumption is that the horizontal velocity is homogeneous throughout the whole fluid depth.

We consider one dimensional shallow water equations with no frictional force as follows

$$\begin{cases} \eta_t + (hu)_x = 0 \\ u_t + u u_x + g \eta_x = 0, \end{cases} \tag{3}$$

where η is the fluid level above plane of reference, u is velocity of the fluid, $h = d + \eta$ is total depth of the fluid and d is the fluid depth below plane of reference.

The first equation in the equations (3) comes from mass conservation, whereas the second equation describes momentum conservation.

3 Numerical Method

3.1 Smoothed Particle Hydrodynamics

Smoothed particle hydrodynamics (SPH) is a particle method based on integral approximation using a kernel function that approximates the delta function

$$f(x) = \int_{\Omega} f(x')W\left(x - x'\right) dx', \tag{4}$$

where $x \epsilon \Omega, W$ is a smoothing kernel function with h as width of the kernel (see [2]). The method was proposed by Lucy, Gingold and Monaghan. At first the method was used for simulating astrophysical problems [7], [11]. Nowadays SPH is applied in many fields including wave simulation. The SPH method is convenient for this kind of wave problems since it does not require solving the free boundary.

The main idea of SPH is to discretize the fluid into a finite number of points that have some physical field quantities, e.g., mass-density, pressure, etc. [5]. The movement of the points (particles), depends on its governing equation, i.e., the equations (2). In the SPH method, the approximation of the governing equations is derived using particle approximation.

Unlike grid-based methods that compute spatial derivatives by taking the difference of values at neighboring grid points, the SPH method computes influence of all particles over a certain area depending on the support of the kernel through an integral approximation weighted by the kernel function.

The choice of the kernel function is important in the SPH method, similarly to the choice of schemes in finite difference method [5]. Depending on the situation, some kernel functions can be better than other ones. There are many types of kernel functions but the most common one is the beta cubic spline kernel

$$W\left(x - x', h\right) = \beta \begin{cases} \frac{3}{2} - q^2 + \frac{1}{2}q^3 & 0 \leq q < 1 \\ \frac{1}{6}(2-q)^3 & 1 \leq q < 2 \\ 0 & \text{otherwise} \end{cases}$$

where $q = \frac{|x-x'|}{h}$, $2h$ is the kernel radius (r_{kernel}). The value of β depends on the dimension of the problem, in 2-D case $\beta = \frac{15}{7\pi h^2}$.

To change the integral interpolation into particle approximation, we rewrite the integral (4) into discrete form as follows

$$\langle f(x_i) \rangle \quad = \quad \sum_{j=1}^{N} f(x_j) W_{ij} V_j,$$

where x_i represents the position of i-th particle, $V_j = \frac{m_j}{\rho_j}$ is the volume corresponding to the particle $j, W_{ij} = W(x_i - x_j, h)$, and $\rho_i = \sum_{j=1}^{N} m_j W_{ij}$. The summation is carried out for all neighboring particles in the kernel support.

The particle transformation of the NSE equations (2) results in the set of SPH equations as follows

$$\left\langle \frac{D\rho_i}{Dt} \right\rangle = \sum_{j=1}^{N} m_j \left(\mathbf{u}_i - \mathbf{u}_j\right) \cdot \nabla_i W_{ij}$$

$$\left\langle \frac{D\mathbf{u}_i}{Dt} \right\rangle = -\sum_{j=1}^{N} m_j \left(\frac{p_i + p_j}{\rho_i \rho_j} + \Pi_{ij} \right) \nabla_i W_{ij} + \mathbf{g},$$

where Π_{ij} is artificial viscosity, which is added in order to achieve numerical stability (see [2], [10]). We use artificial viscosity in [5] as follows

$$\Pi_{ij} = \begin{cases} \frac{-a\frac{1}{2}(c_i+c_j)\mu_{ij}+b\mu_{ij}^2}{\frac{1}{2}(\rho_i+\rho_j)} & \text{if } \mathbf{x}_{ij}\cdot\mathbf{u}_{ij}<0 \\ 0 & \text{otherwise} \end{cases}$$

where c_i and c_j are sound speeds of the particle, a and b are constants (typically $b = 0$), $\mathbf{u}_{ij} = (\mathbf{u}_i - \mathbf{u}_j)$, $x_{ij} = (x_i - x_j)$, and

$$\mu_{ij} = \frac{h\mathbf{u}_{ij}\cdot\mathbf{x}_{ij}}{\mathbf{x}_{ij}^2 + (\varepsilon h)^2}$$

with ε a small number, often taken as 0.1 [8].

To update the pressure of particles, we use equation of state that was proposed by Monaghan

$$p_i = B\left(\left(\frac{\rho_i}{\rho_0}\right)^{\gamma} - 1\right),$$

where γ is a constant, often taken as $\gamma = 7$. ρ_0 is the reference density. B is a parameter determining a restriction for the maximum change of density, which is often taken as the initial pressure [2].

3.2 Staggered Conservative Scheme

We use staggered discretizations for solving the equations (3). The scheme is often used in large-scale applications due to its advantages, e.g., its efficiency in combination with semi-implicit time integration (see [3]).

For the discretizations, we follow the ideas in [3] and [4]. In particular, we discrete the time interval $(0, T)$ into N_t time steps with length Δt. The spatial domain $\Omega := (0, L)$ is discretized into N_x cells with length Δx and partition points

$$x_{\frac{1}{2}} = 0, x_1, x_{\frac{3}{2}}, ..., x_{i-\frac{1}{2}}, x_i, x_{i+\frac{1}{2}}, ...x_{Nx+\frac{1}{2}} = L$$

Moreover, we define the depth η at full grid points and the velocity u at half grid points (see Fig.1). Therefore the total depth of the water h is also defined at the full grid.

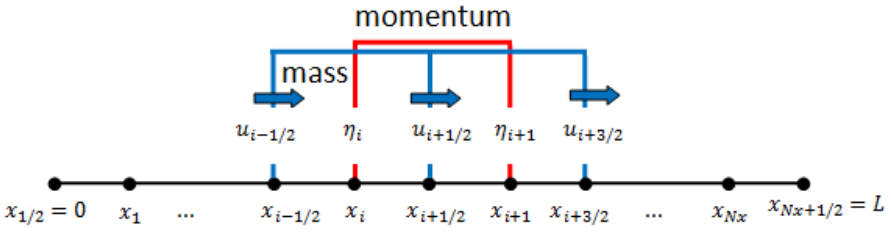

Figure 1: Staggered grid discretization scheme

Applying the scheme to the mass equation of the SWE, we obtain

$$\frac{\eta_i^{n+1}-\eta_i^n}{\Delta t}=-\left(\frac{{}^*h_{i+\frac{1}{2}}^n u_{i+\frac{1}{2}}^n - {}^* h_{i-\frac{1}{2}}^n u_{i-\frac{1}{2}}^n}{\Delta x}\right).$$

The total depth in the discretization of the mass equation appear at half grid but since we define them at full grid, we need to interpolate them. Here we denote by ${}^*h$ the missing points of h at half grid.

We approximate the missing points using first-order upwind scheme. Namely, when the wave comes from the left, we take information from the left side and when the wave comes from the right we take right-side values:

$${}^*h_{i+\frac{1}{2}}=\begin{cases} h_i & if\left(u_{i+\frac{1}{2}}^n \geq 0\right) \\ h_{i+1} & if\left(u_{i+\frac{1}{2}}^n < 0\right). \end{cases} \tag{5}$$

As for the momentum equation of the SWE, we rewrite the nonlinear part in the equations (3) as follows

$$u\frac{\partial u}{\partial x}=\frac{1}{h}\left(\frac{\partial\left(hu^2\right)}{\partial x}-u\frac{\partial\left(hu\right)}{\partial x}\right)=\frac{1}{h}\left(\frac{\partial\left(qu\right)}{\partial x}-u\frac{\partial q}{\partial x}\right).$$

Then, the discretization for the momentum equation is given as follows

$$\frac{u_{i+\frac{1}{2}}^{n+1}-u_{i+\frac{1}{2}}^n}{\Delta t}=-\frac{1}{\overline{h}_{i+\frac{1}{2}}}\left(\frac{\overline{q}_{i+1}u_{i+1}^*-\overline{q}_i u_i^*}{\Delta x}-u_{i+\frac{1}{2}}\frac{\overline{q}_{i+1}-\overline{q}_i}{\Delta x}\right)-g\left(\frac{\eta_{i+1}^{n+1}-\eta_i^{n+1}}{\Delta x}\right),$$

where

$$\overline{h}_{i+\frac{1}{2}}=\frac{h_i+h_{i+1}}{2},\quad \overline{q}_i=\frac{q_{i+\frac{1}{2}}+q_{i-\frac{1}{2}}}{2},\quad q_{i+\frac{1}{2}}={}^* h_{i+\frac{1}{2}}u_{i+\frac{1}{2}}$$

and ${}^*h$ satisfies the equation (5). u^* is the notation for missing points of u on the full grid which are approximated using first-order upwind scheme as follows

$$u_i^*=\begin{cases} u_{i-\frac{1}{2}} & if\left(\ \overline{q}_i \geq 0\right) \\ u_{i+\frac{1}{2}} & if\left(\overline{q}_i < 0\right). \end{cases}$$

Applying both discretizations of the mass and momentum equations, some oscillations will appear in the result. We add an artificial diffusion to smooth out the result:

$${}^*\eta_i^{n+1}=\left(1-\varepsilon\right)\eta_i+0.5\varepsilon\left(\eta_{i-1}+\eta_{i+1}\right) \tag{6}$$

with ε a smoothing parameter. The equation (6) is also known as first order Shapiro filter [6].

4 Coupled Model

4.1 Coupling Idea

The idea to couple the above two sets of governing equations is done by dividing the domain into two regions, SWE Region and NSE Region, with a buffer between these two regions [1], [9] (see Fig.2).

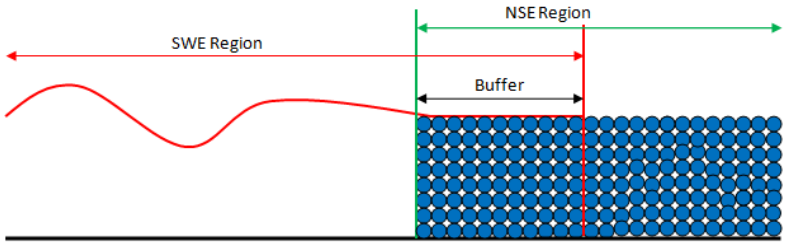

Figure 2: SWE - NSE coupling scheme

The buffer is a place for transferring information between the models. We still need to consider the way of selecting the information to be transferred between the models because of the fact that SWE model provides less information than NSE model.

Basically, we can set the whole computational domain as the SWE region but it will not be effective. Therefore, we choose the SWE region until near shoreline, so that the length of the region is larger than that of the NSE region to represent the large computational domain.

As for the NSE region, we set it up to start from close to the shoreline up to the end of the computational domain in order to deal with the complex behavior of the waves. The selection of the buffer length will be explained in the next section.

4.2 SWE to NSE Coupling

As we know, the SWE is simplified model so it has less information than the NSE model. We obtain homogeneous horizontal velocity for all depths at a given position, whereas the NSE model gives both vertical and horizontal velocity at each point of the domain.

To overcome the lack of information, we insert a wavemaker moving with a velocity given from the SWE model at the left boundary of the NSE region. The wavemaker is created from particles placed in a column as shown in Fig.3

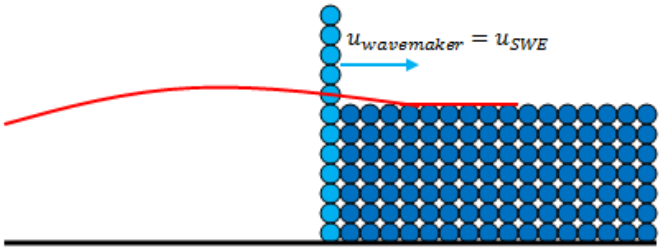

Figure 3: SWE to NSE coupling scheme

We impose the same velocity for every particle of the wavemaker since the SWE has homogeneous velocity. Moreover, the wavemaker moves only in the horizontal direction with the given velocity. In this way, the wavemaker will push the fluid particles and the influence of the SWE will propagate into the NSE through the wavemaker movement. By repeating the process, the influence will propagate over all of the NSE domain.

4.3 NSE to SWE Coupling

From the NSE model we obtain all necessary information for the SWE model. The difficulty in the feedback coupling is in reducing the information when transferring it to the SWE model. Ideally, we want to preserve mass and momentum. In this research, we do it by reconstructing wave-surface and averaging velocity over certain columns in the SPH result.

With the explicit staggered scheme, basically we need only data at one point for the feedback coupling. Hence, we prescribe the SWE boundary condition with the SPH result by taking the information at the right boundary of the SWE model as shown in the Fig.4

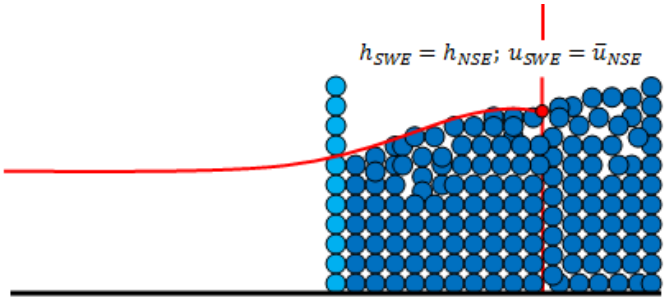

Figure 4: NSE to SWE coupling scheme where both of $\bar{u}_{\mathrm{NSE}}$ and h_{NSE} are computed by averaging particle horizontal velocity and by taking the maximum height of particles in suitable columns.

The choice of the suitable columns depends on parameters used in the SPH. When choosing the columns, we have to ensure that there are always particles in the columns. In our case, the smallest feasible width of the columns was $8\Delta x$, and we compute both $\bar{u}_{\mathrm{NSE}}$ and h_{NSE} over the columns centered on the boundary as follows

$$\begin{aligned} \bar{u}_{\mathrm{NSE}} &= \tfrac{1}{np} \sum_{k=1}^{np} u_1(k), \\ h_{\mathrm{NSE}} &= \max_{1 \le k \le np} y(k) \end{aligned}$$

where np is the number of particles in the column, u_1 is the horizontal velocity of the particles, and y is the vertical position of the particles.

The influence of the NSE model will propagate into the SWE region through the boundary condition. In the first iteration, the influence is at the boundary and the nearest grid from the boundary. By repeating the process, the influence will propagate over all of the SWE domain.

4.4 Coupling Algorithm

In the numerical computation, we have to make sure that the parameters of both models match before start the coupling simulation.

The time step for each model is chosen according to numerical stability requirements. For the SPH, when considering external force and viscous diffusion, the time step of SPH is chosen as follows (see [5])

$$\Delta t_{SPH} = \gamma \min_i \left(\Delta t_f, \Delta t_{cv} \right),$$

where $\Delta t_f = \min_i \left(\frac{h_i}{|\mathbf{f}_i|}\right)$, $\Delta t_{cv} = \min_i \left(\frac{h_i}{c_i + 0.6\left(ac_i + b\max_j \mu_{ij}\right)}\right)$, and $\gamma = 0.25$ or 0.4.
In [2], the time step is also chosen as the ratio between the smallest length of the kernel function and the maximum speed of numerical propagation

$$\Delta t_{SPH} = \min_i \left(\frac{h_i}{c}\right)$$

For the SWE staggered scheme, the CFL condition restricts the time step by the condition

$$\frac{\Delta t_{SWE}}{\Delta x}\left(\sqrt{g^* h^{n+1}_{i+\frac{1}{2}}} + \left|u^n_{i+\frac{1}{2}}\right|\right) \leq 1,$$

where ${}^*h$ satisfies the equation (5). In particular, these conditions usually mean that the SPH time step Δt_{SPH} has to be smaller than the time step for the finite difference method Δt_{SWE}. In our computations we put $\Delta t_{SPH} = 0.5\frac{h}{c}$ and select Δt_{SWE} as large as possible to save computational time.

The coupling algorithm is given as follows

Algorithm 1 Coupled the SWE - NSE algorithm

```
Input values of parameters and initial conditions for both models
for n = 1 ... N_max do
    t = nΔt_SWE
    Solve the SWE region
    Get velocity from SWE model at the SPH boundary
    for j = 1 ... N(N = Δt_SWE/Δt_SPH) do
        Update position of wavemaker
        Solve the NSE region
    Set boundary conditions for the SWE model as in section 4.3
```

5 Result and Discussion

As a numerical example, we simulated water waves on flat and inclined bottoms. The inclined bottom simulation represents coastal area. In this section, we also provide a validation of our model. We assume that the buffer length is large enough to prevent the wavemaker from going out of the buffer. In this simulation, we set the domain for the SWE region, buffer, and the NSE region as follows

$$\Omega_{SWE} := [0, 25], \Omega_{\text{buffer}} := [20, 25], \Omega_{NSE} := [20, 29].$$

Further, we set the constant of artificial viscosity $a = 0.03$, $g = 9.81$, $\Delta x = \frac{h_{\text{kernel}}}{0.9}$ and $\Delta t_{SPH} = \frac{1}{3}\Delta t_{SWE}$. These parameters are used for all cases of our numerical example.

5.1 Model Validation

First, we check the coupling idea by comparing the coupled SWE - SWE model with the pure SWE model. We divide the domain into two regions with a buffer for the coupled model and at

the buffer we transfer both depth and velocity between the models in the same way as in Algorithm 1. The results show that the coupled model and the pure model coincide, as expected.

We adopt our method to compare the coupled SWE - NSE model with pure SWE model. The results are shown in Fig.5.

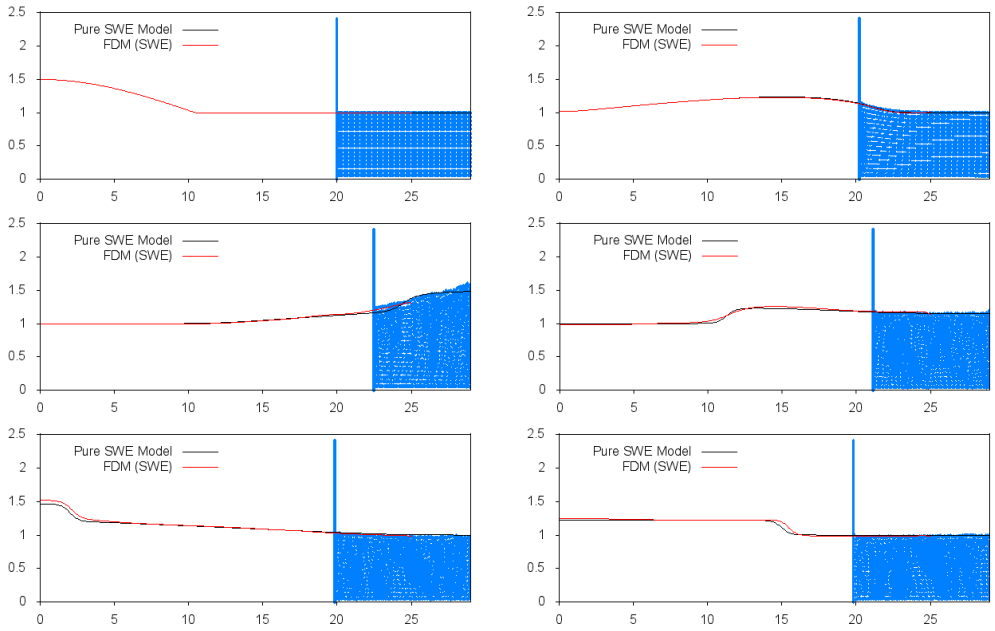

Figure 5: Comparison between the coupled model and the pure SWE model with $h_{\text{kernel}} = 0.0575$.

It is natural that result of the coupled model is different from the pure SWE model since the models are different. However, we can see that the influence of propagation among the models shifts smoothly and the waves resulting from the coupled model and the pure SWE model almost match within the buffer. Therefore, we may say that the result is good.

It is hard to say whether the coupling idea for the SWE - NSE model is correct or not, based only on the comparison method. In order to fully validate the model, it is necessary to compare its results with experimental data. In such a case, we need two-dimensional model for the SWE and three-dimensional model for the NSE.

5.2 Flat Bottom Water Waves Simulation

First, we set $h_{\text{kernel}} = 0.0270588$, obtaining the result shown in Fig.6.

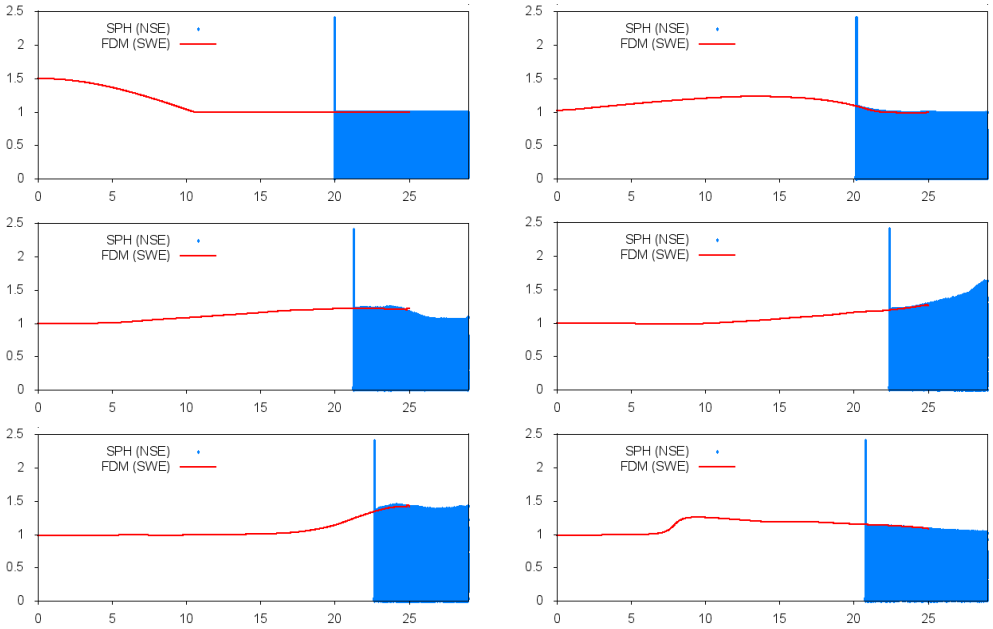

Figure 6: Wave propagation of coupled model at $t = 0, 3.49, 5.24, 6.98, 8.73, 12.23$.

Next, we increase the number of particles two times, which gives a radius of kernel function 0.714 times smaller than in the previous example. The result is shown in Fig.7.

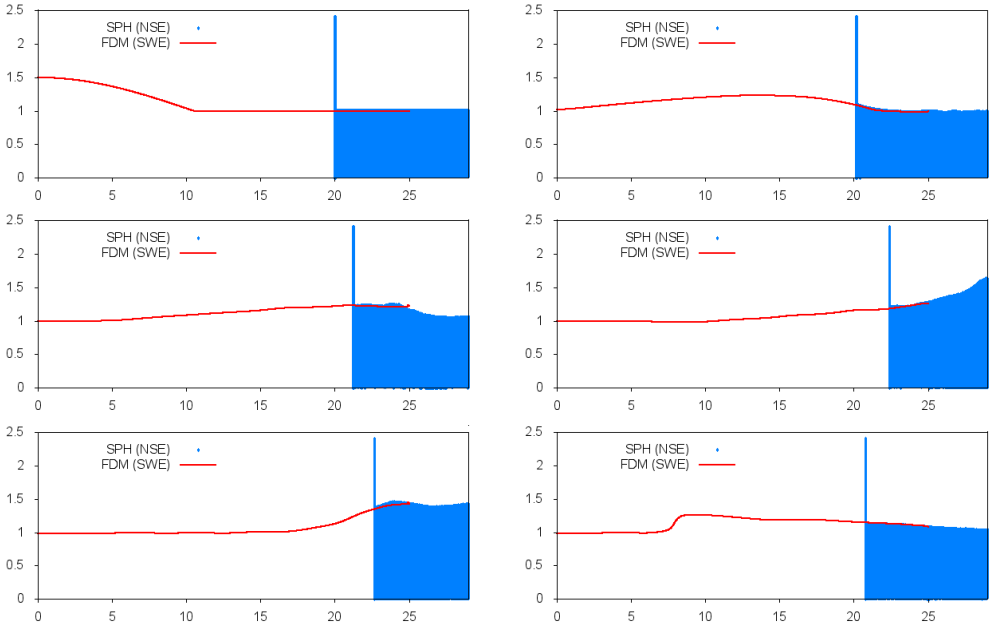

Figure 7: Wave propagation of coupled model with doubled number of particles (at the same time instants as above).

Decreasing the number of particles four times, the length of the kernel increases two times compared to the first case. The corresponding result is shown in Fig.8.

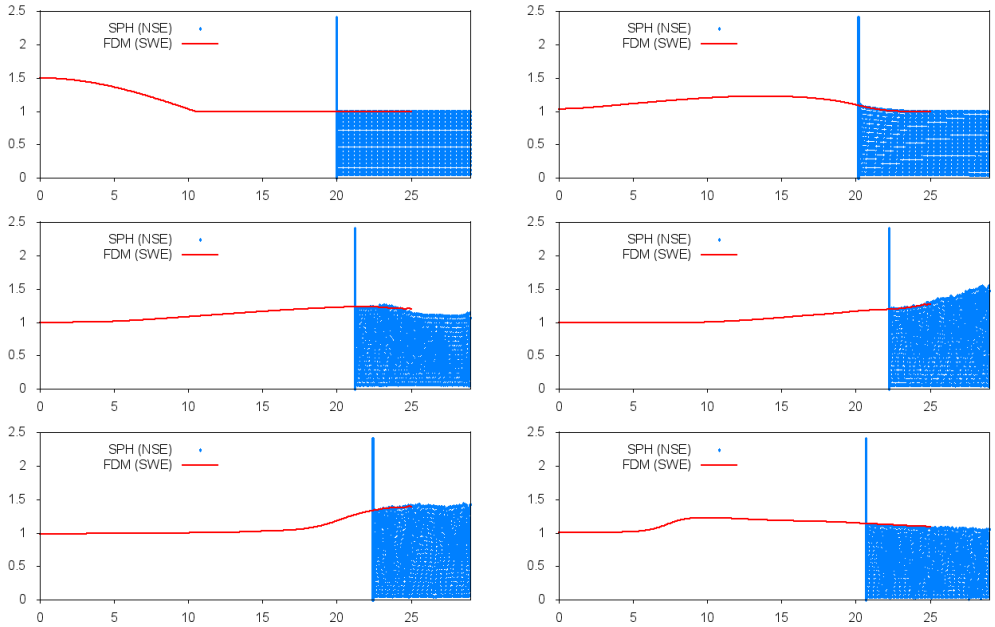

Figure 8: Wave propagation of coupled model with four times smaller number of particles (at the same time instants as above).

As we can see, the results in Fig.6, Fig.7, and Fig.8 do not essentially differ although the resolution of the SPH model was significantly changed. This confirms the correctness of the numerical results.

5.3 Inclined Bottom Water Waves Simulation

For the water wave simulation over inclined bottom, we use the same parameters as in the previous simulation with $h_{\text{kernel}} = 0.046$. The inclination starts from 26.05 with slope $\frac{1}{3}$. The results are shown in Fig.9.

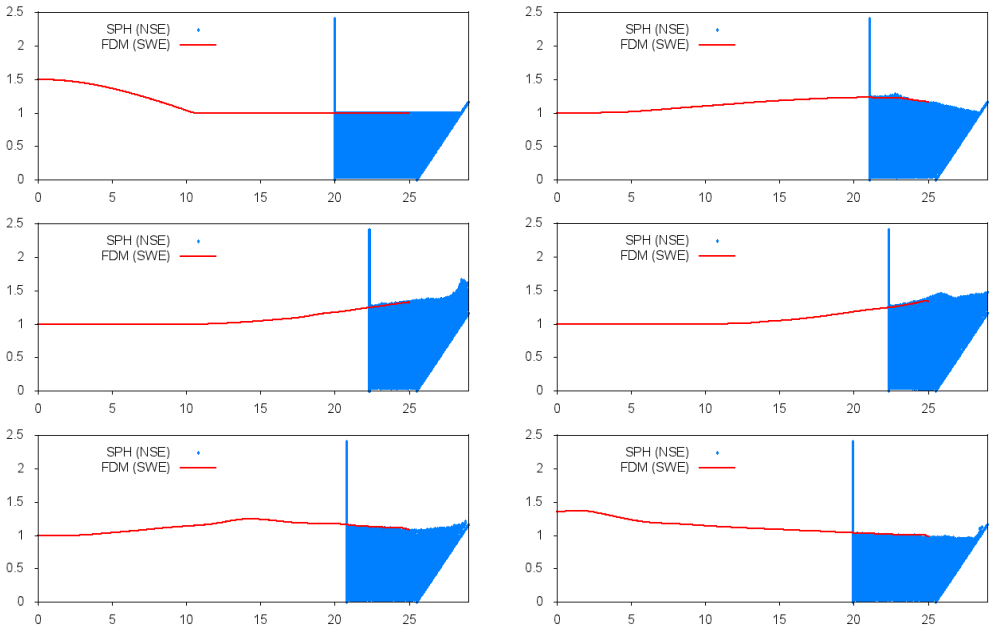

Figure 9: Wave propagation of coupled model at $t = 0, 5.05, 7.42, 8.91, 11.88, 14.85$.

6 Summary

We have presented coupled model between a finite difference Shallow Water Equation (SWE) model and a 2-D Smoothed Particle Hydrodynamics Navier-Stokes Equation (NSE) model. The coupling strategy for SWE to NSE is done by inserting a wavemaker that moves horizontally with velocity given from Shallow Water model. The NSE to SWE coupling is done by reconstructing the wave surface and by averaging velocity over certain columns in the SPH result. The computational speed for the case in Fig.8 was 2.37 times faster than for the pure NSE model, but it is expected to be much more effective for large SWE domains.

Coupling idea with inserting a wavemaker is intuitive. However, in real phenomena there is no such wavemaker that pushes water, therefore the authors would like to consider a more refined coupling idea mentioned in [1] that uses inlet/outlet boundary condition for the SPH method at the buffer for coupling from the SWE to the NSE. We keep this improvement as a future goal.

Acknowledgment

I would like to thank Prof. Karel Svadlenka for helpful discussions, support and guidance during the study.
I would like to thank Prof. Seiro Omata and Prof. Norbert Pozar for helpful discussions.
The work of the author was supported by Japan Student Services Organization (JASSO) Student Exchange Support Program.

References

[1] Christophe Kassiotis, Martin Ferrand, Damien Violeau, Benedict D. Rogers, Peter K. Stansby, and Michel Benoit (2011). Coupling SPH with a 1-D Boussinesq-type wave model, 6^{th} *International SPHERIC Workshop*, Hamburg, Germany, 241 - 247.

[2] G.R. Liu and M.B. Liu (2003). *Smoothed particle hydrodynamics, a meshfree particle method.* World Scientific Publishing, Singapore.

[3] G. S. Stelling and S. P. A. Duinmeijer (2003). A staggered conservative scheme for every Froude number in rapidly varied shallow water flows. *Int. J. Numer. Meth. Fluids*, **43**, 1329 – 1354.

[4] G. Stelling and M. Zijlema (2003). An accurate and efficient finite-difference algorithm for non-hydrostatic free-surface flow with application to wave propagation. *Int. J. Numer. Meth. Fluids*, **43**, 1 – 23.

[5] J.J. Monaghan (1992). Smoothed particle hydrodynamics. *Annu. Rev. Astron. Astrophys.*, **30**, 543 – 574.

[6] Jochen Kämpf (2009). *Ocean Modelling for Beginners.* Springer-Verlag Berlin Heidelberg, Germany.

[7] L.B. Lucy (1977). A numerical approach to the testing of the fission hypothesis. *Astron. J.*, **82**, 1013 – 1024.

[8] L.D. Libersky, A.G. Petschek, T.C. Carney, J.R. Hipp, and F.A. Allahdadi (1993). High strain Lagrangian hydrodynamics. *J. Comput. Phys.*, **109**, 67 – 75.

[9] Muthukumar Narayanaswamy, Alejandro Jacobo Cabrera Crespo, Moncho Gómez-Gesteira, and Robert Anthony Dalrymple (2010). SPHysics - FUNWAVE hybrid model for coastal wave propagation. *Journal of Hydraulic Research*, **48**, 85 – 93.

[10] P.W. Randlesa and L.D. Libersky (1996). Smoothed particle hydrodynamics: some recent improvements and applications. *Comput. Methods Appl. Mech. Engrg.*, **139**, 375 – 408.

[11] R.A. Gingold and J.J. Monaghan (1977). Smoothed particle hydrodynamics: theory and application to non-spherical stars. *Mon. Not. R. Astr. Sot.*, **181**, 375 – 389.

Non-vanishing Terms of the Jones Polynomial

Fuad Yasin[a,b], Kenichi Kawagoe[c]

[a]Graduate Schold of Natural Science and Technology, Kanazawa University, Japan
[b]Faculty of Mathematics and Natural Sciences, Institut Teknologi Bandung, Indonesia
[c]Faculty of Mathematics and Physics, Kanazawa University, Japan

Abstract. *We consider the Tutte polynomial for the graph associated to the* $(2, 2k+1)$ *torus and twist knot. Up to a sign and multiplication by a power of* t *the Jones polynomial* $V_L(t)$ *of an alternating link* L *is equal to the Tutte polynomial* $\chi(G; -t, -t^{-1})$*. Therefore, the Jones polynomial could be calculated by using the Tutte polynomial for* $(2, 2k+1)$ *torus and twist knot. The Jones polynomial has a vanishing term if the knot is a* $(2, 2k+1)$ *torus knot, but there is no vanishing term if the knot is a twist knot. We look for graphs which the associated with 3-tuple of pretzel link have non-vanishing terms in the Jones polynomial. The term Jones polynomial is proven to be non-vanishing by calculated the Tutte polynomial of the given graph.*

Keywords: Graph theory, knot theory, the Tutte polynomial, the Jones polynomial

1 Introduction

A link is a finite family of disjoint, smooth, oriented or unoriented, closed curves in $\mathbb{R}^3$ or equivalently S^3. A knot is a link with one component. Suppose L be an unoriented link, $w(L)$ denotes the writhe of L. We define the normalized bracket polynomial $X(L) = (-A^3)^{-w(L)}\langle L\rangle$. Then, we have the Jones polynomial

$$V_L(t) = (-A^3)^{-w(L)}\langle L\rangle\Big|_{A=t^{-\frac{1}{4}}} \in \mathbb{Z}[t^{\frac{1}{2}}, t^{-\frac{1}{2}}] \tag{1}$$

The torus knot $T(2, 2k+1)$

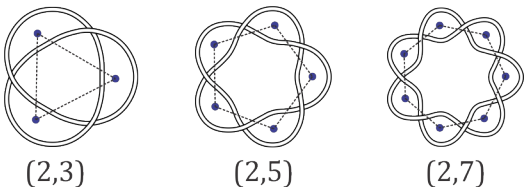

Figure 1: The $(2, 2k+1)$ torus knot, $k = 1, 2, \ldots$

Let G_k be the medial graph of $T(2, 2k+1)$ (Fig. 2).
The Jones polynomial of $T(2, 2k-1)$

$$V_{T(2,2k+1)} = t^k + \sum_{i=1}^{2k}(-1)^{i+1}t^{i+k+1} \tag{2}$$

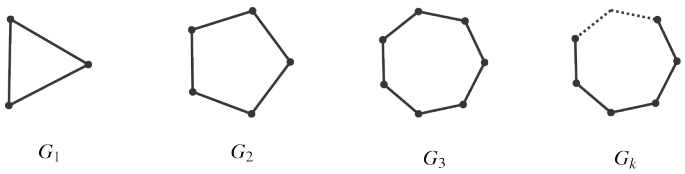

Figure 2: Medial graph of $T(2, 2k + 1)$.

The Jones polynomial of these knot are alternating and has zero coefficient at t^{k+1}. For example:

$$\begin{aligned}
k = 1 &\Rightarrow V_{T(2,3)}(t) = & & & & -t^4 + t^3 & & +t \\
k = 2 &\Rightarrow V_{T(2,5)}(t) = & & & -t^7 + t^6 - t^5 + t^4 & & +t^2 & \\
k = 3 &\Rightarrow V_{T(2,7)}(t) = & -t^{10} + t^9 - t^8 + t^7 - t^6 + t^5 & & & +t^3 & &
\end{aligned}$$

In this paper, we construct the Jones polynomial of an alternating knot which all coefficients are non-zero. We will briefly review the standard theory of the Tutte polynomial and the connection between the Tutte polynomial and the Jones polynomial.

2 Graph Theory

A graph $G = (V(G), E(G))$ or $G = (V, E)$ consists of two finite sets. $V(G)$ or V is the non-empty vertex set of the graph called vertices and $E(G)$ or E is the edge set of the graph called edges, such that each edge e in E is assigned as an unordered pair of vertices (u, v) called the end vertices of e. A path is a sequence of edges which connect a sequence of vertices which are all distinct from one another. A cycle of a graph G is a subset of the edge set of G that forms a path such that the first node of the path corresponds to the last. An isthmus or a bridge is an edge of graph if and only if it is not contained any cycle. A loop is an edge that connects a vertex to itself.

3 The Tutte Polynomial by Deletion-Contraction

Consider the following recursive definition of the function $\chi_G(x, y)$ of a graph G, x, y are independent variables. Then Tutte polynomal is defined by:

$$\chi(G; x, y) = \begin{cases} 1 & \text{if } E(G) = \emptyset \\ x\chi(G'_e; x, y) & \text{if } e \in E \text{ and } e \text{ is an isthmus} \\ y\chi(G''_e; x, y) & \text{if } e \in E \text{ and } e \text{ is a loop} \\ \chi(G; x, y) = \chi_{G'_e}(x, y) + \chi_{G''_e}(x, y) & \text{if e is neither a loop nor an isthmus} \end{cases}$$

where G'_e denotes the deletion by an edge e of graph G and G''_e denotes the contraction by an edge e of graph G.

Example. If G is a complete graph K_3, then

$$\chi(K_3; x, y) = x^2 + x + y$$

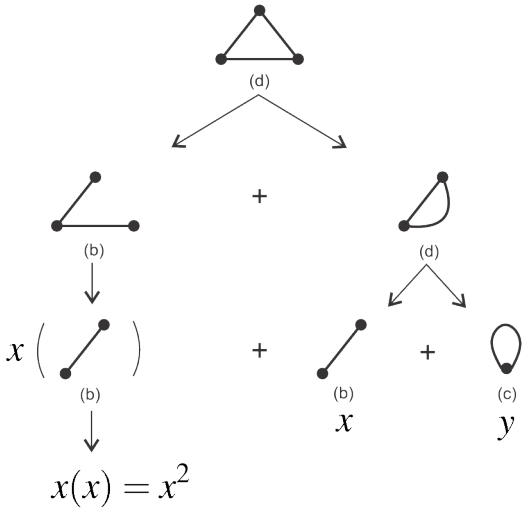

Figure 3: An example of computing the Tutte polynomial of a graph by using deletion and contraction.

Theorem 1. (Thistlethwaite [4]) *Suppose $\phi(t)$ be a sign and multiplication by power of t, Let L be an unoriented link and G be a planar graph associated with L.*
Then, $V_L(t) = \phi(t)\chi(G; -t, -t^{-1})$
Example. Let K be a trefoil knot, G is a medial graph of knot K.

$$\chi(G; x, y) = x^2 + x + y$$
$$\chi(G; -t, -t^{-1}) = t^2 - t - t^{-1}$$

$$V_K(t) = t + t^3 - t^4$$
$$V_K(t) = (-t^2)\chi(G; -t, -t^{-1})$$

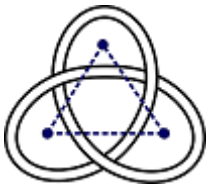

Figure 4: Trefoil knot with its medial graph.

4 The Jones Polynomial of 3-Tuple Pretzel Link

Let $G_{(p,q,r)}$ be a connected planar graph with three number of faces. p, q, and r are the number of vertices of graph $G_{(p,q,r)}$ (Fig. 5). The graph $G_{(p,q,r)}$ is associated with 3-tuple pretzel link.

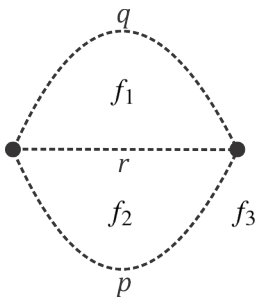

Figure 5: Graph $G_{(p,q,r)}$ with three number of faces f_1, f_2, and f_3

We have the Tutte polynomial of $G_{(p,q,r)}$

$$\chi(G_{(p,q,r)};x,y) = (y-1)^2 + (y-1)\sum_{i=0}^{p} x^i + \sum_{j=0}^{q} x^j \left(y - 1 + \sum_{i=0}^{p} x^i \right) + \sum_{k=0}^{r} \left(x^k y + \sum_{l=0}^{q+p} x^{k+l+1} \right) \quad (3)$$

By changing variable $x = -t$ and $y = -t^{-1}$ from **(3)** we get

$$\begin{aligned} \chi(G_{(p,q,r)};-t,-t^{-1}) = {} & t^{-2} + 2t^{-1} + 1 + (-t^{-1} - 1)\sum_{i=0}^{p}(-t)^i \\ & + \sum_{j=0}^{q}(-t)^j \left(- t^{-1} - 1 + \sum_{i=0}^{p}(-t)^i \right) \\ & + \sum_{k=0}^{r} \left((-t)^{k-1} + \sum_{l=0}^{q+p}(-t)^{k+l+1} \right) \end{aligned} \quad (4)$$

We simplify the Tutte polynomial of $(-t,-t^{-1})$ of graph $G_{(p,q,r)}$

$$\begin{aligned} \chi(G_{(p,q,r)};-t,-t^{-1}) = {} & \frac{1}{t^2(t+1)^2} \\ & \times [1 + t + \{2 - (-t)^p - (-t)^q - (-t)^r\} t^2 \\ & + \{1 - (-t)^p - (-t)^q - (-t)^r\} t^3 \\ & + \{1 - (-t)^p - (-t)^q - (-t)^r\} t^4 \\ & + (-t)^{p+q+r+5}] \end{aligned} \quad (5)$$

So by theorem 1 we get the Jones polynomial of link associated with graph $G_{(p,q,r)}$

$$\begin{aligned} V_L(t) = {} & \frac{\phi(t)}{t^2(t+1)^2} \\ & \times [1 + t + \{2 - (-t)^p - (-t)^q - (-t)^r\} t^2 \\ & + \{1 - (-t)^p - (-t)^q - (-t)^r\} t^3 \\ & + \{1 - (-t)^p - (-t)^q - (-t)^r\} t^4 \\ & + (-t)^{p+q+r+5}] \end{aligned} \quad (6)$$

Where $\phi = (-t^{\frac{3}{4}})^w (t^{-\frac{1}{4}(p+q+r-1)})$ [3]

5 Statement of Results

Theorem 2. *All coefficients in $\chi(G; -t, -t^{-1})$ are non-zero*

Proof. Let $\sum_{i}^{n}(-1)^i a_i t^i$ be a Laurent polynomial with alternating sign and non-vanishing term ($a_i \neq 0$).

Consider $\sum_{i}^{n}(-1)^i a_i t^i \sum_{i}^{m}(-1)^i b_i t^i = \sum_{i}^{m+n}(-1)^i c_i t^i$ and $\sum_{i}^{m}\sum_{i}^{n}(-1)^i a_i t^i = \sum_{i}^{m+n}(-1)^i d_i t^i$.

By using the symmetricity of Tutte polynomial, we will show all coefficients of the polynomial with alternating sign in **(4)** are non-zero if at least p, q, r is greater than zero, assume that $p \leq q \leq r$. Let $r > 0$, we get the Tutte polynomial of $(-t, -t^{-1})$ for graph $G_{(p,q,r)}$

$$\begin{aligned}
\chi(G_{(p,q,r)}; -t, -t^{-1}) &= t^{-2} + 2t^{-1} + 1 + (-t^{-1} - 1)\sum_{i=0}^{p}(-t)^i \\
&\quad + \sum_{j=0}^{q}(-t)^j\Big(- t^{-1} - 1 + \sum_{i=0}^{p}(-t)^i\Big) \\
&\quad + \sum_{k=0}^{r}\Big((-t)^{k-1} + \sum_{l=0}^{q+p}(-t)^{k+l+1}\Big) \\
&= \underbrace{t^{-2} + 1}_{A} + \sum_{i=0}^{p-1}(-t)^i + \sum_{i=0}^{q-1}(-t)^i \\
&\quad + \sum_{j=1}^{q}(-t)^j \sum_{i=1}^{p}(-t)^i + \underbrace{\sum_{k=0}^{r}(-t)^{k-1}}_{B_r} \\
&\quad + \underbrace{\sum_{k=0}^{r}\sum_{l=0}^{q+p}(-t)^{k+l+1}}_{C_{p,q,r}}
\end{aligned}$$

$$\begin{aligned}
A &= t^{-2} + 1 \\
B_r &= - t^{-1} + 1 - t + t^2 - t^3 + \cdots + (-t)^{r-1} \\
C_{p,q,r} &= - t + t^2 - t^3 + \cdots + (-t)^{q+p+1} \\
&\quad + t^2 - t^3 + t^4 + \cdots + (-t)^{q+p+2} \\
&\quad - t^3 + t^4 - t^5 + \cdots + (-t)^{q+p+3} \\
&\quad + (-t)^{r+1} + (-t)^{r+2} + (-t)^{r+3} + \cdots + (-t)^{r+q+p+1}
\end{aligned}$$

All coefficients of polynomial terms $A + B_r + C_{p,q,r}$ are non-zero. Define $\deg^-$ be the lowest degree of its terms. Then, $\deg^-\left(\chi(G_{(p,q,r)}; -t, -t^{-1})\right) = \deg^-(A + B_r + C_{p,q,r}) = -2$ and $\deg\left(\chi(G_{(p,q,r)}; -t, -t^{-1})\right) = \deg(A + B_r + C_{p,q,r}) = r + q + p + 1$. Therefore, all coefficients of polynomial $\chi(G_{(p,q,r)}; -t, -t^{-1})$ are non-zero.□

Corollary 1. *All coefficients in the Jones polynomial of 3-tuple of pretzel link are non-zero.*
Proof. Let L be a 3-tuple of pretzel link.
Consider $\chi(G_{(p,q,r)}; -t, -t^{-1}) = \sum_{i=-2}^{r+q+p+1} (-1)^i a_i t^i$ be the Tutte polynomial with alternating sign and non-vanishing term ($a_i \neq 0$).
Let $\phi(t) = (-1)^h t^k$ be a sign and multiplication by power of t.
Since $V_L(t) = \phi(t)\chi(G_{(p,q,r)}; -t, -t^{-1}) = (-1)^h t^k \sum_{i=-2}^{r+q+p+1} (-1)^i a_i t^i = \sum_{i=-2}^{r+q+p+1} (-1)^{h+i} a_i t^{k+i}$.
Therefore, all coefficients of $V_L(t)$ are non-zero.□
Corollary 2. *All coefficients in the Jones polynomial of n-tuple pretzel link are non-zero.*
Proof. Let $P(c_1, c_2, \ldots, c_n)$ be a pretzel link determined an n-tuple, $G(c_1, c_2, \ldots, c_n)$ is a graph associated with $P(c_1, c_2, \ldots, c_n)$. Choose p, q, r as the first three largest number of $c_1, c_2, \ldots, c_n$ where $p \leq q \leq r$. Then we say that, all coefficients in $\chi(G_{(c_1,c_2,\ldots,c_n)}; -t, -t^{-1})$ are non-zero with $\deg\{\chi(G_{(c_1,c_2,\ldots,c_n)}; -t, -t^{-1})\} = m = r + q + p + 1$.
Let $\phi(t) = (-1)^h t^k$ be a sign and multiplication by power of t.
Since $V_{P(c_1,c_2,\ldots,c_n)}(t) = \phi(t)\chi(G_{(c_1,c_2,\ldots,c_n)}; -t, -t^{-1}) = (-1)^h t^k \sum_{i=-2}^{m} (-1)^i a_i t^i = \sum_{i=-2}^{m} (-1)^{h+i} a_i t^{k+i}$.
Therefore, all coefficients of $V_{P(c_1,c_2,\ldots,c_n)}(t)$ are non-zero.□

Acknowledgment

We would like to thank Japanese Goverment (Monbukagakusho: MEXT) for the financial support in our research.
A special thank to Prof. Hiroshi Iwasaki, Andine Astiany, DDP KU-ITB 2013, our family, Computational Science of ITB and Kanazawa University's lecturers, and Kanazawa University for all the support.

References

[1] N. L. Biggs. The tutte polynomial. *Ch. 13 in Algebraic Graph Theory, 2nd ed.*

[2] Goodall, Andrew. *The Tutte polynomial and related polynomials.* Univerzita Karlova v Praze. 2014.

[3] K. Mimachi. The Jones polynomial and the intersection numbers of twisted cycles associated with selberg type integral. *Journal of Knot Theory and Its Ramifications*, 20(3):469496, 2011.

[4] Morwen B. Thistlethwaite. A spanning tree expansion of the jones polynomial. *Topology*, 26(3):297309, 1986.

New Sliding Puzzle with Neighbors Swap Motion

Prihardono Ariyanto[A,B] Kenichi Kawagoe[C]

Graduate School of Natural Science and Technology, Kanazawa University[A]
Faculty of Mathematics and Natural Sciences, Institut Teknologi Bandung, Email: prihardono.ari@s.itb.ac.id [B]
Faculty of Mathematics and Physics, Kanazawa University [C]

Abstract. *The sliding puzzles (15-puzzle, 8-puzzle, 5-puzzle) are known to have 2 kind of puzzle: solvable puzzle and unsolvable puzzle. In this thesis, we make a new puzzle with only 1 kind of it, solvable puzzle. This new puzzle is made by adopting sliding puzzle with several additional rules from M_{13} puzzle; the puzzle that is formed form The Mathieu group M_{13}. This puzzle has a movement that called a neighbors swap motion, a rule of movement that enables every neighboring points to swap. This extra rule make of new puzzle become possible to be solved, whatever the initial state is.*

Keywords: sliding puzzle, 15-puzzle, 8-puzzle, 5-puzzle, M13 puzzle, neighbors swap motion.

1 Introduction

Sliding puzzle is a puzzle that challenges a player to slide on at pieces along certain routes (usually on a board) to establish a certain end-configuration. Unlike other tour puzzles, a sliding puzzle prohibits lifting any pieces on the board. This property distinguish sliding puzzles from rearrangement puzzles. Hence, finding the movements and the paths open up by each movement within the two-dimensional connes of the board are important parts of solving sliding block puzzles.

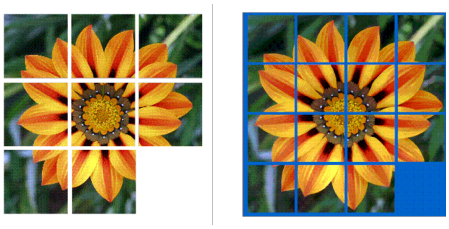

Figure 1: Example of Sliding puzzle (3x3 Sliding Puzzle)

2 15-puzzle

Based on the book written by Edward Hordern in 1986 [4], there is a kind of sliding puzzle that is well known as 15-puzzle. It is a 4x4 square that consists of 15 square tiles in random order and one missing tile. These tiles are numbered from 1 until 15 definitely.

The objective of this game is to set the random tiles to be arranged order by sliding the tiles using the empty space. It is prohibited to lift the tiles, of course. At the end, we will obtain the arrangement of the puzzle with tiles numbered by 1-4 in the first row, 5-8 in the second row, 9-12 in the third row, and 13-15 in the last row added by the empty space.

Generally, there are two type of this puzzle: solvable 15-puzzle and unsolvable 15-puzzle. The unsolvable puzzle is puzzle that have a state that cannot be solved whatever we slide it. Johnson (1879), Story (1879), and Archer (1999) said that the 15-puzzle have state or condition that is impossible to solve. Therefore not all of 15-puzzle can arranged.

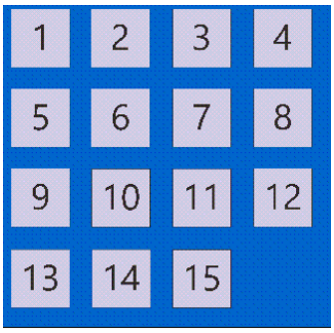

Figure 2: Example of 15-puzzle

3 8-puzzle and 5-puzzle

This sliding puzzle also exists in other size, particularly smaller 8-puzzle and 5-puzzle. Noyes Palmer Chapman is the one who invented and popularized this size of puzzle in 1870s. Similarly with the 15-puzzle, it is also played on a square that consists of some tiles and an empty space, but the size is only 3x3 for 8-puzzle and 2x3 for 5-puzzle. With the purpose of how to solve and the rules are, we have to arrange the tiles by sliding it horizontally or vertically without lifting the tiles, so that they are well ordered (ascending ordered).

Generally, there are two type of this puzzle: solvable puzzle and unsolvable puzzle like 15-puzzle

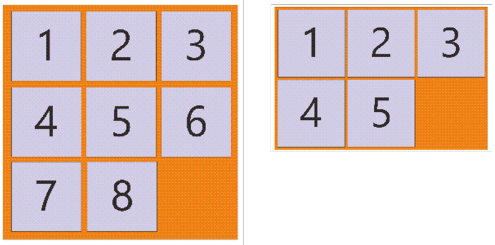

Figure 3: Example of 8-puzzle and 5-puzzle

4 M_{13} Puzzle

M_{13} puzzle is a puzzle that formed form The Mathieu group M_{13}.

M_{13} consists of the permutations of counters that can be obtained by composing finite sequence of moves. This is not a group, since we can only compose two moves if the point left empty after carrying out the first move is the empty point at the start of the second move. More precisely:

the objects of M13 are the 13 positions of the point that's left empty. The morphisms are the permutations of counters that arise from finite sequences of compostable moves.

In How to Play M_{13} by Sebastian Egner and Thomas Beth [3], The Puzzle can be shown as this Figure. The image represent a projective geometry that basic of the M_{13} puzzle. The projective geometry can be thought as the set of one dimensional subspaces of the three dimensional space $\mathbb{F}^3$. A points in this geometry are thirteen one-dimensional subspaces, it indicated by red dot. In addition, the lines at this geometry are thirteen two-dimensional subspaces, it is represented by black triangle. The connection between red dot and triangle is incidence. The red dot is adjacent with triangle if the point is incident to the line.

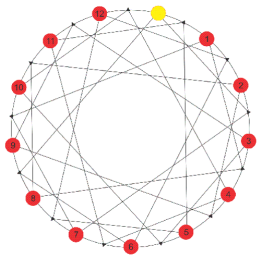

Figure 4: Example of 8-puzzle and 5-puzzle

The puzzle is constructed by putting number 1 until 12 to red dots. The last red dot that doesn't have number called a hole. The basic movement in this puzzle are: 1. Pick a number between 1 and 12, so there is a shortest path to move a number to hole. The path consist one triangle and 2 lines that connect them. so the last state is the picked number became hole and hole became a number that picked before. 2. Exchange the number except a picked number and hole that adjacent to the triangle in the path(from step 1). This movement is called a neighbors swap motion.

The rule in swap motion from M_{13} puzzle swap the adjacency point after we move the target point to the hole. In the M_{13} puzzle we use connectivity between point an triangle, In 8-puzzle and 5-puzzle we use the adjacency between cell.

5 The New 8-puzzle and 5-puzzle

From neighbors swap motion in M_{13} puzzle we can make a new rule with same idea. The idea is a movement that consider with the adjacent with neighbourhood. In this puzzle the rule is adding some extra movement when we slide one of cell.

Assume we move the target cell to empty cell. The movement of new rule is if the number of the cell that is adjacent to the target is 2, the extra movement is swapping between 2 of adjacent cell.

Because 8-puzzle has one more possibilities about number of adjacent cell. Assume we move the target cell to empty cell. The new rule for 8-puzzle become:

1. If the number of the cell that adjacent to the target is 2, the extra movement is swapping between 2 of adjacent cell.
2. If the number of the box that adjacent to the target is 3, the extra movement is swapping only cell that not same row or same column with target cell.

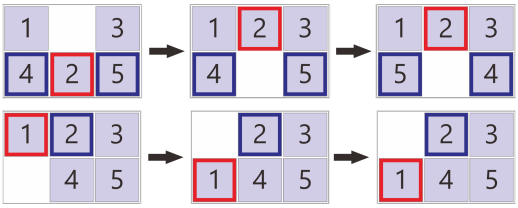

Figure 5: Example of 5-puzzle

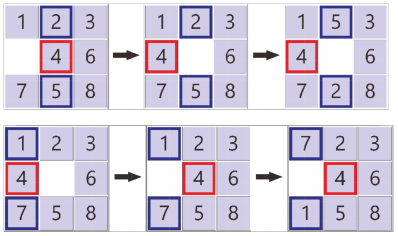

Figure 6: Example of 8-puzzle

6 Solvability of New Puzzle

These new puzzles (new 5-puzzle and new 8-puzzle) can be represented in graph theory as set of vertices and edges. The vertices is a every state of the puzzle (every permutation of the {1,2,3,4,5,0} for 5-puzzle and {1,2,3,4,5,6,7,0} for 8-puzzle) and the edges is the possibilities of the change of the state if we move the hole (0).

Definition 6.1 *$G_5 = (V_5, E_5)$ is a graph with:*

1. *V_5 := Vertices that represent a state of 5-puzzle,*
2. *E_5 := Edges that represent possibility between two state.*

Definition 6.2 *$G_5 = (V_8, E_8)$ is a graph with:*

1. *V_8 := Vertices that represent a state of 8-puzzle,*
2. *E_8 := Edges that represent possibility between two state.*

With this graph we can find there a possible path between every state. This path indicate there exist a movement/s that makes a state became other state. In other word we can find a possibility path from every state to solved state (state when we finished the puzzle). If there exist that path, we can say that state can be solved.

6.1 Solvability of new 5-puzzle

With definition above we get $|V_5| = 720$ and $|E| = 1680$. And with Breadth-first Search (BFS), we can find path of every state that connect it to solved state. The result is G_5 has 720 vertices that have path to solved state. That means every state can be a solve state. In other word we can solve all of new 5-puzzle. Therefore new 5-puzzle didn't have a unsolvable state.

6.2 Solvability of new 8-puzzle

Theorem 6.1 *Every two adjacent cell in new 8-puzzle can be exchanged.*

Let G_8 is a graph representation of state of 8-puzzle. The existence of path in G_8 from vertex v_1 to v_2 means the possibilities movement that can change the state of puzzle that is represented by v_1 to state that is represented by v_2. If the path exist then the movement that can change that state also exists.

Pick 2 cell in 8-puzzle. We will find whether the cell can exchange without change the position of the other cell. 2 cell can exchange if there exists a movement that change the state from original to exchanged state (only 2 cell are changed) or in other words there exists a path from original state vertex to exchanged state vertex. With BFS we can get path that connects that vertices. Because there exist a path for all case so every two adjacent cell in new 8-puzzle can be exchanged.

Theorem 6.2 *Every state of puzzle can be solved.*

Because every two adjacent cell in puzzle can be exchanged, we can exchange any two cells in this puzzle. Therefore we can make a solved state from any state of puzzle.

7 Summary

The regular 5-puzzle and 8-puzzle have 2 types of puzzle: solvable puzzle and unsolvable puzzle. With the rule/movement from M_{13} puzzle (Neighbors swap motion) we can make new 5-puzzle and new 8-puzzle. These puzzles only have one type of puzzle, solvable puzzle.

Acknowledgement

We would like to show our gratitude to the Kenichi Kawagoe's Laboratory for providing invaluable advice, direction, and encouragement during course of our research. For the financial assistance, I would like to thank the Indonesian Government for its Dikti Scholarship.

References

[1] Conway, J. H. (1997). *M13, Surveys in Combinatorics*. London Math. Soc. Lect. Note Series, 241.

[2] Diestel, Reinhard (2005). *Graph Theory (3rd ed. ed.)*. Graduate Texts in Mathematics, vol. 173, Springer-Verlag.

[3] Egner, Sebastian and Beth, Thomas (1998). *How to Play M_{13}*. Designs, Codes and Cryptography, 16, 243247 (1999). Kluwer Academic Publishers, Boston.

[4] Hordern, Edward(1986). *Sliding Piece Puzzles*. Oxford University Press.

[5] Ray, Santanu Saha (2013). *Graph Theory with Algorithms and its Applications-In Applied Science and Technology*. In Applied Science and Technology, Springer India.

Computing general error locator polynomial of 3-error-correcting BCH codes via syndrome varieties using minimal polynomial

Muhammad Zaki Almuzakki[a,b] and Katsuyoshi Ohara[c]

[a]Graduate School of Natural Science and Technology, Kanazawa University, Japan
[b]Faculty of Mathematics and Natural Sciences, Institut Teknologi Bandung, Indonesia, E-mail: muhammad.almuzakki@gmail.com
[c]Faculty of Mathematics and Physics, Kanazawa University, Japan, E-mail: ohara@air.s.kanazawa-u.ac.jp

Abstract. *BCH codes are subclass of cyclic codes with strong properties and have been known for years. In 1994, Chen, Reed, Helleseth, and Truong proposed a decoding procedure for t-error-correcting codes via CRHT syndrome variety using computation of lexicographical Gröbner bases of the ideal. In 2005, Orsini and Sala added polynomial $\chi_{l,\tilde{l}}$, $1 \leq l < \tilde{l} \leq t$, to a system of algebraic equations I to make sure that the position of any two errors are distinct or at least one of them is zero. In 2014, Takuya Fushisato proposed a modified system J to solve 2-error-correcting BCH codes problem. Here the polynomial $\tau_j \in J$ is a divisor of σ_j and contain all possible syndromes of type $0, \alpha^{i_1}, \alpha^{i_1} + \alpha^{i_2} \in \mathbb{F}_{q^m}$ as roots. Generally, τ_j may be regarded as the minimal polynomial of the roots. In this paper, Fushisato's system is generalized into K in which $\Omega_j \in K$ contains all possible roots of t-error-correcting BCH codes in the set $Sol \subseteq \mathbb{F}_{q^m}$. Using the system of polynomials K, the general error locator polynomials of 3-error-correcting codes could be computed and the computation time of some codes were reduced.*

Keywords: BCH codes, t-error-correcting codes, CRHT syndrome variety

1 Introduction

Communication is one of essential components of human beings. The main purpose of a communication system is to deliver any messages effectively from sender to receiver. In a communication system, there are many possibilities that there will be errors due to communication channel. To overcome these problems, researchers develop a field of study named *coding theory*. In general, coding theory deals with the construction of strong codes with good encoding and decoding procedures. Some codes with strong properties are called BCH codes. BCH codes are subclass of cyclic codes in which many algebraic tools can be applied.

Let $\mathbb{F}_{q^m}$ be the splitting field of $x^n - 1$ over $\mathbb{F}_q$. Let $\alpha \in \mathbb{F}_{q^m}$ be a primitive nth root of unity such that

$$\prod_{i=0}^{n-1}(x - \alpha^i) = x^n - 1.$$

A BCH code C can be seen as $\mathbb{F}_q$-kernel of parity-check matrix

$$H = \begin{pmatrix} 1 & \alpha^{i_1} & \alpha^{2i_1} & \dots & \alpha^{(n-1)i_1} \\ 1 & \alpha^{i_2} & \alpha^{2i_2} & \dots & \alpha^{(n-1)i_2} \\ \vdots & \vdots & \vdots & \ddots & \vdots \\ 1 & \alpha^{i_r} & \alpha^{2i_r} & \dots & \alpha^{(n-1)i_r} \end{pmatrix}.$$

Assume that there are errors in the transmission. The errors are collected in an error vector

$$\vec{e} = (e_0 \dots e_{n-1}) = (\underbrace{0 \dots 0}_{k_1-1} \underset{\uparrow}{a_1}_{k_1} 0 \dots 0 \underset{\uparrow}{a_l}_{k_l} 0 \dots 0 \underset{\uparrow}{a_t}_{k_t} \underbrace{0 \dots 0}_{n-k_t-1})$$

where t is the maximum number of errors, $k_1, \dots, k_t$ denote the error location and $a_1, \dots, a_t$ denote the error value. Then the syndrome vector can be computed by multiplying parity-check matrix H with the transpose of error vector $\vec{e}^T$. That is, $\vec{s}^T = H\vec{e}^T$. Every entry s_j of $\vec{s}^T$ can be written in following equation,

$$\sum_{l=1}^{t} a_l (\alpha^{i_j})^{k_l} - s_j = 0,\ 1 \le j \le r \tag{1}$$

To correct errors in a received message, equation 1 needs to be solved. The following notations will be used from now on. Let $X = (x_1 \dots x_r)$ be the syndrome vector $\vec{s}$, $Z = (z_t \dots z_1)$ be the vector which each entries z_l denotes the error location α^{k_l} or zero since there is a possibility that only $\mu \le t$ errors occur (μ is the exact weight of error vectors $\vec{e}$), and $Y = (y_1 \dots y_t)$ be the vector which each entries denotes the error values corresponding to the error locations.

By using X, Y, and Z, equation 1 could be rewritten as

$$f_j : \sum_{l=1}^{t} y_l z_l^{i_j} - x_j = 0,\ 1 \le j \le r \tag{2}$$

In this case, the range of all possible solution is very huge. But from the definitions of errors and syndromes, several equations can be added to restrict the range of the solutions. Chen, Reed, Helleseth, and Truong add following equations to restrict equation 2.

$$\sigma_j : \quad x_j^{q^m} - x_j = 0, \qquad 1 \le j \le r \text{ since } x_j \in \mathbb{F}_{q^m}, \tag{3}$$

$$\eta_i : \quad z_i^{n+1} - z_i = 0, \qquad 1 \le i \le t \text{ since } (\alpha^{i_j})^{k_l} \text{are either } n\text{th roots of unity or zero}, \tag{4}$$

$$\lambda_i : \quad y_i^{q-1} - 1 = 0, \qquad 1 \le i \le t \text{ since } a_l \in \mathbb{F}_q \setminus \{0\}. \tag{5}$$

Equations 2, 3, 4, and 5 are collected in system $F = \{f_j, \sigma_j, \eta_i, \lambda_i \mid 1 \le j \le r,\ 1 \le i \le t\}$. The variety defined by F is then called as CRHT syndrome variety.

The Gröbner bases that is obtained by computing F with respect to a lexicographic ordering probably contains a general error locator polynomial $L(z) = \prod_{l=1}^{\mu}(z - \alpha^{k_l})$ of any BCH codes. This research is focused on building system related to F in order to compute the general error locator polynomial of BCH codes.

2 Orsini-Sala's system

The locations and values of errors in a message can be computed using CRHT syndrome variety. However, the system does not guarantee that every error location is distinct. Therefore, Orsini and Sala add other equation to fix this problem. The equation is of the form,

$$\chi_{l,\tilde{l}} : z_l z_{\tilde{l}} \mathrm{p}(n, z_l, z_{\tilde{l}}) = 0,\ 1 \le l < \tilde{l} \le t \tag{6}$$

Equation 6, together with equations in F then generate the ideal

$$I = \left\langle f_j, \sigma_j, \eta_i, \lambda_i, \chi_{l,\tilde{l}} \;\middle|\; 1 \le j \le r,\ 1 \le i \le t,\ 1 \le l < \tilde{l} \le t \right\rangle$$

which is used to compute the Gröbner bases to find the general error locator polynomial. Suppose that G_I is the reduced Gröbner bases of ideal I with respect to lexicographic ordering, then the polynomial $L_z(X, z_t) \in G_I$ is the general error locator polynomial of code C and is obtained by using Orsini-Sala's system I.

The following algorithm is developed by Orsini and Sala to compute error locations by substituting syndrome $\vec{s}$ to general error locator polynomial $L_z(X, z_t) \in G_I$ and is used to decode messages in the later system.

Algorithm 1 Orsini-Sala decoding algorithm

Input: $\vec{s} = (s_1 \dots s_r)$ and $L_z(X, z_t) = \sum_{i=0}^{t-1} a_i(X) z_t^i + z_t^t \in G$

$\mu \leftarrow t$
while $a_{t-\mu}(\vec{s}) = 0$ **do**
$\mu \leftarrow \mu - 1$
end while

Output: μ and $L_z(\vec{s}, z_t)/(z_t^{t-\mu})$

Note that the algorithm above is used to decode a code after it's general error locator polynomial is found. The general error locator polynomial is computed in the preprocessing of Orsini-Sala's method and is the main object in this research.

3 Fushisato's system

General error locator polynomial of any BCH code C can be computed using Orsini-Sala's system I. However, the complexity of the computation of the Gröbner bases of any system depends on the degrees of polynomials in the system. Thus, it follows that the computation time of the Gröbner bases of Orsini-Sala's system increases exponentially due to σ_j.

Modifying σ_j in Orsini-Sala's system becomes the main problem in order to reduce the amount of computation time since σ_j has the greatest degree among polynomials in the system. It is known that polynomials having syndromes of type $0, \alpha^i, \alpha^i + \alpha^j \in \mathbb{F}_{q^m}$ are sufficient to correct errors in 2-error-correcting codes. To build polynomial with lower degree than σ_j, Fushisato proposes to utilize the minimal polynomials $m_\alpha(x)$ of every syndromes $0, \alpha^i, \alpha^i + \alpha^j \in \mathbb{F}_{q^m}$. That is to take least common multiple of all minimal polynomials of $0, \alpha^i, \alpha^i + \alpha^j \in \mathbb{F}_{q^m}$. Denote the polynomial by τ_j, then it can be written as

$$\tau_j : \operatorname{lcm} \left\{ m_\alpha(x_j) \mid \alpha \in \left\{ 0, \alpha^{i_1}, \alpha^{i_1} + \alpha^{i_2} \right\} \subseteq \mathbb{F}_{q^m} \right\} = 0$$

Denote Fushisato's system formed by changing σ_j to τ_j by

$$J = \left\langle f_j, \tau_j, \eta_i, \lambda_i, \chi_{l,\tilde{l}} \;\middle|\; 1 \le j \le r, 1 \le i \le t, 1 \le l < \tilde{l} \le t \right\rangle.$$

Theorem 3.1. *The reduced Gröbner bases G_J of J with respect to a lexicographical ordering includes a general error locator polynomial for a 2-error-correcting BCH code C.*

Proof. By using theorem 6.8 in [4], simply take $L_z = g_{221}(X, z) \in G_J$ as the general error locator polynomial where $g_{221}(X, z)$ is a polynomial in G_J with leading term $Lt(g_{221}) = z_2^2$ and leading

coefficient $Lc(g_{221}) = 1$ since it satisfies the definition of general error locator polynomial.

Note that Fushisato's system only works on 2-error-correcting codes.

4 t-error syndrome system

Recall the definition of errors and syndromes. Here is a solution set Sol considered as a set containing syndromes associated to errors. Based on the definition, the following statements must be satisfied.

1. If there are no errors, then $0 \in \mathbb{F}_{q^m}$ must be in Sol.
2. If there is 1 error occurs, then Sol must contain syndromes of type $\alpha^{i_1} \in \mathbb{F}_{q^m}$.
3. If there are 2 error occur, then Sol must contain syndromes of type $\alpha^{i_1} + \alpha^{i_2} \in \mathbb{F}_{q^m}$.
4. If there are 3 error occur, then Sol must contain syndromes of type $\alpha^{i_1} + \alpha^{i_2} + \alpha^{i_3} \in \mathbb{F}_{q^m}$.
5. If there are l error occur, then Sol must contain syndromes of type $\sum_{j=1}^{l} \alpha^{i_j} \in \mathbb{F}_{q^m}$.

Since t-error-correcting code means that it can correct up to t errors, it can be concluded that for any t-error-correcting code, the set of all possible syndromes Sol can be written as

$$Sol = \{0\} \bigcup_{l=1}^{t} \left\{ \sum_{j=1}^{l} \alpha^{i_j} \;\middle|\; 0 \leq i_1 < i_2 < \cdots < i_l \leq n-1 \right\} \subseteq \mathbb{F}_{q^m}$$

Definition 4.1. Let $m_\alpha(x)$ be the minimal polynomial of a primitive nth root of unity α. For any t-error-correcting BCH code C, the polynomial with minimum degree containing all possible syndromes for the code in Sol is defined by

$$\Omega_j : \operatorname{lcm} \{ m_\alpha(x_j) \;\mid\; \alpha \in Sol \subseteq \mathbb{F}_{q^m} \} = 0$$

The polynomial Ω_j defined in definition 4.1 can be written in simpler form

$$\Omega_j : \prod_{\alpha \in Sol} (x - \alpha) = 0$$

so that it will be easier to compute.

Definition 4.2. The modified system of t-error-correcting codes formed by changing $\sigma_j \in I$ to Ω_j is called t-error syndrome ideal and defined by

$$K = \left\langle f_j, \Omega_j, \eta_i, \lambda_i, \chi_{l,\tilde{l}} \;\middle|\; 1 \leq j \leq r,\ 1 \leq i \leq t,\ 1 \leq l < \tilde{l} \leq t \right\rangle.$$

Theorem 4.3. *The reduced Gröbner bases G_K of K with respect to a lexicographical ordering includes a general error locator polynomial for a t-error-correcting BCH code C.*

Proof. By using theorem 6.8 in [4], simply take $L_z = g_{tt1}(X, z) \in G_K$ as the general error locator polynomial where $g_{tt1}(X, z)$ is a polynomial in G_K with leading term $Lt(g_{tt1}) = z_t^t$ and leading coefficient $Lc(g_{tt1}) = 1$ since it satisfies the definition of general error locator polynomial.

5 Computation results

Below are the results computed for some 3-error-correcting BCH codes using computer algebraic system Risa/Asir.

1. $n = 19, m = 18, S_C = \{1\}$,
   - Orsini-Sala's system I:
     - $\sigma_j : x_j^{262144} - x_j = 0$,
     - GB computation time: 26.1458 seconds,
   - Modified system K:
     - $\Omega_j : x_j^{1160} + x_j^{1122} + x_j^{1008} + x_j^{970} + x_j^{856} + x_j^{818} + x_j^{780} + x_j^{742} + x_j^{704} + x_j^{666} + x_j^{628} + x_j^{590} + x_j^{552} + x_j^{514} + x_j^{476} + x_j^{457} + x_j^{438} + x_j^{419} + x_j^{324} + x_j^{305} + x_j^{286} + x_j^{248} + x_j^{229} + x_j^{172} + x_j^{153} + x_j^{39} + x_j^{20} + x_j = 0$,
     - GB computation time: 1.18 seconds,
   - general error locator polynomial :
     $L_z = z_3^3 + x_1 z_3^2 + (x_1^{1142} + x_1^{1104} + x_1^{1066} + x_1^{1009} + x_1^{990} + x_1^{952} + x_1^{933} + x_1^{914} + x_1^{876} + x_1^{857} + x_1^{800} + x_1^{781} + x_1^{724} + x_1^{705} + x_1^{648} + x_1^{629} + x_1^{572} + x_1^{553} + x_1^{496} + x_1^{477} + x_1^{439} + x_1^{420} + x_1^{382} + x_1^{363} + x_1^{325} + x_1^{287} + x_1^{268} + x_1^{230} + x_1^{192} + x_1^{154} + x_1^{116} + x_1^2) z_3 + x_1^{1143} + x_1^{1105} + x_1^{1067} + x_1^{991} + x_1^{953} + x_1^{915} + x_1^{877} + x_1^{820} + x_1^{801} + x_1^{744} + x_1^{725} + x_1^{668} + x_1^{649} + x_1^{592} + x_1^{573} + x_1^{516} + x_1^{497} + x_1^{421} + x_1^{402} + x_1^{383} + x_1^{307} + x_1^{288} + x_1^{269} + x_1^{212} + x_1^{117} + x_1^{98} + x_1^{79} + x_1^{60}$.
2. $n = 37, m = 36, S_C = \{1\}$,
   - Orsini-Sala's system I:
     - $\deg(\sigma_j) = 68719476736$,
     - GB computation time: almost impossible to compute the Gröbner bases of this system,
   - Modified system K:
     - $\deg(\Omega_j) = 8474$,
     - GB computation time: 216.644 seconds,
   - general error locator polynomial :
     $L_z = z_3^3 + x_1 z_3^2 + (x_1^{8438} + x_1^{8401} + x_1^{8364} + x_1^{8253} + x_1^{8216} + x_1^{8179} + x_1^{8068} + x_1^{8031} + x_1^{7994} + x_1^{7920} + x_1^{7883} + x_1^{7735} + x_1^{7698} + x_1^{7661} + x_1^{7550} + x_1^{7365} + x_1^{7291} + x_1^{7069} + x_1^{7032} + x_1^{6995} + x_1^{6958} + x_1^{6847} + x_1^{6810} + x_1^{6736} + x_1^{6551} + x_1^{6440} + x_1^{6403} + x_1^{6366} + x_1^{6255} + x_1^{6181} + x_1^{6107} + x_1^{6070} + x_1^{6033} + x_1^{5996} + x_1^{5922} + x_1^{5848} + x_1^{5774} + x_1^{5700} + x_1^{5552} + x_1^{5478} + x_1^{5441} + x_1^{5404} + x_1^{5367} + x_1^{5293} + x_1^{5145} + x_1^{5108} + x_1^{5071} + x_1^{4923} + x_1^{4849} + x_1^{4738} + x_1^{4701} + x_1^{4627} + x_1^{4590} + x_1^{4516} + x_1^{4479} + x_1^{4368} + x_1^{4257} + x_1^{4146} + x_1^{4109} + x_1^{4035} + x_1^{3998} + x_1^{3961} + x_1^{3924} + x_1^{3887} + x_1^{3850} + x_1^{3813} + x_1^{3702} + x_1^{3628} + x_1^{3591} + x_1^{3443} + x_1^{3406} + x_1^{3295} + x_1^{3258} + x_1^{3073} + x_1^{3036} + x_1^{2962} + x_1^{2925} + x_1^{2888} + x_1^{2851} + x_1^{2814} + x_1^{2740} + x_1^{2703} + x_1^{2555} + x_1^{2370} + x_1^{2296} + x_1^{2185} + x_1^{2111} + x_1^{2074} + x_1^{2037} + x_1^{2000} + x_1^{1963} + x_1^{1889} + x_1^{1815} + x_1^{1556} + x_1^{1445} + x_1^{1408} + x_1^{1371} + x_1^{1297} + x_1^{1260} + x_1^{1223} + x_1^{1112} + x_1^{1038} + x_1^{964} + x_1^{927} + x_1^{890} + x_1^{742} + x_1^{668} + x_1^{631} + x_1^{557} + x_1^{520} + x_1^{298} + x_1^{261} + x_1^{224} + x_1^{187} + x_1^{76} + x_1^2) z_3 + x_1^{8439} + x_1^{8365} + x_1^{8069} + x_1^{7995} + x_1^{7958} + x_1^{7884} + x_1^{7847} + x_1^{7773} + x_1^{7736} + x_1^{7514} + x_1^{7477} + x_1^{7329} + x_1^{7255} + x_1^{7181} + x_1^{7144} + x_1^{7107} + x_1^{7070} + x_1^{7033} + x_1^{6996} + x_1^{6885} + x_1^{6848} + x_1^{6663} + x_1^{6515} + x_1^{6478} + x_1^{6441} + x_1^{6404} + x_1^{6330} + x_1^{6145} + x_1^{6108} + x_1^{6034} + x_1^{5923} + x_1^{5886} + x_1^{5590} + x_1^{5553} + x_1^{5479} + x_1^{5331} +$

$$x_1^{5257}+x_1^{5220}+x_1^{4998}+x_1^{4961}+x_1^{4924}+x_1^{4887}+x_1^{4850}+x_1^{4776}+x_1^{4702}+x_1^{4665}+x_1^{4628}+x_1^{4443}+$$
$$x_1^{4406}+x_1^{4369}+x_1^{4332}+x_1^{4295}+x_1^{4258}+x_1^{4221}+x_1^{4184}+x_1^{4110}+x_1^{4073}+x_1^{3999}+x_1^{3740}+x_1^{3703}+$$
$$x_1^{3666}+x_1^{3629}+x_1^{3370}+x_1^{3333}+x_1^{3296}+x_1^{3148}+x_1^{3074}+x_1^{3037}+x_1^{3000}+x_1^{2926}+x_1^{2889}+x_1^{2815}+$$
$$x_1^{2630}+x_1^{2593}+x_1^{2556}+x_1^{2519}+x_1^{2408}+x_1^{2260}+x_1^{2223}+x_1^{2149}+x_1^{2075}+x_1^{2001}+x_1^{1964}+x_1^{1890}+$$
$$x_1^{1853}+x_1^{1742}+x_1^{1705}+x_1^{1668}+x_1^{1594}+x_1^{1520}+x_1^{1483}+x_1^{1446}+x_1^{1335}+x_1^{1298}+x_1^{1187}+x_1^{1113}+$$
$$x_1^{1002}+x_1^{891}+x_1^{854}+x_1^{817}+x_1^{743}+x_1^{669}+x_1^{484}+x_1^{373}+x_1^{336}+x_1^{299}+x_1^{262}+x_1^{188}+x_1^{77}+x_1^{40}.$$

3. $n = 61, m = 60, S_C = \{1\}$,
   - Orsini-Sala's system I:
     - $\deg(\sigma_j) = 1152921504606846976$,
     - GB computation time: almost impossible to compute the Gröbner bases of this system,
   - Modified system K:
     - $\deg(\Omega_j) = 37882$,
     - GB computation time: 1564.78 seconds,
   - The general error locator polynomial is a huge polynomial.

6 Summary

The system K is sufficient to obtain the general error locator polynomial of t-error-correcting BCH codes since $\Omega_j \in K$ contain all possible syndromes for the codes. In this paper, the general error locator polynomial of 3-error-correcting BCH codes can be obtained and the amount of computation time of the lexicographic Gröbner bases is greatly reduced.

Acknowledgment

The researchers would like to thank Japan student service organization (JASSO) for the financial support in the research, to all previous researchers in these topics, and to the developer of strong computer algebraic system Risa/Asir. Also thank to researchers's family, DDP KU-ITB 2013's students, computational science of ITB and Kanazawa University's lecturers, all Indonesian people in Ishikawa, Pudy Kusumaningrum, and Kanazawa University for all the support.

References

[1] Fushisato, T., A BCH decoding algorithm using the Gröbner bases of a polynomial ideal. Master's thesis, Kanazawa University, January 2014. (in Japanese)

[2] Fushisato, T., Ohara, K., Effective computation of general error locator polynomials of binary BCH codes with $t = 2$, in preparation.

[3] Miyake, S., On decoding algorithm for cyclic codes using Gröbner bases. Master's thesis, Kobe University, February 2012. (in Japanese)

[4] Orsini, E., Sala, M., Correcting errors and erasures via the syndrome variety. Journal of Pure and Applied Algebra **200** (2005), 191-226.

First-principles Study of Hydrogen Impurity in GaN

Dinan Andiwijayakusuma[a,b], Fumiyuki Ishii[a], Mineo Saito[a]

[a]Division of Mathematical and Physical Science, Graduate School of Mathematics and Physics, Kanazawa University, Japan

[b]Faculty of Mathematics and Natural Sciences, Bandung Institute of Technology

E-mail: dandiwijaya@cphys.s.kanazawa-u.ac.jp

Abstract. *Gallium nitride (GaN) is a wide-band gap (Eg=3.4eV) semiconductor and is a candidate for high-power devices. As an impurity, hydrogen (H) plays an important role in GaN-based devices. We perform first-principles calculations to investigate the stable geometry of H impurity. We carry out the density-functional calculations within the generalized gradient approximation (GGA) using PHASE/0. We find that the bond-center site is the most stable site for H^+, whereas the trigonal channel at the center of wurtzite, where the hydrogen has three nearest Ga atoms, is the most stable for H^0 and H^-, which is consistent with the results of past theoretical studies. We discuss some details of optimized geometries and find that these geometries does not contradict with the results of μSR. We confirm that the present supercell model well describes the impurity state and conclude that the hydrogen impurity has a negative-U property in GaN, which is consistent with the past theoretical studies*

Keywords: Hydrogen, GaN, impurity

1 Introduction

Gallium nitride (GaN) is an important semiconductor after silicon. Its wide-band gap of 3.4 eV affords its special properties for applications in electronic and optoelectronic devices, i.e bright, highly efficient blue and green light-emitting diodes (LED) [1]. The photons of the emitted light have an energy similar to the value of the energy gap. GaN also is a direct band-gap. In the case of direct band gap, the optical transitions across the bandgap are "allowed" and therefore much stronger than indirect bandgaps, so the direct band gap give more light emittion than indirect band gap semiconduntor. With these advantages, GaN-based LED have started to replace light bulbs and fluorescent tubes, which means more efficiency in energy and cost reductions.

The semiconductor LED require *pn*-junction, i.e junction between *p*-type and *n*-type. However, when crystal GaN is grown by common growth techniques, it exhibits n-types conductivity. The *p*-type conductivity of GaN was initially difficult to obtain, but Akasaki and Nakamura et.al have solved it by thermal annealing and reveal that hydrogen is the important key of this problem [2,3]. Hydrogen as a common impurity in semiconductor shows very complex behavior. It has a big influence on mechanical and optoelectronic properties of several semiconductor because of its ability to passivate and compensate both shallow and deep defects. It acts as amphoteric impurity in semiconductor, which means hydrogen can acts as a donor or an acceptor [4]. Large concentrations of hydrogen appear in many semiconductor growth techniques, such as metal-organic chemical deposition (MOCVD) or hydride vapor phase epitaxy (HVPE).

In most stages of GaN-based devices fabrication are influenced by hydrogen. The hydrogen incorporated during growth of GaN to passivation the acceptors, and also in postgrowth to render the acepptors electrically active [5]. In the other words, the hydrogen atoms plays an important role in most processing step of GaN-base devices. With the role of hydrogen in GaN, it seem

to be necessary to study and investigate the relevant behavior of hydrogen in GaN. The goal of this first-principles study is to investigate the stability of hydrogen impurity in wurtzite GaN. We find the most stable geometry of hydrogen impurity in GaN and compare the stability of either positively or negatively charged states of the hydrogen atom with the neutral charge in GaN.

2 Computational Method

There are three geometry crystal structures for GaN : the wurtzite, the rocksalt and the zinc-blende (cubic). In this work, we focus on the wurtzite, which is the most stable one for bulk GaN. In order to examine the hydrogen impurity in GaN, we consider a model of one hydrogen atom in 72 atoms GaN supercell to investigate the stability geometry for charge-state of hydrogen in GaN. We carry out the first-principles calculation using PHASE/0 code, within the framework of the Generalized Gradient Approximation (GGA) and the ultrasoft pseudo-potentials. The convergence tests of the total energy with respect to the planewave energy cutoff and k-point sampling have been carefully examined. In the calculation based on the PHASE/0 the cut-off energies of the wave function and charge density are 25 and 225 Ry, respectively. A supercell geometry containing 72 host atoms, and a set of k points generated by the 2x2x2 mesh for Brillouin-zone integration. The energy convergence is within 1.0e-03 Hartree/Bohr, and remaining force in the optimized geometries is within 1.0e-03 Hartree/Bohr.

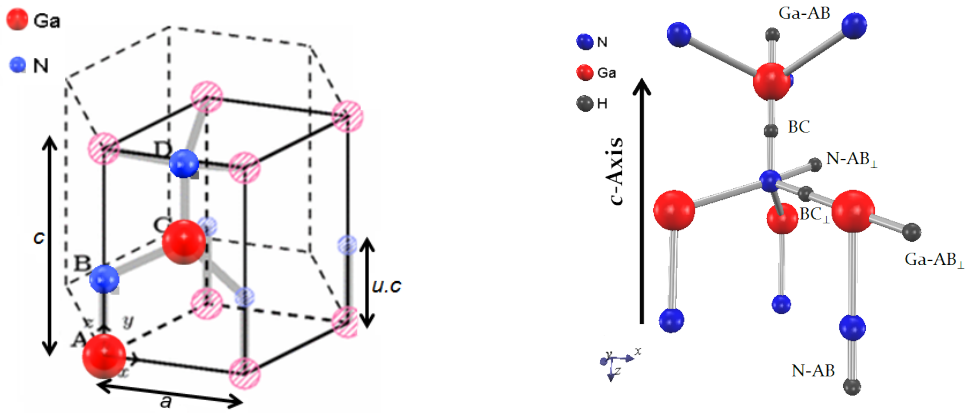

(a) Wurtzite unitcell

(b) Possible position of H in GaN

Figure 1: (a) Wurtzite unit cell of GaN consist of two atoms gallium and two atoms nitrogen, with lattice parameter a and c also the internal parameter u. (b) GaN geometry structure with six possible locations where hydrogen atom may reside, they are Ga-AB$_\perp$, Ga-AB$_\parallel$, N-AB$_\perp$, N-AB$_\parallel$, BC$_\perp$, and BC$_\parallel$,

3 Results and Discussions

3.1 The Optimized Wurtzite Structure

To study the influence of hydrogen impurity on the properties of GaN, stable structure of the wurtzite GaN has to be determined. As we can see at Fig. 1a, for wurtzite there are four atoms

per hexagonal unit cell. The unit vectors are $\overrightarrow{a_1}$=(a,0,0),$\overrightarrow{a_2}$=(a/2,$a\sqrt{3/2}$,0), and $\overrightarrow{a_3}$=(0,0,c), where a and c are the wurtzite lattice constants. The positions of gallium atom are (1/3,2/3,0) and (2/3,1/3,1/2) while the nitrogen atom positions are (1/3,2/3,u) and (2/3,1/3,1/2+u), where u is internal parameter. In the ideal wurtzite structure, the value of u is constant (u=3/8) and c/a =$1/\sqrt{u}$, all four nearest-neighbor distances are equal and all bond angles are ideal tetrahedral angles (109.5).

In present work, to get the stable structure, we calculate equilibrium geometry of the wurtzite phase, following the procedure outlined in [6]. First step, we use ideal wurtzite geometry parameter and we vary the lattice constant a to get the equilibrium of a. After that, we vary the c/a ratio while we keep the last lattice constant a and internal parameter u is ideal, we get the new c/a value. With the new c/a, we vary the lattice constant a to determine new equilibrium of lattice constant a. Finally we vary the internal parameter u by keep the value of a and c/a ratio, so we can get the equilibrium of all parameter in wurtzite geometry including u.

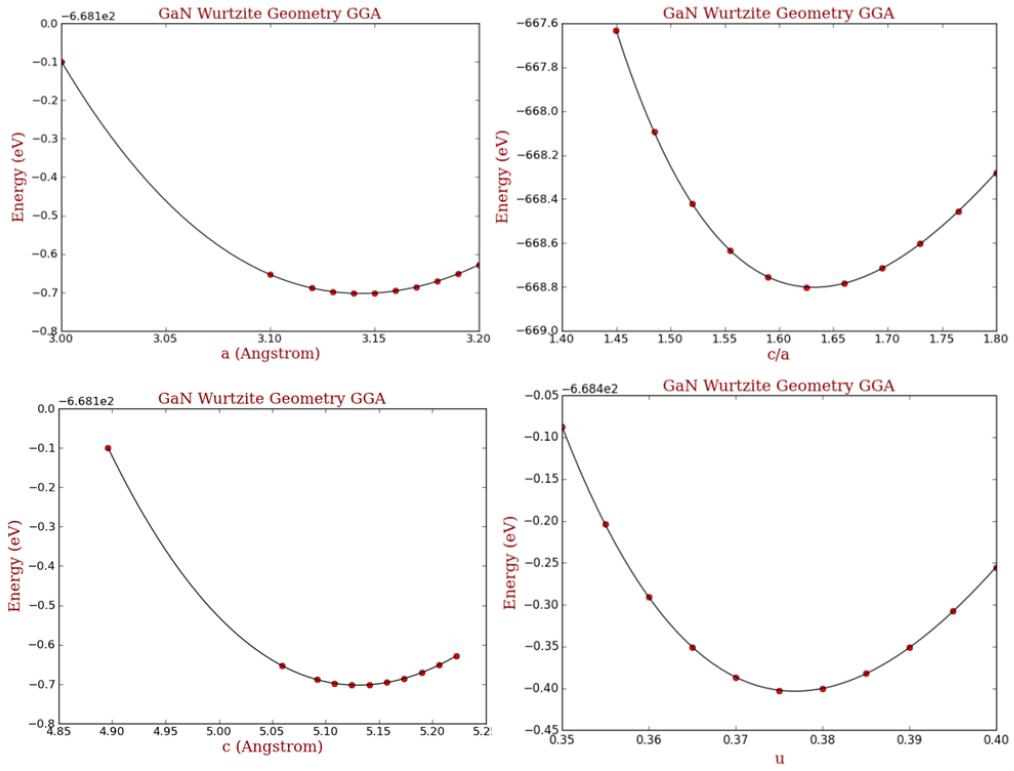

Figure 2: Total energy as a function of the latice constant a and c, c/a ratio and u for wurtzite GaN

Table 1 compares the values of the equilibrium lattice constants a, c, and of the internal parameter u resulting from the present calculation with a collection of experimental and theoretical values available in the literature. In Fig. 2, we plot the total energy versus lattice constant a,c, the c/a ratios and the internal structural parameter. With respect to experiment, our calculation lattice constant a and c as obtained using GGA is smaller by 1.16% and 0.69% respectively. After we get the stable structure, we examined several interstitial configurations of H. The equilibrium position

Table 1: Lattice constants a and c, c/a, internal parameter u of wurtzite GaN obtained in this works, previous theoritical calculations and experimen

Parameter	This Work	Calculations [6] [7] [8]	Experiment [6] [7] [8]
a(Å)	3.143	3.124 – 3.245	3.180 – 3.192
c(Å)	5.130	5.0 – 5.228	5.166 – 5.185
c/a	1.632	1.628 – 1.632	1.624 – 1.627
u	0.377	0.375 – 0.376	0.375 – 0.377

of H atom in the supercell of GaN is determined by the geometry optimizations with different initial positions of the H atom. Many possible sites for interstitial hydrogen were investigated for the three states, H^+, H^0, and H^-, were calculated at each site. There are six possibilities position of H atom in the supercell, as we can see at the Fig. 1b.

3.2 The Most Stable Geometry

As already mentioned before at the introduction hydrogen acts as amphoretic impurity in semiconductor, i.e. it can have positive or negative charge state. So, we examine the consequences of this amphoretic behavior of hydrogen in GaN. First we determine the most stable geometry by calculating the total energies for neutral and charge states of hydrogen in GaN. The hydrogen atoms were placed in various possible position (see Fig. 1b), then perform the self-consistent field (SCF) calculation based on density functional theory (DFT) with allowing the atoms to relax. The resulting total energies for H^+, H^0 and H^- are shown in Fig. 3.

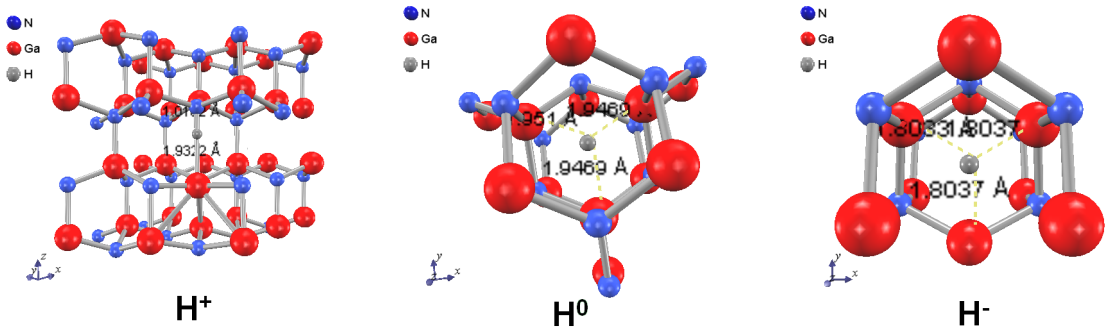

(a) (b) (c)

Figure 3: Configuration of the most stable geometry for hydrogen in wurtzite GaN obtained from first-principles calculation. (a)The H^+ stable at the bond center, (b) The H^0 stable at triagonal channel, and (c) The H^- also stable at triagonal channel center of wurtzite

Our results are in general consistent with those of past studies [9] [10]. Here we clarify some details of the optimized geometries. GaN is partly ionic in nature, this properties has significant influence on stable position for charge states of H. We found that the bond-center parallel to c axis ($BC_{\parallel}$) is the most stable geometry for positive charge of hydrogen (H^+) (see Fig. 3a), with

the calculated N-H bond length for this position is 1.02$\mathring{A}$ and Ga-H bond length is 1.93$\mathring{A}$. For the negative charge of hydrogen (H^-), the most stable geometry is at the center of triagonal channel (see Fig. 3c). At this geometry the hydrogen atoms has three nearest gallium atoms. Those stable geometry results for positive (H^+) and negative charged (H^-)of hydrogen in GaN are in good agreement with previous theory calculation [9] [10] and the experiment that investigate muonium (Mu) defect in GaN [12] [13]. Mu is similar or as a pseudo-isotope of hydrogen which has a very light mass ($m_\mu \simeq \frac{1}{9}\ m_p$). Those similarity and the very light mass of Mu implies to the bigger of quantum effects of Mu to give more accurate results. The neutral hydrogen (H^+) in GaN also found stable at the center of the trigonal channel (see Fig. 3b), where the hydrogen atoms has three nearest gallium atoms. The Ga-H bond length for this geometry almost same with the Ga-N bond length, about 1.95Å. The μSR experiment provides important information on the geometry [11]. We find that all the optimized geometries have trigonal symmetry, which is consistent with results of μSR ([12–14])

3.3 The Stability of Charge Hydrogen

After determining the most stable geometry of neutral and charge states of hydrogen in GaN, now we investigate which is the most stable states of hydrogen. As shown in Fig 4, the band dispersion of the impurity level is small enough to determine the energetical position of the impurity level. In order determine the stability of the system with charged states compared to the neutral one, we examine several steps as follows. In case for negative charge states, first we determine the most stable geometry structure of neutral charge state, and we have done this in the sub section 3.2. After that we calculate the total energy of the -1 charge state for the geometry optimized in the case of the neutral charge state, $E_{tot}(0)$. second step, we optimize the geometry for the -1 charge state and get the total energy, $E_{tot}(-1)$. The difference between the energies of $E_{tot}(0)$ and $E_{tot}(-1)$ is called the relaxed energy ΔE_{relax} which is negative.

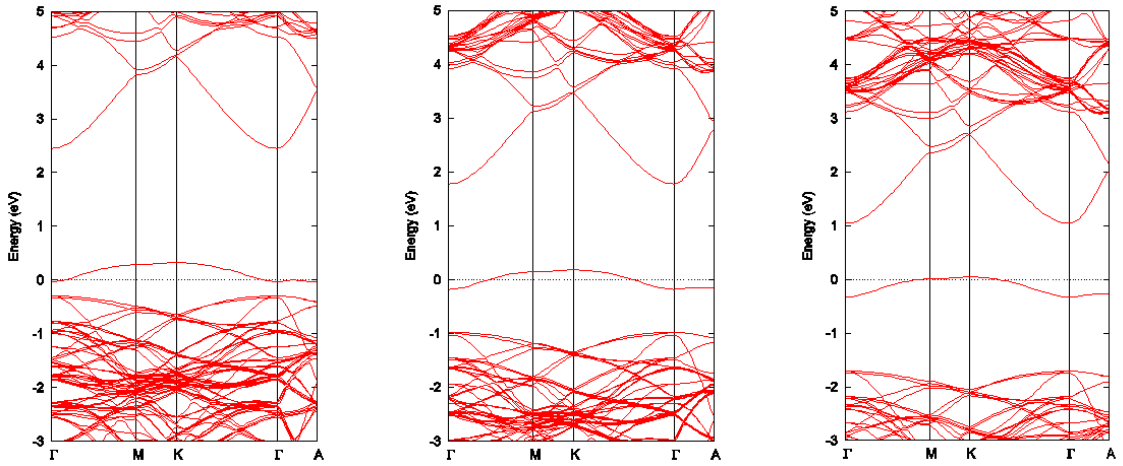

(a) (b) (c)

Figure 4: The calculated band structure of GaN with hydrogen atom in three different charged states, to measure the ΔE_{relax} (a) positive half charged, (b) neutral, and (c) negative half charged.

According to the Slater's argument [15] [16] that explain if we have two systems with the same

atomic geometry and have charged states 0 and -1, then the difference in total energy between them is given as the highest occupied level energy of a system having half-negative charge with the same atomic geometry. So in the third step, we carry out calculation of the electronic structure levels for the negative half charge state and the geometry optimized for the neutral charge state, then we calculate the difference between the energies of the impurity level and the valence band maximum, is called the level energy ΔE_{level} which is negative. We can get this value from electronic band structure as seen on Fig. 4. The energy of the ΔE_{relax} and ΔE_{level} for the positive charge state can be computed in the same manner as well as negative charge.

The relative total energy of the charged states q hydrogen for the fermi energy μ is given by :

$$^{rel}E_{total}(q) = \Delta E_{relax}(q) + \Delta E_{level}(q) + \mu.q \tag{1}$$

As we can see at Fig. 5, it shows the relative total energy of hydrogen impurity in its various charge state in GaN. The Fermi level (E_F) is set to zero at the top of valence band of GaN and (E_F) changes within the calculated band-gap energy. The E_F moves through the band gap. In the beginning, the stable charge is the positive charge of hydrogen (for E_F below 1.7eV) and then changes directly to the negative one (for E_F above 1.7eV). This implies that p-type GaN, where E_F close to the valence band maximum, the positive charged H^+ is stable and H act as a donor. For the n-type GaN, where E_F close to the conduction band minimum, the negative charged H^- is favored and act as acceptor. The facts that the neutral states H^0 is never stable in this system, on the other words that the hydrogen thus effectively "self-compensates". With this results, we conclude that the hydrogen has a negative-U behavior in GaN, which is consistent with the results of past theoretical studies [9] [10].

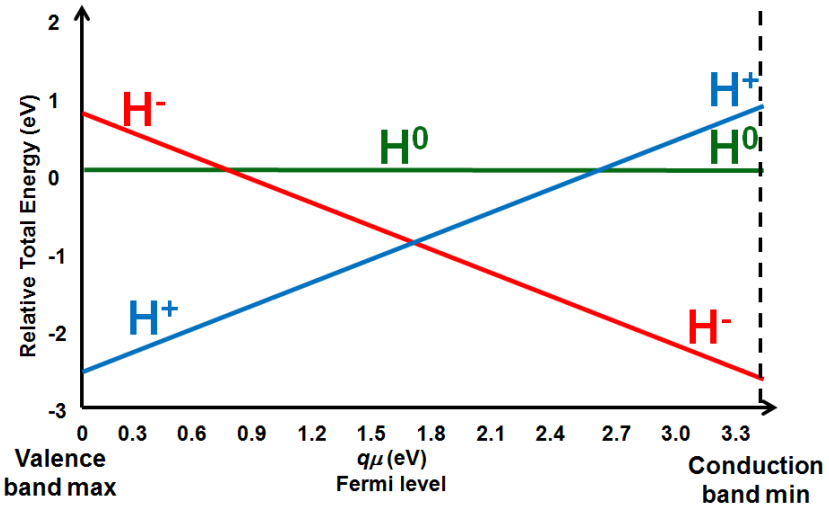

Figure 5: The relative total energies of the positively charged (H^+), neutral (H^0), and negatively charged (H^-) as a function of fermi level. When fermi level = 0, it is corresponds to the top of valence band.

4 Summary

First-principles calculations are carried out to investigate the behavior of hydrogen impurity in GaN. We find that the bond-center (BC) site is the most stable geometry for H^+ impurity whereas the trigonal channel at the center wurtzite with the hydrogen has three nearest Ga atoms is the most stable geometry for H^0 and H^-, which is consistent with results of past studies. We clarify some details of the geometries and find that our results are in good agreement with experimental results of muon. However, the calculation of the hyperfine coupling constants is necessary for further discussion in future. We clarify that the present supercell model well describes the impurity level and find that the hydrogen impurity has a negative-U property in GaN, which is consistent with the results of the past theoretical studies.

Acknowledgment

The numerical calculations were performed using the Supercomputers at Center-Institute for Solid State Physics (ISSP), and the Indonesian Institute of Science (LIPI) High Performance Computing. The first author thanks to Kanazawa University, Japan Student Services Organization (JASSO) and Indonesian Ministry of Research, Technology and High Education (KEMENRISTEKDIKTI) for financial support through the scholarship program.

References

[1] S. Nakamura, T. Mukai, and M. Senoh (1994). Candela-class high-brightness InGaN/AIGaN double-heterostructure (DH) blue-light-emitting diodes (LEDs). *Appl. Phys. Lett.*, **64**, 1687-1689.

[2] S. Nakamura, N. Iwasa, M. Senoh, and T. Mukai (1992). Hole Compensation Mechanism of P-Type GaN Films *J.Appl. Phys.*, **31**, 1258-1266.

[3] Jorg Neugebauer and Chris G. Van de Walle (1995). Hydrogen in GaN: Novel Aspects of a Common Impurity *Phys. Rev. Lett.*, **75**, 4452-4455.

[4] Chris G. Van de Walle and Jorg Neugebauer (2006). Hydrogen in Semiconductor *Annu. Rev. Mater. Res.*, **36**, 179-198.

[5] Chris G. Van de Walle and Jorg Neugebauer (2004). First-principles calculations for defects and impurities: Applications to III-nitrides *J. App. Phys.*, **95**, 3851-3879.

[6] C. Stampfl and C. G. Van de Walle (1999). Density-functional calculations for III-V nitrides using the local-density approximation and the generalized gradient approximationt Phys. Rev. B., **59**, 5521-5535.

[7] Properties of Group III Nitrides, Editor: J.H. Edgar, Electronic Materials Information Service (EMIS) Datareviews Series (Institution of Electrical Engineers, London, 1994

[8] A. Trampert, O. Brandt and K.H. ploog (1990). in Crystal Structure of Group III Nitrides, Editor:J.I. Pankove and T.D. Moustakas, Semiconductors and Semimetals Vol. 50 (Academic), San Diego, 1998

[9] A. F. Wright (1999). Influence of crystal structure on the lattice sites and formation energies of hydrogen in wurtzite and zinc-blende GaN Phys. Rev. B., **60**, R5101-R5104

[10] S. M. Myers, A. F. Wright, G. A. Petersen, C. H. Seager, W. R. Wampler, M. H. Crawford, and J. Han (2000). Equilibrium state of hydrogen in gallium nitride: Theory and experiment *J.Appl. Phys.*, **88**, 4676-4687.

[11] S.K.Estrecher and M. Sanati (2006), D, H, and Mu in GaN: Theoretical predic-tions at finite temperatures Physica B., **374-375**, 363-367.

[12] R.L. Lichti, S.F.J. Cox, M.R. Dawdy, T.L. Head, B. Hitti, R.J. Molnar, C. Schwab, R.P. Vaudo (2000). Sites and motion of Mu^- defect centers in n-type gallium nitride Physica B., **289–290**, 542-545.

[13] R.L. Lichti, S.F.J. Cox, E.A. Davis, B. Hittie, S.K.L. Sjuea (2000). Positively charged muonium centers in aluminum and gallium nitrides Physica B., **308-310**, 73-76.

[14] K. Shimomura, R. Kadono, K. Ohishi, M. Mizuta, M. Saito, K. H. Chow, B. Hitti, and R. L. Lichti(2004). Muonium as a Shallow Center in GaN Phys. Rev. Lett., **92** 135505 (1-4).

[15] J. C. Slater (1974). *The Self Consistent Field for Molecules and Solids.* McGraw-Hill, New York.

[16] Ayumi Yokozawa (1997). First-principles calculations for charged states of hydrogen atoms in SiO_2 Phys. Rev. B., **55**, 13783-13788.

Multiferroic $BiFeO_3$ for Photovoltaic Applications : A First-principles Study

Muhammad Rifqi Al Fauzan[a,b], Fumiyuki Ishii[a], and Mineo Saito[a],

[a]Graduate School of Natural Science and Technology, Kanazawa University, Japan, E-mail: alfauzan@cphys.s.kanazawa-u.ac.jp, ishii@cphys.s.kanazawa-u.ac.jp, m-saito@cphys.s.kanazawa-u.ac.jp

[b]Faculty of Mathematics and Natural Science, Institut Teknologi Bandung, Indonesia, E-mail: alfauzan@s.itb.ac.id

Abstract. *Ferroelectric materials are new candidates for photovoltaic materials. Ferroelectrics can produce photocurrents without using p-n junction which is necessary for conventional photovoltaic devices. BiFeO3 is one of the most promising multiferroic materials having band gap of 2.5 eV. This band gap is too wide to be used as photovoltaic devices, therefore lower band gap is necessary. In order to reduce $BiFeO_3$ band gap, we carry out a first-principles calculation. We study Cu substitution impurities. We introduce a single Cu atom in the 2x2x2 supercell and we find that the band gap is reduced by 0.039 eV. We expect the existence of optical transition energy between valence and impurity band with energy value 1.232 eV lower than the band gap of $BiFeO_3$.*

Keywords: $BiFeO_3$, Cu substitution impurities, photovoltaics, band gap.

1 Introduction

Bismuth ferrite ($BiFeO_3$) is a promising room temperature single-phase multiferroic material [1]. It has ability to exhibit both ferromagnetic (G-type antiferromagnetic) under the Neel temperature (T_N) of 640 K and ferroelectric properties under the Curie temperature (T_C) of 1120 K [2, 3]. Those two orders are coupled so that by changing the magnitude or direction of one type of order, the other is also changed [4]. At ambient condition, BiFeO3 has a rhombohedral symmetry belonging to the R3c space group [7]. It permits the development of spontaneous polarization along [111] direction of the highly distorted perovskite [8]. The primitive unit cell contains two formula units with ten atoms [9] as shown in Fig. 1. The perovskite structure has the general stoichiometry ABX_3 [10]. Where "A" is large cation, "B" is smaller cation, and "X" is anion. In BiFeO3 case, both A and B cations are trivalent states.

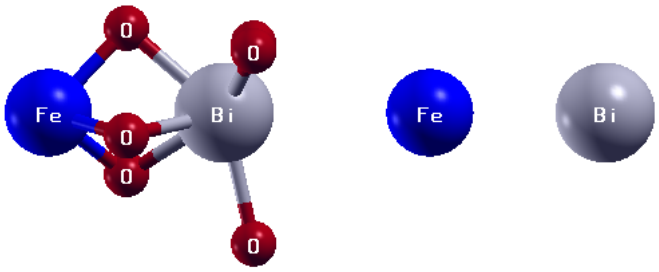

Figure 1: Schematic view of $BiFeO_3$ unit cells.

Recently the photovoltaic effect in ferroelectric materials has attracted enormous interest. Ferroelectrics can generate photocurrents without using p-n junction which is necessary for conventional photovoltaic devices. Ferroelectrics do not need separation of electrons and holes by internal field et all, photocurrent and photovoltage can be observed in pure homogeneous single crystals [5, 6]. This ability leads ferroelectrics as one of the candidates for next generation photovoltaic devices. Experimentally multiferroic $BiFeO_3$ materials having band gap of 2.5 eV as reported by Gao et al.[12]. Unfortunately, these band gap is too large to be used for photovoltaic application. Material with band gap 1.3–2.0 eV have the greatest potential to make an efficient cell [13]. A wider band gap would be unable to absorb low-energy photons and a narrower band gap would be lose many high-energy photon to heat. This band gap problem become our concern in this study.

2 Calculation Details

To perform the first-principles electronic-structure calculations we use density functional theory (DFT) as implemented in OpenMX code [14]. All calculations in this study performed by local spin density approximation (LSDA) exchange correlation form [15] plus U [16] approach with U=4 eV for Fe and Cu 3d electrons, norm-conserving pseudopotentials [17] are used. Wavefunctions are expanded by linear combination of multiple pseudoatomic orbitals (LCPAO) [18, 19]. The orbitals are specified as Bi10.0-s3p3d2, Fe8.0S-s3p3d3, Cu8.0S-s3p3d3, and O6.0-s3p3. The former numbers written after atomic symbols are cut off radii of the confinement potential. Whereas the latter parts (s3p3d2, etc) are number of orbitals for s, p, and d composed. These calculations are performed with a $8 \times 8 \times 8$ uniform $\mathbf{k}$-point mesh centered at Γ and the convergence criteria for energy is 10^{-7} Hartree. G-type antiferromagnetic order is assumed for all calculations with collinear spin arrangement (does not consider spin orbit coupling).

3 Results and Discussion

3.1 Structural parameters

BiFeO3 has rhombohedral structure with space group R3c, where the Bi atom is placed at the origin. The calculation results of full structural optimization of G-type antiferromagnetic BiFeO3 are collected in Table 1. Our results are in better agreement with both experimental [20] and previous calculations [21]. Fractional coordinates of atomic positions presented in Wyckoff positions, 2a for Bi and Fe and 6b for O are referred to the rhombohedral system. The lattice constant of the primitive unit cell a_{rh} and the rhombohedral angle α are also listed. Both calculated and experimental rhombohedral angle are very close to 60° which would appropriate to perfect cubic lattice vectors.

Tabel 1. Calculated and experimental parameters for $BiFeO_3$ in R3c structure.

		Present calc.	Prev. calc.	Expt.
Bi ($2a$)	x	0	0	0
Fe ($2a$)	x	0.214	0.227	0.221
O ($6b$)	x	0.536	0.542	0.538
	y	0.938	0.943	0.933
	z	0.392	0.397	0.395
a_{rh}(Å)		5.59	5.52	5.63
α(°)		59.37	59.84	59.35

In the R3c structure, the Fe site has two types of bonds with different bond length. Three oxygen neighbors have bond lengths of 1.94 Å and the others have 2.11 Å, which results in the distortion of FeO_6 octahedra. The ideal cubic perovskite structure has O-Fe-O bond angle of 180°, which is changed in this system by 165.07° because of its distortion.

3.2 Electronic properties

We calculate the electronic structures of $BiFeO_3$ in R3c structure. For $BiFeO_3$ unit cell, the structure has indirect band gap of 1.77 eV. We did a comparison with previous calculation performed by Neaton et al.[21] as listed in Table 2.

Tabel 2. $BiFeO_3$ unit cell band gap of present and previous calculations (in eV).

	U=4 eV
Present Calc.	1.8
Previous Calc.	1.9

In order to reduce $BiFeO_3$ band gap, we introduce Cu substitution impurities with concentration about 6.25%. So that we need to enlarge $BiFeO_3$ system from unit cell to $2 \times 2 \times 2$ supercell. The supercell system consists of 80 atoms: 16 Bi, 16 Fe, and 48 O atoms, where a Fe atom is replaced with a Cu atom as an impurity as shown in Fig. 2. After adding Cu impurities, then we relax the position of all atoms until the absolute deviation between the eigenvalue energy at the current and previous SCF step is less than convergence criterion.

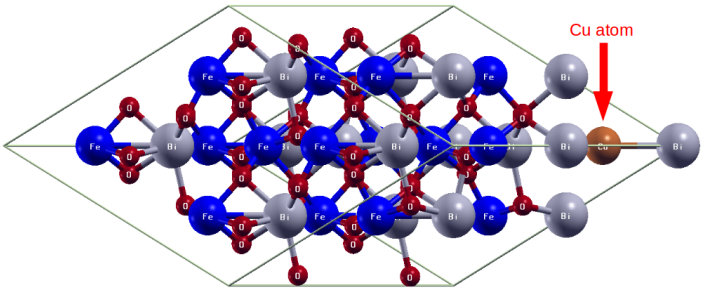

Figure 2: A $2 \times 2 \times 2$ $BiFeO_3$ supercell with Cu substitution impurities. Grey ball is Bi, blue ball is Fe, red ball is O, and brown ball is Cu.

The calculated energy band structure of $BiFeO_3$ supercell along high-symmetry directions in Brillouin zone for system without impurities (called perfect system) and system with Cu impurities (called impurity system) are given in Figs. 3(a) and 3(b). Red and green structures for the up- and down-spin states, respectively. Up- and down-spin states in perfect system have exactly same value, therefore this system has no net magnetic value. Both perfect and impurity systems have indirect band gap, with the top of the valence band located at F point and the bottom of the conduction band at γ point.

For perfect system, we can find energy band gap E_g about 1.834 eV. Some states appear between valence and conduction band for impurity system case. This states come from Cu impurities (called impurity band). So, in order to perform band gap calculation we have to neglect this states. Then we can find impurity system has band gap E_g^{Cu} about 1.795 eV, only 0.039 eV reduced from perfect system band gap. This band gap is still too wide for photovoltaic applications. We

expect the existence of optical transition energy E_{Opt}^{Cu} between valence and impurity band. This optical transition energy has value about 0.602 eV, 1.232 eV different with the band gap of perfect system. Unfortunately this optical transition energy value also still not favorable for photovoltaic applications. In addition, the calculated Fe magnetic moment is 3.67 μB, in a good agreement with experimental value [20] (3.75 μB) and theoretical value [22] (3.65 μB).

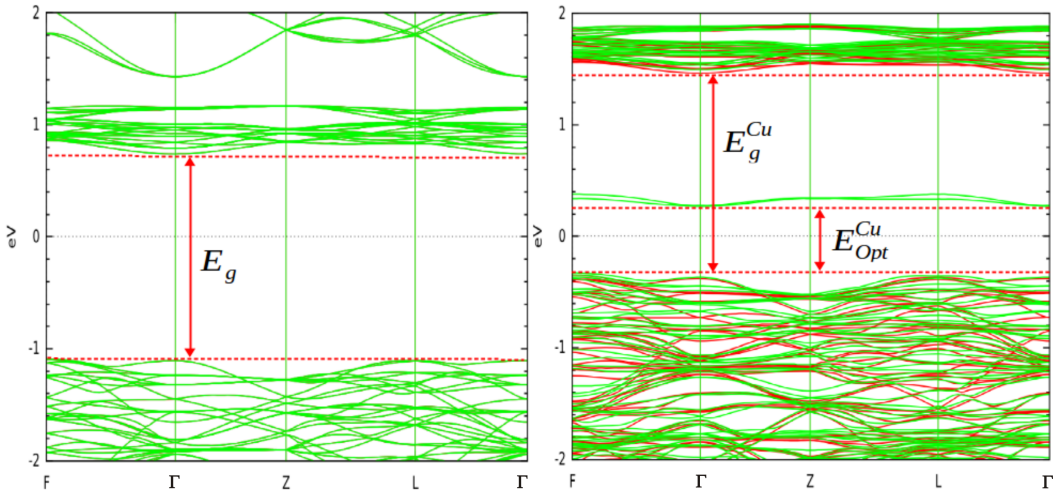

(a) (b)

Figure 3: Band structures of $BiFeO_3$ supercell along high-symmetry directions, the Fermi level is located at 0 eV. The valence, conduction, and impurity band edges are indicated by the red dashed horizontal lines. (a) $BiFeO_3$ supercell system without impurities, (b) $BiFeO_3$ supercell system with Cu impurities.

4 Conclusion

In summary, we have investigated the effect of Cu substitution impurities in $BiFeO_3$ system. We find that Cu impurities reduce $BiFeO_3$ band gap by 0.039 eV. We expect there is optical transition energy between valence and impurity band, which has value 1.232 eV lower than the band gap of $BiFeO_3$ perfect system.

Acknowledgment

This study was supported by Japan student service organization (JASSO). The calculations were performed using the supercomputer at the Institute for Solid State Physics (ISSP), the University of Tokyo.

References

[1] J. Wang, J.B. Neaton, H. Zeng, et al. (2003). Epitaxial $BiFeO_3$ multiferroic thin film heterostructures. *Science*, **299**, 1719 – 1722.

[2] G. Catalan and J.F. Scott (2009). Physics and applications of bismuth ferrite. *Advanced Materials*, **21**, 2463 – 2485.

[3] Y. Wang, J.E. Saal, P. Wu, et al. (2011). First-principles lattice dynamics and heat capacity of $BiFeO_3$. *Acta Materialia*, **59**, 4229 – 4234.

[4] N.A. Spaldin and M. Fiebig (2005). The renaissance of magnetoelectric multiferroics. *Science*, **309**, 391 – 392.

[5] V.M. Fridkin (2001). Bulk Photovoltaic effect in noncentersymmetric crystals. *Crystallography Reports*, **46**, 654 – 658.

[6] A.M. Glass, D.V.D. Linde, and T.J. Negran (1974). High-voltage bulk photovoltaic effect and the photorefractive process in $LiNbO_3$. *App. Phys. Lett.*, **25**, 233 – 234.

[7] J. Lu, F. Schrettle, F. Mayr, et al. (2010). On the room temperature multiferroic $BiFeO_3$: magnetic, dielectric and thermal properties. *Eur. Phys. J. B.*, **75**, 451-460.

[8] K.Y. Yun, D. Ricinshi, T. Kanashima, et al. (2004). Giant ferroelectric polarization beyond 150 C/cm^2 in $BiFeO_3$ thin film. *Jap. Jour. of App. Phys. Lett.*, **43**, 647 – 648.

[9] C. Michel, J.M. Moreau, D. Gary, et al. (1969). The atomic structure of $BiFeO_3$. *Solid State Commn.*, **7**, 701 – 704.

[10] F.S. Galasso (1969). *Structure, properties and preparation of perovskite-type compounds*. Pergamon Press, London.

[11] H. Shima, H. Naganuma, and S. Okamura (2013). Optical properties of multiferroic $BiFeO_3$ films. *Material Science - Advanced Topics*, 33 – 61.

[12] F. Gao, Y. Yuan, K.F. Wang, et al. (2006). Preparation and photoabsorption characterization of $BiFeO_3$ nanowires. *App. Phys. Lett.*, **89**, 102506-1 – 102506-3.

[13] S.S. Sun and N.S. Sariciftci (2005). *Organic photovoltaics: mechanisms, materials, and devices*. CRC Press, Florida.

[14] T. Ozaki, H. Kino, J. Yu, et al. (2013). OpenMX open source package for material explorer ver. 3.7., http://openmx-square.org/.

[15] D.M. Ceperley and B.J. Alder (1980). Ground state of the electron gas by a stochastic method. *Phys. Rev. Lett.*, **45**, 566 – 569.

[16] M.J. Han, T. Ozaki, and J. Yu (2006). O(N) LDA+U electronic structure calculation method based on the nonorthogonal pseudoatomic orbital basis. *Phys. Rev. B*, **73**, 045110-1 – 045110-11.

[17] N. Troullier and J.L. Martins (1991).Efficient pseudopotentials for plane-wave calculations. *Phys. Rev. B*, **43**, 1993 – 2006.

[18] T. Ozaki (2003). Variationally optimized atomic orbitals for large-scale electronic structures. *Phys. Rev. B*, **67**, 155108-1 –155108-2.

[19] T. Ozaki and H. Kino (2004). Numerical atomic basis orbitals from H to Kr. *Phys. Rev. B*, **69**, 195113-1 – 195113-19.

[20] F. Kubel and H. Schmid (1990). Structure of a ferroelectric and ferroelastic monodomain crystal of the perovskite $BiFeO_3$. *Acta Cryst.*, **B46**, 698 – 702.

[21] J.B. Neaton, C. Ederer, U.V. Waghmare, et al. (2005). First-principles study of spontaneous polarization in multiferroic $BiFeO_3$. *Phys. Rev. B*, **71**, 014113-1 – 014113-8.

[22] P. Hermet, M. Goffinet, J. Kreisel, et al. (2007). Raman and infra red spectra of multiferroic bismuth ferrite from first principles. *Phys. Rev. B*, **75**, 220102-1 – 220102-4.

Prediction of Solvation Free Energy of Proteins: Molecular Dynamics Simulation and QSPR Model Approach

Sri R. Natasia[a,b], Hiroaki Saito[a], Taku Mizukami[c], Kazutomo Kawaguchi[a], Hidemi Nagao[a]

[a]Institute of Science and Engineering, Kanazawa University, Kakuma, Kanazawa 920-1192 Japan,
[b]Faculty of Mathematics and Natural Sciences, Institut Teknologi Bandung, Jl. Ganesha 10, Bandung 40132 Indonesia,
[c]School of Material Science, Japan Advanced Institute of Science and Technology, Nomi, Ishikawa 923-1292 Japan,
E-mail: ayu@wriron1.s.kanazawa-u.ac.jp, saito@wriron1.s.kanazawa-u.ac.jp

Abstract. *Solvation free energy has valuable role as represents the desolvation cost of a molecular binding interaction, which is very important in a variety of chemical and biological processes. Therefore, many computational methods have been explored to predict this value. In this study, we attempted to find the correlation between experimental and calculated value of solvation free energy of proteins, containing organic molecules, by using quantitative structure property relationship (QSPR) model. To obtained a comparable value of solvation free energy which will be used as reference in QSPR model, we adopted energy representation (ER) method. And as this method works through molecular dynamic (MD) simulation, we then performed the MD simulation prior to the calculation by ER method. The results showed that the predicted solvation free energies were quite close to calculated values by ER method. We also found that the values of solvation free energy, both in MD simulation and ER method, were well correlated to solvent accessible surface area of hydrophobic portion.*

Keywords: solvation free energy, organic molecules, proteins, molecular dynamics, ER method, QSPR model

1 Introduction

Solvation free energy is one of the most important physical quantity to describe thermal system of a solution. It has valuable role as represents the desolvation cost of a molecular binding interaction [1], which is very important in a variety of chemical and biological processes. For instances, in drug discovery and in analysis of protein folding and binding. Therefore, many computational methods have been explored to predict this value.

In recent years, quantitative structure-property relationship (QSPR) model has been widely used in chemical physics area to predict some physical quantities of organic materials. QSPR model is well known for its simplicity yet has the ability to provide a promising result. This approach attempts to relate the structure-derived property of a chemicals to its biological or physicochemical activity. One of the most fundamental and common modeling method in QSPR is multiple linear regression, which is favored for its simplicity and ease of interpretation [2].

In construction QSPR model of protein, a reliable data of solvation free energy is strongly needed. However, due to limitation in experimental measurements, solvation free energy of protein is still rare even unavailable. Hence, to provide such value, we adopted energy representation [3] (ER) method which has been successfully applied for many biological systems [4].

Here, firstly we employ ER method to calculate solvation free energy of 50 organic molecules containing diverse organic functions in explicit water solvent. As the calculation using this method is obtained in combination with molecular dynamics (MD) simulation [5], we carry out the MD simulation of each molecule prior to the calculation of this value. In order to confirm the validity of this method, we then compare the results to experimental data. Further, we compute solvation free energy of proteins and construct the QSPR model with utilizing MD simulation.

2 Materials

We calculated solvation free energies of 50 organic molecules containing diverse organic functions; alkanes, alkenes, aromatics, alcohols, aldehydes, ketones, amines, ethers, esters, and others. The number of atoms is vary from 5 to 40. We retrieved the coordinate files of these molecules in mol2 format from reference [6]. The 50 organic molecules are listed in Table 1 below.

Table 1: The 50 organic molecules, number of atom and experimental value of ΔG_{sol}

Name	**Atom**	ΔG_{sol} **exp. (kcal/mol)**
Alkanes		
ethane	8	1.83
2,2-dimethylbutane	20	2.51
2,3,4-trimethylpentane	26	256
chlorofluoromethane	5	-0.77
1,1,1,2-tetrachloroethane	8	-1.43
Alkenes		
1,1-diphenylethene	26	-2.78
ethylene	6	1.28
1,1,2-trichloroethylene	6	-0.44
1-methylcyclohexene	19	0.67
butadiene	10	0.56
Aromatics		
1,3-dichlorobenzene	12	-0.98
toluene	15	-0.90
m-xylene	18	-0.83
9,10-dihydroanthracene	26	-3.78
1,4-dibromobenzene	12	-2.30
Alcohols		
phenol	13	-6.60

Table 1: The 50 organic molecules, number of atom and experimental value of ΔG_{sol} (continued)

Name	**Atom**	ΔG_{sol} **exp. (kcal/mol)**
methanol	6	-5.10
2-methoxyethanol	13	-6.62
p-cresol	16	-6.13
2,2,2-trifluoroethanol	9	-4.31
Ethers		
anisole	16	-2.45
1,4-dioxane	14	-5.06
diphenylether	23	-2.87
tetrahydrofuran	13	-3.47
2,5-dimethyltetrahydrofuran	19	-2.92
Aldehydes		
butanal	13	-3.18
2-hydroxybenzaldehyde	15	-4.68
2-methylpropanal	13	-2.86
4-(1-methylethenyl)-1-cyclohexene-1 -carboxaldehyde	25	-4.09
formaldehyde	4	-2.75
Ketones		
cyclopentanone	14	-4.70
acetone	10	-3.80
nitroxyacetone	13	-5.99
3,3-dimethyl-2-butanone	19	-3.11
cyclohexanone	17	-4.91
Esters		
methyl acetate	11	-3.13
ethyl hexanoate	26	-2.23
methyl-4-nitrobenzoate	20	-6.88
methyl pentanoate	20	-2.56
isopropyl formate	14	-2.02
Amines		
2-naphtylamine	20	-7.47
1-N,1-N-diethyl-2,6-dinitro-4-(trifluoromethyl)benzene-1,3-diamine	35	-5.66
2-methoxyethanamine	14	-6.55
(2-benzhydryloxyethyl)-dimethyl-amine	40	-9.34

Table 1: The 50 organic molecules, number of atom and experimental value of ΔG_{sol} (continued)

Name	**Atom**	ΔG_{sol} **exp. (kcal/mol)**
n-methylmethanamine	10	-4.29
Miscellaneous		
benzamide	16	-11.00
butane-1-thiol	15	-0.99
pyridine	11	-4.69
2-methylpirazine	13	-5.51
benzonitrile	13	-4.10

In construction of QSPR model of protein, we used 4 small and neutral charge proteins. These proteins were leginsulin, cysteine-rich module 3 from integrin beta-2 (the name is shortened as cysteine-rich in this paper), crambin, and ubiquitin. The initial structures were taken from X-ray diffraction and NMR solution from Protein Data Bank. The secondary structure of these proteins in ribbon representation using visual molecular dynamics (VMD) tools are shown in Figure 1. The protein data bank (PDB) ID, the number of residues and atoms are listed in Table 2.

3 Methods

3.1 MD Simulation

In MD simulations for organic molecule, the force field parameters and partial charge for each atom were assigned by *antechamber* [7] program of Amber tools in which general atom force field (GAFF) [8] and AM1-BCC [9, 10] were utilized. After generating Amber topology and coordinate files, these two files were converted to Gromacs topology and coordinate files using *acpype* [11] conversion script. These organic molecules were then solvated in a simulation box of 32Å × 32Å × 32Å which consists of 1000 water molecules using Gromacs utilities. The simulations were performed for 100 ps and sampled every 10 fs for solution system. Meanwhile, for pure solvent and isolated solute systems, the simulations were conducted for 10 ps and 10 ns and sampled every 200 fs.

Meanwhile, for protein system, we carried out MD simulations for 20-30 ns to obtain the equilibrium state of the system. The proteins were placed at the center of simulation box with the distance at least 12Å from the box edge. The box was then filled with water molecules to set the density of the system near to 1 g/cm^3. The protein simulations were performed with AMBER99SB [12] force field.

All MD simulations, for both organic molecules and proteins, were performed by Gromacs 4.6.5 program package. The conditions were generated through NPT ensemble at 300 K and 1 bar using Nose-Hoover thermostat and Parinello-Rahman barostat with time constant of 1 ps [13, 14]. The Lennard-Jones potential was applied for intermolecular interaction with cutoff length of 13.5 Å. To handle electrostatic interaction, particle-mesh Ewald (PME) [15] with interpolation order of 6 was used. TIP3P water model [16] were adopted for water molecules. And the simulations were run with time step for integration of 2 fs.

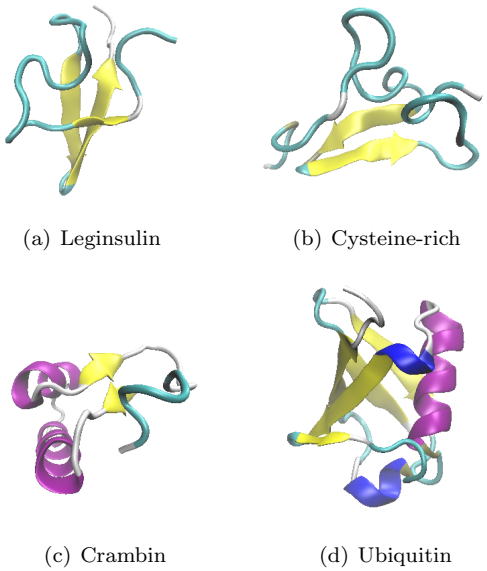

(a) Leginsulin (b) Cysteine-rich

(c) Crambin (d) Ubiquitin

Figure 1: Various initial structure of proteins were taken from the original PDB file

Table 2: The protein data bank ID, the number of residues and atoms of 4 proteins [17–20].

Protein	PDB ID	Residue	Atom
Leginsulin	1ju8	37	524
Cysteine-rich	1l3y	41	557
Crambin	1crn	46	642
Ubiquitin	1ubq	76	1231

3.2 Energy Representation

In energy representation (ER) method, solvation free energy can be represented as a functional of energy distribution functions $\rho^e(\varepsilon)$ and $\rho_0^e(\varepsilon)$ and the correlation matrix $\chi_0^e(\varepsilon, \eta)$ [4]. The energy distribution $\rho^e(\varepsilon)$ is given by

$$\rho^e(\varepsilon) = \langle \sum_i \delta(v(\psi, \mathbf{x_i}) - \varepsilon) \rangle \tag{1}$$

where ψ is the solute coordinate, $\mathbf{x_i}$ refers to the coordinate of the i-th solvent molecule, v is the potential function for the solute-solvent pair interaction, the summation is taken over all the solvent molecules, and $\langle ... \rangle$ is the ensemble average.
The calculation using ER method is obtained in combination with MD simulation. Therefore, to get the energy distribution functions and correlation matrix, we performed two kinds of MD simulation prior to the calculation of solvation free energy for each organic material. These simulations are solution system $\rho^e(\varepsilon)$ and the pure solvent system $\rho_0^e(\varepsilon)$. The solution system is the system in which the interaction presents between the solute and the solvent molecule under the solute-solvent pair interaction energy v of interest at full coupling. While the reference solvent system refers to the system in which no interaction physically present between the solute and the solvent molecule [4].

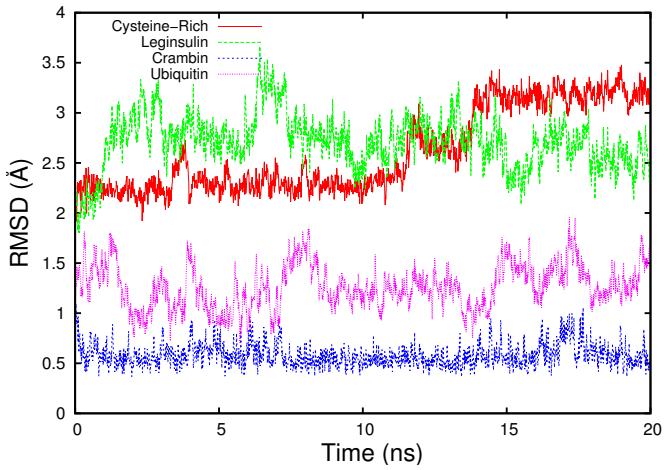

Figure 2: Root mean square displacement (RMSD) profiles of the four proteins

The energy distribution function $\rho_0^e(\varepsilon)$ and correlation matrix $\chi_0^e(\varepsilon,\eta)$ are constructed by placing the solute into the pure solvent as a test particle.
In MD simulation of solution system for protein, the protein conformations were taken from the stable state of the 20 ns equilibration MD. From the last 10 ns simulation, the structure of protein was sampled every 200 ps, leading to 50 samplings of protein structure. For each structure, the MD simulation was performed in which the protein was in fixed condition. The simulation were run for 1 ns and was kept every 10 fs, yielding 100 k sampling data for the calculation of $\rho^e(\varepsilon)$.
The next is the reference solvent system, which was used for the calculation of $\rho_0^e(\varepsilon)$ and $\chi_0^e(\varepsilon,\eta)$. The simulation was carried out for 1 ns and the snapshot was kept every 1 ps, leading to 1 k sampling data. The protein with random positions, yet same conformation as that in the solution system, were then inserted to the center of reference solvent system. The number of insertion sampling was 1000, hence we had 1000 k sampling data for the calculation of $\rho_0^e(\varepsilon)$ and $\chi_0^e(\varepsilon,\eta)$. The number of water molecule in both of simulation was equal to that in the prior equilibrium MD. These simulations were also conducted in NPT configuration.

3.3 QSPR Model

In construction of QSPR model, we adopted linear regression equation from Duffy and Jorgensen model [21]:

$$\Delta G_{sol} = \beta < \mathrm{E_{elec}} > + \alpha < \mathrm{E_{vdW}} > + \gamma < \mathrm{SASA} > + \epsilon \tag{2}$$

where $\mathrm{E_{elec}}$ is the electrostatic (Coulomb) energy between solute and solvent molecule. $\mathrm{E_{vdW}}$ represents the van der Waals (Lennard-Jones) interaction energy of solute-solvent. While SASA refers to solvent-accessible surface area of the solute by solvent molecule. The correlation coefficient β, α and γ are obtained from the covariance matrix among the MD simulation-derived descriptors and the reference solvation free energies, and is defined by:

$$cov(y, x_j) = \sum_{m=1}^{k} b_m . cov(x_m, x_j) \quad j, m = 1, ..., k \tag{3}$$

where y is the reference solvation free energy, x the MD simulation-derived descriptors, k the number of descriptors, and b_m refers to correlation coefficient of each descriptor (β, α and γ). The covariance matrix is governed by the following equation:

$$cov(x, y) = \frac{\sum_{i=1}^{n}(x_i - \bar{x})(y_i - \bar{y})}{(n-1)} \tag{4}$$

where x and y are the observed variables, can be the reference solvation free energy–descriptor or descriptor–descriptor. The index of i refers to the i-th data, while the bar signs refer to mean value of each observed variable. Then, the remaining ϵ becomes

$$\epsilon = \bar{Y} - \sum_{m=1} b_m \bar{x}_m \tag{5}$$

where $\bar{Y}$ is the mean value of the reference solvation free energy.
We also modified the equation 2 to asses the contribution of hydrophobic and hydrophilic properties of organic material. To do so, the SASA area was then divided into 2 parts, the areas of hydrophilic and hydrophobic portions of SASA ($\mathrm{SASA_{philic}}$ and $\mathrm{SASA_{phobic}}$). The modified of equation 2 is shown below:

$$\Delta G_{sol} = \beta < \mathrm{E_{elec}} > + \alpha < \mathrm{E_{vdW}} > + \gamma_1 < \mathrm{SASA_{phobic}} > + \gamma_2 < \mathrm{SASA_{philic}} > + \epsilon \tag{6}$$

The average values of all descriptors in equation (2) and (6) were calculated using *g_energy* and *g_sas* functions in Gromacs. The solvent probe radius of 1.4 Å was defined in calculation of SASA by *g_sas* function.

4 Results and Discussion

4.1 MD Simulation of Proteins

We calculated the root mean square displacement (RMSD) of backbone atoms of the four proteins to examine the stability of the systems during MD simulations. The RMSD curves are illustrated in Figure 2. These curves show that the three proteins reached the equilibrium state after about 10 ns simulation. Meanwhile, the RMSD profile of Cysteine-rich increased after 10 ns. Thus, to further see the dynamics of the system, the MD simulation was extended to 30 ns for this protein. Later,we found that it was fully equilibrated after about 15 ns simulation. The average of RMSD of all protein systems at stable state were 0.58-3.22 Å, indicating that overall dynamics structures were close to the native structures without large structural changes.

4.2 Solvation Free Energy by ER Method

The calculated solvation free energies of 50 organic molecules and the corresponding experimental data from reference [6] are shown in Figure 3.(a). We found that these values were in good agreement with the experimental data with the average of difference was about 2.09 kcal/mol.
We also investigated the solvation free energy with respect to the surface properties area of organic molecules. Figure 3 (b) displays the solvation free energy and the value of whole SASA. From this figure, we could tell that these two values do not correlate well for all organic molecules. Hence, we further analyzed the surface area into $\mathrm{SASA_{phobic}}$ and $\mathrm{SASA_{philic}}$ as shown in Figure 3 (c) and (d). Based on these figures, $\mathrm{SASA_{phobic}}$ has positive correlation towards the solvation free energy,

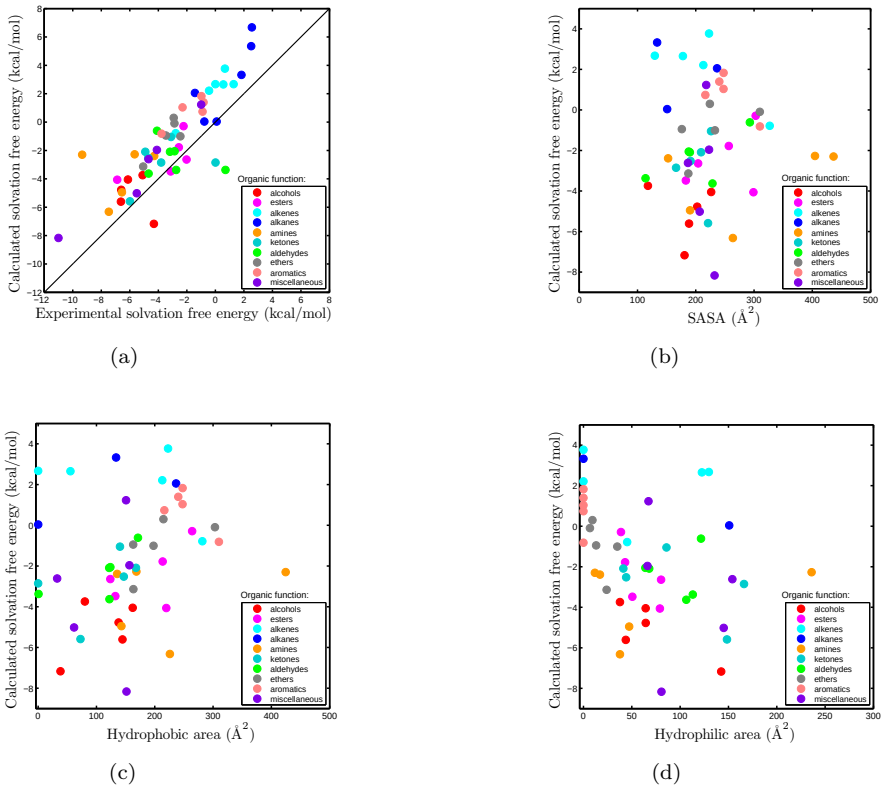

Figure 3: The experimental vs calculated values of solvation free energy of organic molecules by ER method (a) and the surface properties area of the molecules (b), (c), (d)

denoted by the correlation coefficient r of 0.29. Whereas $\text{SASA}_{\text{philic}}$ shows weak correlation in which $r = 0.11$. It means $\text{SASA}_{\text{phobic}}$ has more contribution to the solvation free energy of organic molecules. In addition, we observed that almost all of the used molecules consisting of more hydrophobic than hydrophilic atom. And these figures also indicated that more hydrophobic areas of the molecules can be accessed by water solvent than the hydrophilic does.

On the other hand, for the calculation of solvation free energies of proteins, the results are shown in Figure 4 (a) as the protein size (see Table 3 for the actual values). According to these results, the solvation free energies vary depend on the number of atom on the system. Also, the current results of solvation free energies are negative, showing that the proteins can stably exist in pure water solvent. The examined surface properties of the four proteins are illustrated in Figure 4 (b) (the calculated values are listed in Table 3). This figure shows the larger the protein, the possibility of the solvent molecules to access the area is also increase. Especially, globular protein like ubiquitin which has many hydrophilic residues on the surfaces in contact with water, leading to the high value of $\text{SASA}_{\text{philic}}$. In contrast, despite crambin also a globular protein, it is more known as "inside out" globular protein in which containing more hydrophobic residues [22]. Therefore, this protein is insoluble in water solvent indicated by the low value of SASA_{philic} and the solvation free energy.

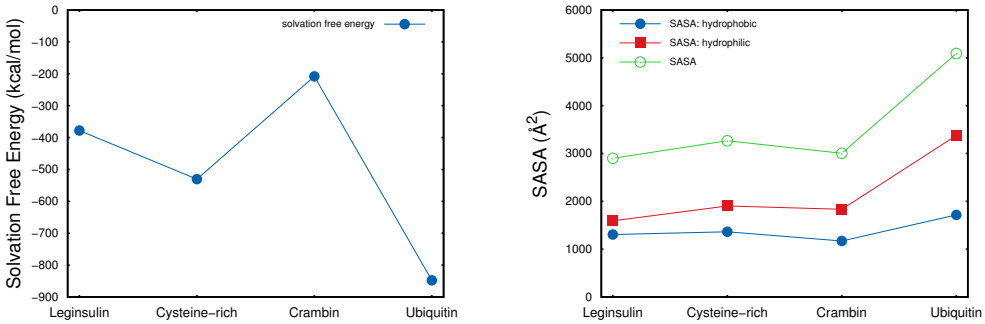

Figure 4: (a) Solvation free energies of the four proteins; and (b) The average of solvent accessible surface areas (SASA) of the four proteins; the green line: whole SASA, the red line: the SASA of hydrophilic portion ($SASA_{philic}$), the blue line: the SASA of hydrophobic portion ($SASA_{phobic}$).

Table 3: Solvation free energies by ER method, the whole portion of solvent accessible surface area (SASA), the SASA of hydrophilic portion ($SASA_{philic}$), and the SASA of hydrophobic portion ($SASA_{phobic}$) of the four proteins.

Protein	Solvation free energy (kcal/mol)	SASA (Å^2)	$SASA_{philic}$ (Å^2)	$SASA_{phobic}$ (Å^2)
Leginsulin	-378	2234	1190	1044
Cysteine-rich	-528	2336	1164	1172
Crambin	-208	2562	1137	1425
Ubiquitin	-848	4210	2188	2022

4.3 Solvation Free Energy by QSPR Model

After performing the MD simulations and the solvation free energy calculation, we constructed the QSPR model using the MD simulation-derived descriptors from all organic molecules and proteins. Based on the equations 2 and 6, we got the following model: -

$$\Delta G_{sol} = 0.1616 < \mathrm{E_{elec}} > +0.3567 < \mathrm{E_{vdW}} > +0.1968 < \mathrm{SASA} > -24.2945 \tag{7}$$

$$\begin{aligned}\Delta G_{sol} =& 0.1131 < \mathrm{E_{elec}} > +0.0085 < \mathrm{E_{vdW}} > +0.0679 < \mathrm{SASA_{phobic}} > \\ &+ 0.0003 < \mathrm{SASA_{philic}} > -9.5278\end{aligned} \tag{8}$$

which gave the squared correlation coefficient (R^2) = 0.998 and mean square error (MSE) = 35.802, for the equation 7. Meanwhile, for the model which constructed by equation 8, the R^2=0.994 and MSE = 144.477. These results indicated that our model which governed by equation 8 was quite good compare to Duffy and Jorgensen model. Moreover, the high values of R^2 in both of models suggest that the regression lines were well fitted to approximate the values of solvation free energy. The predicted solvation free energies of organic molecules and four proteins are shown in Figure 5 (a),(c) and (b),(d), for the equation 7 and 8, respectively.

We also calculated the averages of difference of these two models toward the calculated value of solvation free energies of proteins and the experimetal data of organic molecules. For the proteins, these values were 7.88 and 34.61 kcal/mol, for the model by equation 7 and 8, respectively. And for the organic molecules, the averages of difference of these two models were 3.74 and 4.69 kcal/mol, respectively.
Additionally, in our model, we found that the $SASA_{phobic}$ has more significant contribution than the $SASA_{philic}$, refers to the value of coefficient correlation in the equation 8. This positive correlation has also been presented in previous result by ER method. Moreover, the weak correlation between $SASA_{philic}$ and the solvation free energy as described in previous section also been made clear by value of coefficient correlation in our model. These results was supported by the finding of more hydrophobic atoms than hydrophilic in almost all organic molecules and proteins.

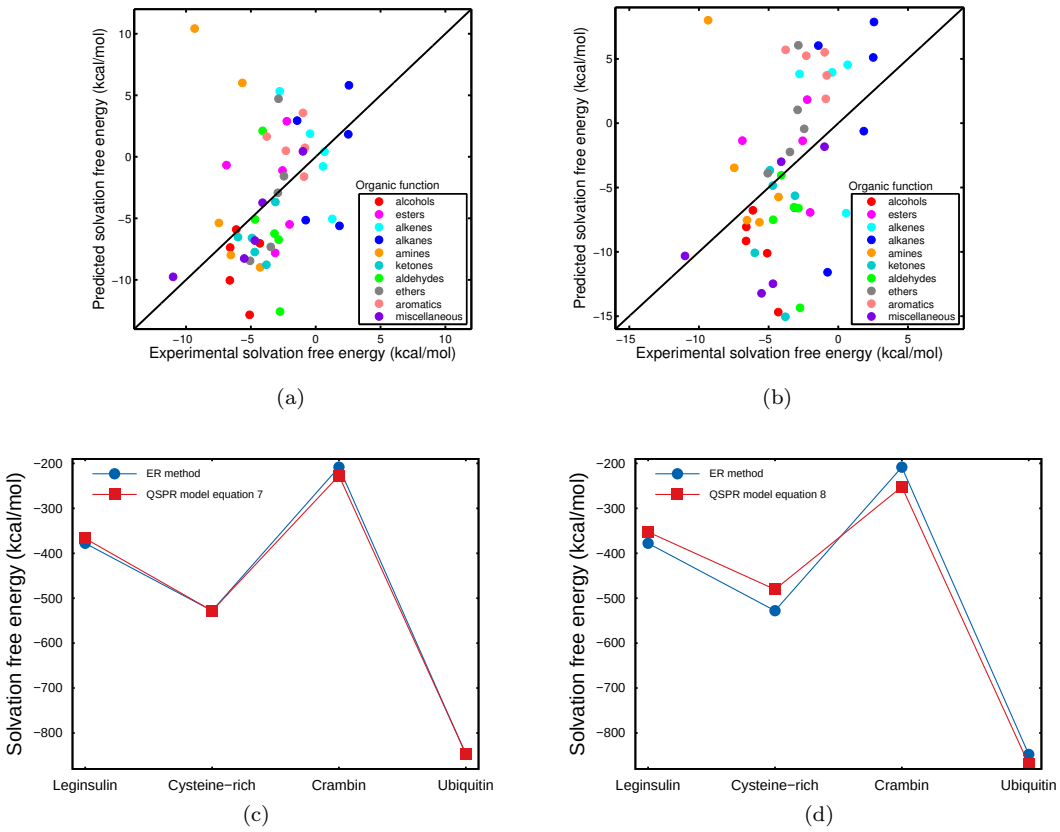

Figure 5: The QSPR model which governed by equation 7 (a),(c) and equation 8 (b),(d)

5 Conclusions

We carried out MD simulations of 4 small and neutral charge proteins, also 50 organic molecules containing diverse organic functions, to calculate solvation free energy of these organic materials. We also constructed the QSPR model, which utilizing MD simulation, to investigate the correlation

to the experimental data and to the calculated results of ER method. However, due to limitation of experimental data of proteins, the comparison of solvation free energy could not be done. Thus, we compared the results of our model to the calculated values by ER method. The comparison indicated that the predicted values of protein were quite close to the calculated values by ER method. We also found that the solvation free energies of our organic materials, both in MD simulation and QSPR model, were well correlated with $SASA_{phobic}$.

Acknowledgment

Some computations in this study were performed using computational resources at Research Center for Computational Science, Okazaki, Japan and Japan Advanced Institute of Science and Technology (JAIST). This works was (partially) supported by a Grant-in-Aid for Scientific Research on Innovation Areas "Chemical Biology of Natural Products" from The Ministry of Education, Culture, Sports, Science, and Technology, Japan.

References

[1] V. N. Viswanadgan, et. al (1999). Prediction of Solvation Free Energies of Small Organic Molecules: Additive-Constitutive Models Based on Molecular Fingerprints and Atomic Constants. *J. Chem. Inf. Comput. Sci.*, **39**, 405 – 412.

[2] M. Dehmer, et. al (2012). *Statistical Modelling of Molecular Descriptors in QSAR/QSPR.* Wiley – VCH, Weinheim.

[3] N. Matubayashi and M. Nakahara (2000). Theory of solutions in the energetic representation. I. Formulation. *J. Chem. Phys.*, **113**, 6070 – 6081.

[4] H.Saito, et. al. (2010). Hydration Property of Globular Proteins: an Analysis of Solvation Free Energy by Energy Representation Method. *Chem. Phys. Letters*, **497**, 218 – 222.

[5] Y. Karino, et. al. (2010). End-Point Calculation of Solvation Free Energy of Amino-Acid Analogs by Molecular Theories of Solution. *Chem. Phys. Letters*, **496**, 351 – 355.

[6] D. L. Mobley, et. al. (2009). Small Molecule Hydration Free Energies in Explicit Solvent: an Extensive Test of Fixed-Chrge Atomistic Simulations. *J. Phys. Chem. B*, **5(2)**, 350 – 358.

[7] J. Wang, et. al. (2006). Automatic Atom Type and Bond Type Perception in Molecular Mechanical Calculations. *J. Mol. Graph. Mod.*, **25**, 247 – 260.

[8] J. Wang, et. al. (2004). Development and Testing of a General AMBER Force Field. *J. Comp. Chem.*, **25**, 1157 – 1174.

[9] A. Jakalian, et. al. (2000). Fast, Efficient Generation of High-Quality Atomic Charges. AM1-BCC Model: I. Method. *J. Comp. Chem.*, **21(2)**, 132 – 146.

[10] A. Jakalian, et. al. (2002). Fast, Efficient Generation of High-Quality Atomic Charges. AM1-BCC Model: I. Parameterization and Validation.*J. Comp. Chem.*, **23(16)**, 1623 – 1641.

[11] A. W. Sousa da Silva and W. F. Vranken. (2012). ACPYPE - AnteChamber PYthon Parser interfacE. *BMC Research Notes*, **5**, 367.

[12] V. Hornak, et. al (2006). Comparison of Multiple Amber Force Fields and Development of Improved Protein Backbone Parameters. *Proteins*, **65**, 712 – 725.

[13] M. E. Tuckerman, et. al (2001). Non Hamiltonian Molecular Dynamics: Generalizing Hamiltonian Phase Space Principles to Non-Hamiltonian Systems. *J. Chem. Phys.*, **115(4)**, 1678 – 1702.

[14] M. Parrinello and A. Rahman. (1980). Crystal Structure and Pair Potentials: a Molecular Dynamics Study. *Phys. Rev. Lett.*, **45**, 1196.

[15] T. Darden, et. al. (1993). Particle Mesh Ewald-an N.Log(N) Method for Ewald Sums in Large System. *J. Chem. Phys.*, **98**, 10089 – 10092.

[16] W. L. Jorgensen, et. al. (1983). Comparison of Simple Potential Functions for Simulating Liquid Water. *J. Chem. Phys.*, **79(2)**, 926 – 935.

[17] T. Yamazaki, et. al. (2003). A Possible Physiological Function and the Tertiary Structure of a 4-kDa Peptide in Legumes. *Eur. J. Biochem.*, **270**, 1269 – 1276.

[18] N. Beglova, et. al. (2002). Cysteine-rich Module Structure Reveals a Fulcrum for Integrin Rearrangement Upon Activation. *Nat. Struct. Biol.*, **9**, 282 – 287.

[19] M. M. Teeter. (1984). Water Structure of a Hydrophobic Protein at Atomic Resolution: Pentagon Rings of Water Molecules in Crystals of Crambin. *Proc. Natl. Acad. Sci. Usa.*, **81**, 6014 – 6018.

[20] S. Vijay-Kumar. (1987). Structure of Ubiquitin Refined at 1.8 A Resoulution. *J. Mol. Biol.*, **194**, 531 – 544.

[21] E. M. Duffy and W. L. Jorgensen. (2000). Prediction of Properties from Simulations: Free Energies of Solvation in Hexadecane, Octanol, and Water. *J. Am. Chem. Soc.*, **122**, 2878 – 2888.

[22] B. L. Pentelute. (2008). *New Chemical Methods for the Synthesis of Proteins and Their Application to the Elucidation of Protein Structure by Racemic Protein Crystallography*. ProQuest LLC. Michigan.

Computing reduction potential of Glucose Oxidase Enzyme

KAZUMA TAMURA[a,b] and MUHAMAD A. MARTOPRAWIRO[a]

[a]Faculty of Mathematics and Natural Sciences, Institut Teknologi Bandung, Jl. Ganesha 10, Bandung 40132 Indonesia, E-mail: tamura@stu.kanazawa-u.ac.jp, muhamad@chem.itb.ac.id
[b]Institute of Science and Engineering, Kanazawa University, Kakuma, Kanazawa 920-1192 Japan,

Abstract. *Glucose oxidase (GOx) is an enzyme and it is an important molecule to understand the energy transfer system in our body. Flavin adenine dinucleotide (FAD) is co-enzyme and it is frequently combined with GOx. GOx helps reduction or oxidation of FAD. Redox would not happen naturally unless FAD is combined with GOx, therefore understanding the effect of electrostatic environment which is made by atoms of GOx is one of the most important factors to decide the reduction potential of GOx-FAD. In this research, we calculate some models which have different range of electrostatic environment of GOx, and examine the effect to the redox potential and compare with previous research [1]. Additionally, we propose a new scheme for calculation of Standard Hydrogen Electrode (SHE), which is employed to measure the reduction potential to the experimental definition.*

Keywords: Redox potential, GOx, FAD, SHE

1 Introduction

Oxidation-reduction reaction, which is usually called redox reaction, is the important reaction in biochemical system. For example, photosynthesis is a process to derive the energy for plants. CO_2 is reduced and H_2O is oxidized in that process to yield carbohydrates and O_2 [2]. In biological system, there are important redox reagents. The famous ones are oxygen, transition metal ions and a number of coenzymes such as Flavin adenine dinucleotide (FAD) and nicotinamide adenine dinucleotide (NAD) [1]. Coenzyme is one of the kinds of cofactor and it is an organic molecule but not a protein. It combines with protein, which is called enzyme, and assist in biochemical transformations. Glucose Oxidase (GOx, PDBIB:1CF3) is an enzyme and it is combined with FAD as a coenzyme in order to work as a catalyst. GOx-FAD is reduced to GOx-$FADH_2$ by some steps. The ring of Flavin is known as the active side of the reaction, so we calculate the reduction potential of lumichrome part of FAD with some "environment atoms".

The difference of Gibbs energy between reduced and oxidized products is observed as reduction or oxidation potential experimentally. Because the absolute redox potential of half-cell cannot be obtained experimentally, we can discuss the redox potential by relative value to some electrode such as Standard Hydrogen Electrode (SHE) or silver-silver chloride electrode. SHE, the half-cell of redox reaction of hydrogen ion and hydrogen gas, is normally used as a reference. The absolute redox potential of SHE is estimated by some researchers. The International Union of Pure and Applied Chemistry (IUPAC) recommends to use the value of 4.44 V reported by Trasatti in 1986 [3]. We can calculate the Gibbs energy for each product, therefore we are able to estimate the absolute redox potential by the change of Gibbs energy. It is impossible to compare the absolute value and relative value. To compare experimental and calculated data, the absolute value should be measured *versus* SHE. Many researchers generally employ the IUPAC recommendation value to measure it. However, there is difficulty to choose the value of absolute potential of SHE because the other researchers report different values ranging 4.05 V to 4.73V by different models [4]. It gives different results when we use

the different computational method such as calculation theory or basis sets. If we place importance on experimental results, we should consider the change of absolute potential of SHE because of choosing the computational method. Matsui and coworkers calculate the absolute reduction potential of SHE depended on calculation methods [4]. In this research we use that value to measure the reduction potentials and we also propose a new scheme to calculate reduction potential of SHE.

2 Methods and Models

The difference of Gibbs energy between before and after reaction has relation with redox potential as shown in equation (1):

$$E_0 = -\frac{\Delta G_{red}}{nF} \tag{1}$$

Where E_0 is the absolute reduction potential, ΔG_{red} is the difference of Gibbs energy between reduced and oxidized, n is the number of electrons transferred and F is the Faraday constant. We calculate the Gibbs energy for each side of reaction half-cell by DFT and 6-31+G(d) is used as the basis set. PCM is used for implicit solvent model. Generally the change of Gibbs energy by reaction in solute cannot be calculated directly because of fluctuation. Thermodynamic cycle is usually employed. In our case the calculation gives the minimum of Gibbs energy because of using PCM, therefore we can get the change of Gibbs energy directly.

GOx-FAD is reduced to GOx-$FADH_2$. This reaction process is happen step by step as shown in equation (2) to (4):

$$\mathrm{FAD} + e^- \rightarrow \mathrm{FAD}^- \tag{2}$$

$$\mathrm{FAD}^- + \mathrm{H}^+ + e^- \rightarrow \mathrm{FADH}^- \tag{3}$$

$$\mathrm{FADH}^- + \mathrm{H}^+ \rightarrow \mathrm{FADH_2} \tag{4}$$

We focus on the first step of this process shown in equation (2) and calculate the reduction potential. We make 2 models and we show them in figure 1 and 2. The model one is only lumichrome molecule which is known as the active side of the reaction [2]. This model contains only 31 atoms. It is enough small to be calculated by Quantum Mechanics. The second model is FAD molecule which has the lumichrome part and tail part. This model is little large therefore we use ONIOM method. The lumichrome part which is enclosed by circle in figure 2 is treated as QM region and the other part is MM region. QM region is treated by DFT/B3LYP 6-31+G(d). Universal Force Field, UFF, is used for MM region.

In this research, we calculate the Gibbs energy of each molecule on the half-cell for each model, and estimate the absolute value of reduction potential of GOx-FAD. The absolute potential is measured *versus* SHE to compare with experiment. We use 3 kinds of value for the absolute reduction potential of SHE, first is IUPAC recommendation value 4.44V, second is theory and basis set depend-

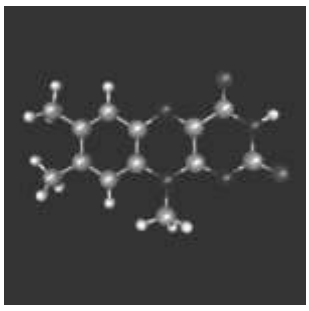

Figure.1 the structure of model 1 (lumichrome molecule model)

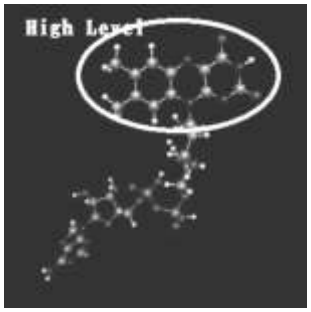

Figure.2 the structure of model 2 (FAD molecule model)

ence value 4.99V reported by Matsui and coworkers, the last one is calculated by our new scheme as mentioned below.

Experimentally SHE is the most common relative electrode. Even if silver-silver chloride electrode or the other electrode is used, the result is usually measured by SHE. The half-cell of SHE is shown in equation (5):

$$\frac{1}{2}\mathrm{H_2} \rightarrow \mathrm{H^+} + e^- \tag{5}$$

This reaction contains proton. If we were able to calculate a proton by quantum mechanics method, we can calculate the reduction potential of that half-cell. Unfortunately, a proton has no electron therefore we cannot use *ab initio* molecular orbital method. With focusing on the behavior of a proton in water solvent, we make new scheme to calculate the reduction potential of SHE. In the water solvent, a proton is not stable from the view point of free energy. Protons form oxonium ions by associating with one or more number of water molecules, like H_3O^+, H_5O^+, …, $H^+(H2O)_n$, … . We approximate half-cell of SHE by equation (6) or (7):

$$\frac{1}{2}\mathrm{H_2} + n\mathrm{H_2O} \rightarrow \mathrm{H^+(H_2O)}_n + e^- \tag{6}$$

$$\frac{1}{2}\mathrm{H_2} + (\mathrm{H_2O})_n \rightarrow \mathrm{H^+(H_2O)}_n + e^- \tag{7}$$

The difference of these two equations is the form of water molecules on the left hand side. Both of equations (6) and (7) have *n* H2O molecules. The Gibbs energy of water molecules is calculated by summation of an isolated water molecule for equation (6), on the other hand, it is defined as a cluster of *n* water molecules. To clarify this approximation, equations (6) and (7) are expressed by Gibbs Energy in equations (8) and (9):

$$\frac{1}{2}\mathrm{G_{H_2}(g)} + n\mathrm{G_{H_2O}(aq)} \rightarrow \mathrm{G_{H^+(H_2O)}}_n\mathrm{(aq)} \tag{8}$$

$$\frac{1}{2}\mathrm{G_{H_2}(g)} + \mathrm{G_{(H_2O)}}_n\mathrm{(aq)} \rightarrow \mathrm{G_{H^+(H_2O)}}_n\mathrm{(aq)} \tag{9}$$

Where $\mathrm{G_{H_2}(g)}$ is the Gibbs energy of hydrogen molecule in the gas, and $\mathrm{G_{H_2O}(aq)}$, $\mathrm{G_{H^+(H_2O)}}_n\mathrm{(aq)}$ and $\mathrm{G_{(H_2O)}}_n\mathrm{(aq)}$ are the Gibbs energy of a water molecule, oxonium ion and a cluster of n water molecules in water solvent. We estimate the absolute reduction potential of SHE from the difference of the Gibbs energy of this half-cells.

3 Results and Discussion

Reduction potential of GOx-FAD

We calculate the Gibbs energy and reduction potential. Table 1 shows the calculated results of each model. To calculate the absolute potential, *n*=1 and F=96.4853kC/mol are employed. The experimental data of this reduction potential is -0.200V [5]. We obtain the absolute potential of 3.69V by model 1. If we employ IUPAC recommendation value for SHE reduction potential 4.44V, the reduction potential is -0.748V. The model 2 gives -0.639V by the same way. The results show the model 2 gives loser value to the experimental data. A possibility reason is that the tail part of FAD molecule makes larger dipole moment on the reduced side. The dipole moments of oxidized side are 14.85 Debye and 14.30 Debye in model 1 and model 2. Those two values are almost the same but there is difference in the dipole moment of reduced side. The model 1 gives 17.41 Debye and model 2 gives 48.63 Debye. The model 2 has much larger dipole moment. Large dipole moment has effect to stabilize the molecule in the water solvent and give the lower Gibbs energy. This effect may give larger difference between reduced and oxidized species in model2. If FAD is combined with GOx, the dipole moment of the system becomes larger because of the effect of polarity residues of GOx. It may give the better result therefore we will report it in the future.

Table 1. The calculated results of GOx-FAD. The model 1 is calculated by full QM with DFT/B3LYP 6-31+G(d). ONIOM method is used for model 2. Same method with model 1 is used for high level layer of ONIOM, and UFF is used for the other mechanical part as the force field.

	G_{ox} (A)	G_{red} (B)	ΔG_{red} (B)-(A)	E_{abs}^{red}	$E_0^{red} = E_{abs}^{red} - E_0^{SHE}$	
					IUPAC[b]	Matsui[c]
Model 1	-871.975[a]	-872.110[a]	-0.135679[a]	3.69V	-0.748V	-1.30V
Model 2	-832.227[a]	-832.367[a]	-0.139667[a]	3.80V	-0.639V	-1.19V

[a] The unit is Hartree. [b] The absolute potential is measure by $E_0^{SHE} = 4.44V$ which is recommended by IUPAC [3]. [c] $E_0^{SHE} = 4.99V$, reported by Matsui *et. al.* [4], is used to measure.

In case we employ Matsui and coworkers' value of SHE to measure, the reduction potential of FAD is -1.19V by model 2. This result is 0.55 V further from the result which is measured by IUPAC recommendation. It is surely caused by the difference of SHE value. This fact indicate that the choosing of the reduction potential of SHE cause important error.

Reduction potential of SHE

Figure 1 shows the calculated results in each number of water. We calculate the reduction potential of the half-cell shown in equation (6) and (7). Model 1, the equation (6), has the minimum with n=4 and this structure is known as the most stable [6]. The potential on the minimum is 5.04V. This value is very close to Matsui and coworkers' result 4.99V for DFT/B3LYP 6-31+G(d). On the other hand, model 2 which is the calculation of equation (7) is converged in the large n and the results have the range about 4.3 to 4.4V. The minimum in model 2 is 4.31V with n=6. In the equation (7), the water molecules on the left hand side is structured. The size of cavity when we use PCM is about 1.2 times larger than van der Waals surface. The half-cell of SHE is equation (5). If we add n water molecules in equation (5), it is changed to equation (10):

$$\frac{1}{2}H_2 + n(H_2O) \rightarrow H^+ + e^- + n(H_2O) \quad (10)$$

And a proton associate with water molecules therefore equation (10) is changed to equation (11):

$$\frac{1}{2}H_2 + n(H_2O) \rightarrow H^+ + e^- + n(H_2O) \rightarrow H^+(H_2O)_n + e^- \quad (11)$$

Seeing this equation, model 1 is similar reaction to the SHE half-cell, but the model 2 leads to the better result because of the size of cavity. Here we consider the case of n=4. If we employ the model 1, the size of cavity is 4.8 times van der Waals surface. One water molecule volume of cavity with PCM is 37.6 Å^3 therefore the size of cavity of model 1 is about 150 Å^3. The cavity of model 2 is 126.6 Å^3 from the result. We find the size of cavity of model 1 is much larger than model 2. Figure 2 shows the size of cavity in each n and each model. Figure 3 shows the size of cavity per one water molecule. Calculate from the density of liquid water, one water molecule has about 30 Å^3 of volume. Now we calculate the water molecule in water solvent, so the volume should be around this value. The size of cavity per a water molecule is 29.5Å^3 with n=6 in

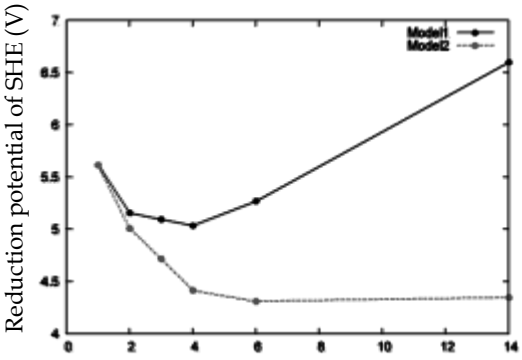

Figure 1. The number of water dependence of reduction potential of SHE. The solid line is the model 1 which is based on the equation (6). The dashed line is the model 2 which is based on the equation (7). The model 2 is converged in the large n, but model 1 has the minimum in n=4.

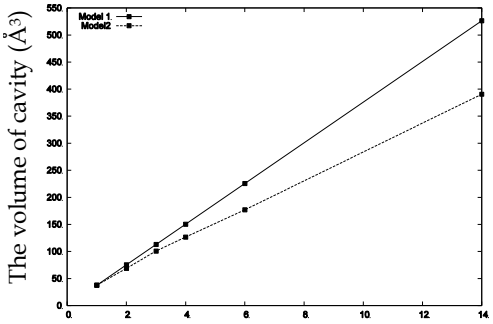

Figure 2. The volume of cavity. Model 1 is solid line and model 2 is dashed line. Model 1 has much larger cavity than model 2.

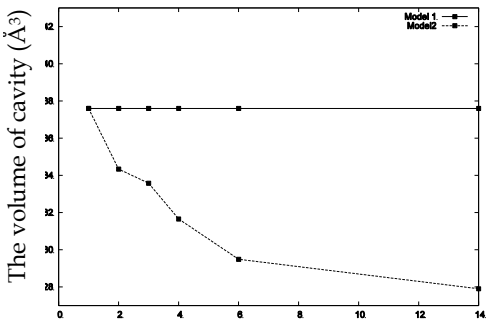

Figure 3. The volume of cavity per a water molecule. Model 1 is solid line and model 2 is dashed line.

model 2. We know n=6 in model gives the minimum and we consider this value is the suitable for reduction potential of SHE with DFT/B3LYP 6-31+G(d). this value is not o far from IUPAC recommendation value 4.44 V but little far from Matsui and coworkers' report 4.99 V. we need to calculate SHE potential with the other calculation theory or basissets and discus the correctness.

Reduction potential of GOx-FAD measured by our SHE potential

We consider the reduction potential of SHE is 4.31 V and use this value to measure the reduction potential of GOx-FAD. The result is -0.500 V by FAD model (the model 2 of GOx-FAD). The experimental data is -0.200 V, consequently our result is 0.300 V further than experimental data. In this research, we consider only FAD molecule and just ignore the effect of GOx. If we calculate with a part of GOx, it may provide closer value. Kurniawan and coworkers report the reduction potential of GOx-FAD with similar calculation method [1]. According to their study, the reduction potential of FAD is -0.801 V. Our result is little close to the experimental data. We understand that our calculation find more stable structure.

4 Conclusions

We successfully calculated the reduction potential of FAD with ONIOM method. Additionally we make a new scheme to calculate the reduction potential of SHE. We estimate 4.31 V for SHE potential. This value is close to IUPAC recommendation. We calculate the FAD reduction potential by our SHE potential and get -0.500 V. This value is close to experimental data of -0.200 V.

In the future, we plan to calculate the reduction potential of FAD with some parts of GOx. Residues of GOx around the active site of reaction have effect to the reaction. This calculation may give better results.

References

[1] I. Kurniawan, MA. Martoprawiro and H. Nagao (2013), *Indonesian Student Conference on Science and Mathematics, I*, INDONESIA.

[2] Formaneck, M. S., *et. al.*, CALCULATING ACCURATE REDOX POTENTIALS IN ENZYMES WITH A COMBINED QM/MM FREE ENERGY PERTURBATION APPROACH, *Journal of Theoretical and Computational Chemistry*, 1(1), 53, 2002.

[3] S. Trasatti (1986), The absolute electrode potential: an explanatory note, *Pure & Appl. Chem.*, **58**, (7), 955-966

[4] Toru Matsui, *et. al.*(2013), Consistent Scheme for Computing Standard Hydrogen Electrode and Redox Potentials, *Journal of Computational Chemistry*, **34**, 21-26.

[5] Marian T. Stankovich, *et. al.*(1978), Determination of Glucose Oxidase Oxidation-Reduction Potentials and the Oxygen Reactivity of Fully Reduced and Semiquinoid Forms, *The Journal of Biological Chemistry*, **253**(14), 4971-4979

[6] Song Hi Lee(2002), Molecular Dynamics Simulations of the OSS2 Model for Water and Oxonium Ion Monomers and Protonated Water Clusters, *Bull. Korean Chem. Soc.*, **23**(1), 107-111

Computation of Redox Potential of Molecule by Energy Representation Method

MASASHI IWAYAMA, KAZUTOMO KAWAGUCHI, HIROAKI SAITO, HIDEMI NAGAO

Institute of Science and Engineering, Kanazawa University, Kakuma, Kanazawa 920-1192 Japan,
E-mail: iwayama@wriron1.s.kanazawa-u.ac.jp

Abstract. *We have been applied the conventional approach based on the molecular dynamics simulation to estimate the redox potential so far. In this study, we have focused the computational conditions in order to estimate standard redox potential by using the energy representation method: we calculate excess chemical potential increasing the number of solvent molecules and sampling data for the preparation of energy distribution functions. From these results, we have found that the computational value of the standard redox potential is close to the experimental value in the case of the system with larger number of solvent molecules unaffected by the behavior of counter-ion when we take a sufficient sampling data for the energy distribution functions.*

Keywords: redox potential, molecular dynamics simulation, thermodynamics cycle, excess chemical potential, energy representation method

1 Introduction

Understanding of redox (reduction and oxidation) mechanisms with electron transfer in biological systems has borne great importance in wide-ranged areas. Analyzing the detailed value of redox potential has been key element technology to apply the redox reaction in biological system to the industrial field such as the bio-fuel cells [1] and artificial photosynthesis [2] as well as the interest in biology [3]. In order to estimate the value of redox potential of molecules, several computational models and methods base on the quantum mechanics (QM) [4, 5] and QM/molecular mechanics (MM) hybrid methods [6, 7] has been developed with the recently growth of computer architecture. However, it is not easy to estimate the redox potential because the redox reaction is associated with the free energy change in electron transfer process in the condensed system, much less the computation of redox potential of large molecules including proteins due to the computational cost. The development of theoretical models and methods to estimate the redox potential for the biological systems is still challenging topics in the field of computational science.

In the previous report, we have suggested a simple calculation method by using molecular dynamics (MD) and density functional theory (DFT) calculations according to thermodynamic cycle to estimate the redox potential of molecules, and we have showed the efficiency of our conventional approach to estimate the difference of the standard redox potential of molecules relative to the normal hydrogen electrode (NHE) potential, which mean the difference of the absolute redox potential of molecules, comparing with the experimental data [8]. However, in the view of each molecule's standard redox potential, the computational values have large discrepancies comparing with the experimental values. To compute accurate value of standard redox potential should be important for the understanding of molecular-specific redox mechanism and the exactly discussions of the redox potential with the difference of that of molecules.

In this study, we compute the standard redox potential of simple small molecule, acetone, relative to the NHE potential. Then, in order to investigate the proper conditions to get more accurate value of standard redox potential, we improve the computational method of excess chemical potential, which is required to estimate the absolute oxidation free energy in thermodynamic cycle, in

the frame work of the energy representation (ER) method [9, 10]: specifically, we calculate the dependence of the standard redox potential on the number of solvent molecules in the simulation cell, and we evaluate the excess chemical potential increasing the sampling data for the description of the energy distribution function. From these results, we have discussed the computational approach by using the ER method to estimate the standard redox potential of molecule.

2 Computational procedures

The computation of the standard redox potential of molecule employs the Nernst equation. The standard redox potential E° is associated with the absolute oxidation free energy change, ΔG, and the absolute potential of normal hydrogen electrode (NHE), E^{NHE}, which has -4.44 V for the experimental data [8, 11], as follow,

$$E^{\circ} = \frac{\Delta G}{nF} + E^{NHE}, \tag{1}$$

where, n and F are the number of electrons and the Faraday constant, respectively. According to the thermodynamic cycle as shown in Figure 1, the ΔG is given by

$$\Delta G = \Delta E + \left\{ \Delta\mu_{(N-1)} - \Delta\mu_{(N)} \right\}, \tag{2}$$

where, ΔE is the ionization free energy, $\Delta\mu_{(N)}$ and $\Delta\mu_{(N\text{-}1)}$ are excess chemical potential of molecules in reduced and oxidized states, respectively. The ionization free energy is evaluated by the difference of the average of total energies of reduced and oxidized configurations, which are obtained from the molecular dynamics (MD) simulations of the molecules in solvation. The excess chemical potential is calculated by the energy representation (ER) method by utilizing the energy representation module (ERmod) program packages [12]. In the ER method, the excess chemical potential is given by the energy distribution functions for the solution and reference solvent systems. These energy distribution functions are obtained from the different MD simulations. The actual form of the excess chemical potential using these energy distribution functions and the details of computational methodology are presented in Refs. [9, 10].

In this report, we have used the previous result of equilibrium MD simulations for the configurations of the neutral and radical cationic molecule in solvation, and we also have used the values of ionization free energy ΔE, which is obtained by the density functional theory (DFT) calculations with B3LYP method and 6-31+G(d,p) basis set in the previous study [8]. The excess chemical potentials in the neutral and radical cationic states, $\Delta\mu_{(N)}$ and $\Delta\mu_{(N\text{-}1)}$, have been reevaluated

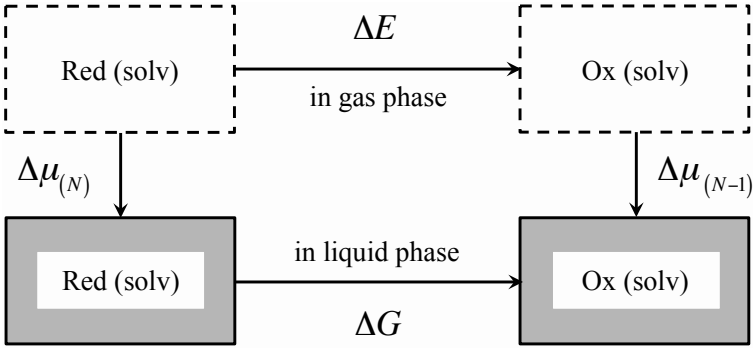

Figure 1. Conventional approach to calculate the absolute oxidation free energy change ΔG based on the thermodynamic cycle

relative to the different number of solvents system. In this study, we prepare the simulation boxes including 1425, 2850 and 4275 solvents molecules; then these system sizes are 36.5 × 34.3 × 34.6 Å, 45.7 × 43.4 × 43.9 Å and 52.3 × 50.0 × 50.0 Å, respectively. The MD simulation for the calculation of energy distribution function is performed utilizing the AMBER 11 program packages [13]. Langevin thermostat and barostat are used to control system temperature (T = 300 K) and pressure (P = 1 atm). The TIP3P model [14] is adopted for the solvent molecule. Particle mesh Ewald method [15] is used for the calculation of coulomb interaction. Cut-off lengths for the real-space coulomb and van der Waals (vdW) interactions are 12 Å. The time step for the MD simulation is 2 fs. The AMBER force field 03 (parm99) parameters [16, 17] are used for the vdW and torsion interactions of solute molecules. On the other hands, for the bond stretching, angle bending and partial charge in acetone molecule, we have applied the previous results obtained from the quantum chemical calculations [18]. It is noted that for the MD simulations of the radical cationic acetone under the periodic boundary conditions, a chloride-ion is inserted into the simulation cell as counter-ion.

For the calculation of energy distribution function for the solution system, the sampled structure of the solute molecule obtained from the equilibrium MD simulation is put in the center of the MD cell, and the water molecules are arranged around the solute molecule. The *NPT*-MD simulation of the solution system is performed for 1 ns to prepare total 100 × 10^3 snapshots. The configuration of the solute molecule is fixed in this simulation. On the other hands, for the calculation of energy distribution function for the reference solvent system, the pure solvent system, which has the same number of water molecules as the solution system, is prepared. The *NPT*-MD simulation of the reference solvent system is performed for 100ps to obtain 100 snapshots. After that, the sampled structures are randomly inserted 1000 times into the pure solvent system of each snapshot: a total of 100 × 10^3 sampling data are prepared for the reference solvent system. It is noted that we have confirmed that the number of sampling data for the reference solvent system is sufficient to estimate the excess chemical potential of molecule in the neutral and radical cationic states.

3 Results and discussions

Table 1 show the computational results of the dependence of absolute oxidation free energy ΔG and the standard redox potential E° of an acetone on the number of solvent molecules in the simulation cell. The average values of ΔG or E° are 186.7, 187.6 and 188.5 kcal/mol or the 3.65, 3.69 and 3.73 V for the 1425, 2850 and 4275 solvents systems, respectively. These results show that the computational value of standard redox potential is more different from the experimental value (0.16 V [19]) even if the number of solvent molecules increases in the simulation cell. The average values of excess chemical potential in neutral state, $\Delta\mu_{(N)}$, are -2.3 kcal/mol for all of the solvents systems, showing that there is no dependence of the $\Delta\mu_{(N)}$ on the number of solvent molecules. On the other hands, the

Table 1. Dependence of the absolute oxidation free energy ΔG and the standard redox potential E° on the number of solvent molecules, N^{water}. The units are kcal/mol for ionization free energy ΔE, excess chemical potential in neutral and radical cationic molecules, $\Delta\mu_{(N)}$ and $\Delta\mu_{(N+1)}$, ΔG and V for the E°, respectively. The values in parentheses show the standard deviation.

N^{water}	ΔE [a]	$\Delta\mu_{(N)}$	$\Delta\mu_{(N-1)}$	ΔG	E°
1425	220.8 (1.4)	-2.3 (0.2)	-36.4 (1.5)	186.7 (2.1)	3.65 (0.09)
2850		-2.3 (0.2)	-35.5 (1.4)	187.6 (2.0)	3.69 (0.09)
4275		-2.3 (0.2)	-34.6 (2.4)	188.5 (2.8)	3.73 (0.12)

[a] Previous computational result from Refs. [8]

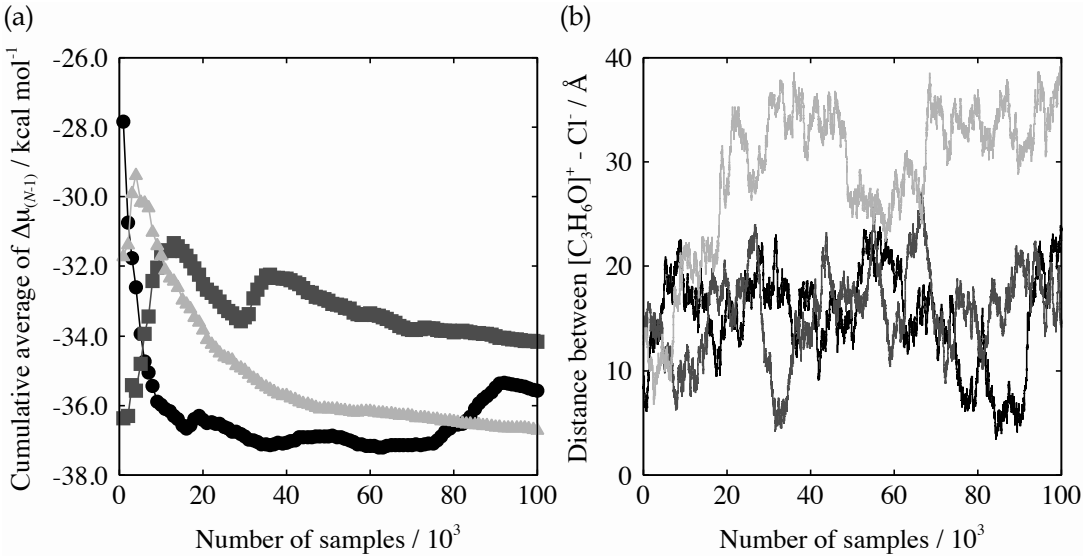

Figure 2. (a) Cumulative average of excess chemical potential in radical cationic state $\Delta\mu_{(N+1)}$ for one configuration and (b) change of distance between the radical cationic acetone and chloride-ion as a function of the number of samples; black, black ash and gray lines indicate these for the 1425, 2850 and 4275 solvents systems, respectively.

average values of excess chemical potential in radical cationic state, $\Delta\mu_{(N-1)}$, are -36.4, -35.6 and -34.6 kcal/mol for the 1425, 2850 and 4275 solvents systems, respectively, denoting the same tendency of the computational values of ΔG or E°. This results show that the radical cationic acetone is less soluble in larger solvents system.

In order to investigate the reason of this results, we have analyzed the cumulative average of $\Delta\mu_{(N-1)}$, as shown in Figure 2 (a), for just only a configuration of solute molecule, which is pick up from equilibrium molecular dynamics (MD) simulation for 10 ns. Additionally, we here plot change of distance of counter-ion (chloride-ion) from the center of mass of the solute molecule in Figure 2 (b). Comparing the Figure 2 (a) with (b), we find that the $\Delta\mu_{(N-1)}$ become positively large value when the counter-ion exists within the distance about 15 Å around the solute molecule; for instance, in the Figure 2 (a), the cumulative average of $\Delta\mu_{(N-1)}$ for the 1425 solvents system increase positively from about 75 × 10^3th sampling data, then, the distance between solute molecule and counter-ion become short as shown in Figure 2 (b). From this result, we assume that the behavior of the counter-ion artificially put in the simulation cell has a negative effect on the evaluation of the excess chemical potential of charged solute molecule.

Based on this assumption, we focus on one configuration and compute the $\Delta\mu_{(N-1)}$ increasing the number of sampling data until 1000 × 10^3 snapshots for the calculation of energy distribution function. Figure 3 (a) and (b) shows the probability distribution of the distance between the solute molecule and the counter-ion for the 100 × 10^3 and 1000 × 10^3, respectively. These figures indicate that we can estimate the $\Delta\mu_{(N-1)}$ with widely coordinate sampling of the counter-ion in the simulation cell because we can get distortion-free probability distribution between 0 – 15 Å at some level.

The results of the value of $\Delta\mu_{(N-1)}$ are shown in Figure 4. In this Figure, we plot the average of the difference of $\Delta\mu_{(N-1)}$ ($\Delta(\Delta\mu_{(N-1)})$) for 1425 solvents system from that for 2850 or 4250 solvents systems. In the case of 2850 – 1425 solvents systems, the average of $\Delta(\Delta\mu_{(N-1)})$ become negative value from outside of 400 × 10^3th sampling data. From the result, we find that the value of $\Delta\mu_{(N-1)}$ for 2850 solvents system is smaller than that for 1425 solvents system, and specifically, the value of absolute oxidation free

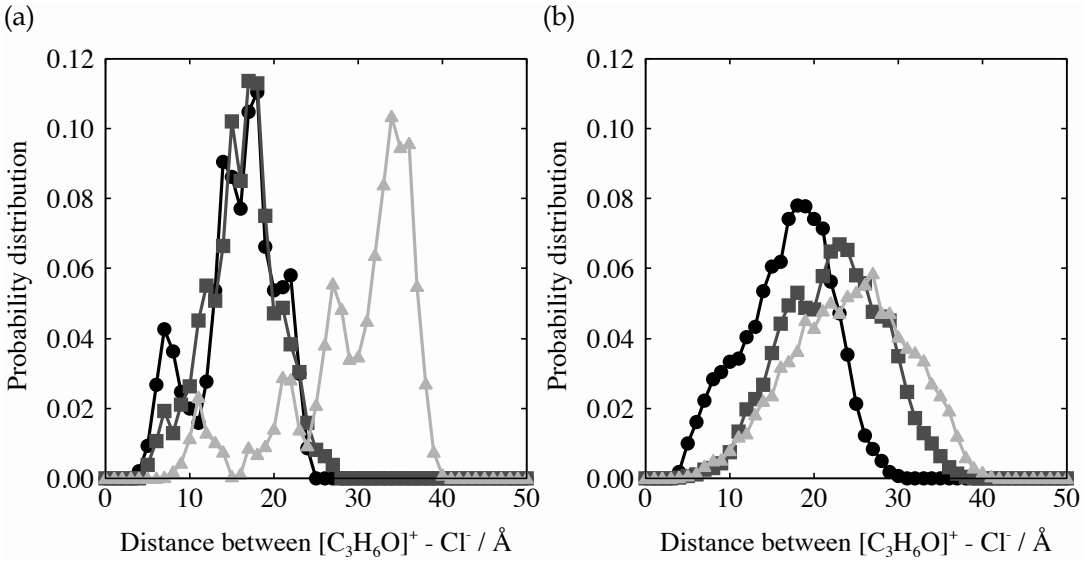

Figure 3. (a) and (b) are probability distributions of the distance between the radical cationic acetone and chloride-ion for the 100 × 10^3 and 1000 × 10^3, respectively; black, black ash and gray lines indicate these for the 1425, 2850 and 4275 solvents systems, respectively.

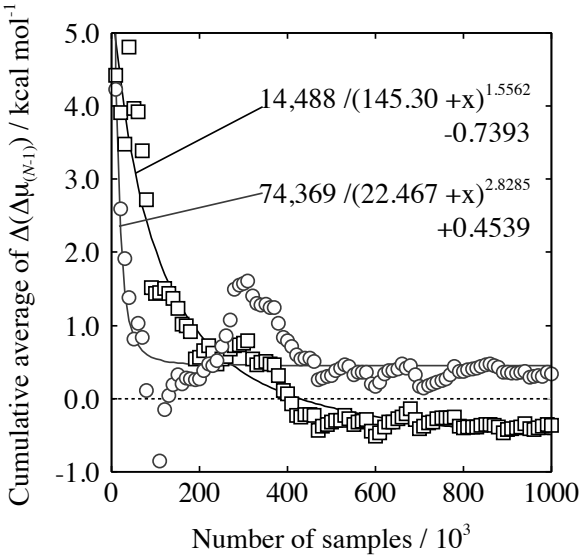

Figure 4. Cumulative average of the difference of excess chemical potential in radical cationic state $\Delta\mu_{(N-1)}$, which is showed as ($\Delta(\Delta\mu_{(N-1)})$) in the Figure, between the 1425 and 2850 solvents systems (black square points) and between the 1425 and 4250 solvents systems (black ash circle points); lines are fitting results of these points.

energy ΔG (or also standard redox potential E°) is close to the experimental value for 0.7 kcal/mol. This value is obtained from fitting calculation of all the values of $\Delta(\Delta\mu_{(N-1)})$. On the other hands, in the case of 4275 – 1425 solvents systems, the average of $\Delta(\Delta\mu_{(N-1)})$ is still positive value even if we have

take the 1000×10^3 sampling data. From the result, it is considered that the computation of $\Delta\mu_{(N\text{-}1)}$ for the 4275 solvents system is still not satisfied only by 1000×10^3 sampling data due to the widely system size; actually, the probability distribution for 4275 solvents system has larger part than that for 2850 solvents system between the distances from 0 to 15 Å. In order to become negative value for the $\Delta(\Delta\mu_{(N\text{-}1)})$ and close to the experimental data for the ΔG, we should sufficiently take sampling data for the calculation of energy distribution function, and we should compute the average of $\Delta\mu_{(N\text{-}1)}$ including the other configurations; these treatments would be a future work. Thus, these results suggest that the computational approach by using the energy representation (ER) method has the possibility of discussion for the standard redox potential of molecule under the condition of the sufficiently number of solvent molecules and sampling data to obtain the energy distribution function unaffected by the counter-ion.

4 Summary

We have computed the standard redox potential of molecule by using our conventional approach with energy representation (ER) method. To compute the absolute oxidation free energy, we have investigated the proper conditions for the calculation of excess chemical potential increasing the number of solvent molecules and sampling data to get the energy distribution functions in the frame work of the ER method.

We have discussed about the computational approach by using the ER method to estimate the standard redox potential of molecule in relation to the behavior of counter-ion in the simulation cell. The computational value of the standard redox potential is close to the experimental value in the case of larger system when we take a sufficient sampling data for the calculation of the energy distribution functions. These results suggest that the computational approach by using the ER method has the possibility of discussion for the standard redox potential of molecule under the condition of the sufficiently number of solvent molecules in the simulation cell and sampling data to obtain the energy distribution functions unaffected by the counter-ion.

References

[1] S. C. Barton, J. Gallaway, P. Atanassov (2004), Enzymatic Biofuel Cells for Implantable and Microscale Devices, *Chem. Rev.*, **104**, 4867 – 4886.

[2] Y. Umena, K. Kawakami, J. R. Shen, N. Kamiya (2011), Crystal structure of oxygen-evolving photosystem II at a resolution of 1.9 Å, *Nature*, **473**, 55 – 61.

[3] H. Lodish, A. Berk, C. A. Kaiser, M. Krieger, M. P. Scott, A. Bretscher, H. Ploegh, P. Matsudaria (2007), *Molecular Cell Biology, 6th ed.*, W. H. Freeman and Co. Ltd., New York.

[4] M. H. Baik and R. A. Friesner (2002), Computing Redox Potentials in Solution: Density Functional Theory as A Tool for Rational Design of Redox Agents, *J. Phys. Chem. A*, **106**, 7407 – 7412.

[5] Y. Fu, L. Liu, H. Z. Yu, Y. M. Wang, Q. X. Guo (2005), Quantum-Chemical Predictions of Absolute Standard Redox Potentials of Diverse Organic Molecules and Free Radicals in Acetonitrile, *J. Am. Chem. Soc.*, **127**, 7227 – 7234.

[6] H. Takahashi, H. Ohno, R. Kishi, M. Nakano, N. Matubayasi (2008), Computation of the free energy change associated with one-electron reduction of coenzyme immersed in water: A novel approach within the framework of the quantum mechanical/molecular mechanical method combined with the theory of energy representation, *J. Chem. Phys.*, **129**, 205103.

[7] X. Zeng, H. Hu, X. Hu, A. J. Cohen, W. Yang (2008), *Ab initio* quantum mechanical/molecular mechanical simulation of electron transfer process: Fractional electron approach, *J. Chem. Phys.*, **128**, 124510.

[8] M. Iwayama, I. Kurniawan, K. Kawaguchi, H. Saito, H. Nagao, A hybrid type approach with MD and DFT calculations for estimation of redox potential of molecules, *Mol. Simul.*, in press (DOI: 10.1080/08927022.2015.1012641).

[9] N. Matubayasi and M. Nakahara (2000), Theory of solutions in the energetic representation. I. Formulation, *J. Chem. Phys.*, **113**, 6070 – 6081.

[10] N. Matubayasi and M. Nakahara (2002), Theory of solutions in the energy representation. II. Functional for the chemical potential, *J. Chem. Phys.*, **117**, 3605 – 3616.

[11] S. Trasatti (1986), The absolute electrode potential: an explanatory note, *Pure and Appl. Chem.*, **58**, 955 – 966.

[12] Available from: http://sourceforge.net/projects/ermod/.

[13] D. A. Case, T. A. Darden, T. E. Cheatham, III, C. L. Simmerling, J. Wang, R. E. Duke, R. Luo, R. C. Walker, W. Zhang, K. M. Merz, B. Roberts, B. Wang, S. Hayik, A. Roitberg, G. Seabra, I. Kolossváry, K. F. Wong, F. Paesani, J. Vanicek, J. Liu, X. Wu, S. R. Brozell, T. Steinbrecher, H. Gohlke, Q. Cai, X. Ye, J. Wang, M.-J. Hsieh, G. Cui, D. R. Roe, D. H. Mathews, M. G. Seetin, C. Sagui, V. Babin, T. Luchko, S. Gusarov, A. Kovalenko, and P. A. Kollman (2010), AMBER 11, University of California, San Francisco.

[14] W. L. Jorgensen, J. Chandrasekhar, J. D. Madura, R. W. Impey, K. L. Klein (1983), Comparison of simple potential functions for simulating liquid water, *J. Chem. Phys.*, **79**, 926 – 935.

[15] T. Darden, D. York, L. Pedersen (1993), Particle mesh Ewald: an $N \cdot \log(N)$ method for Ewald sums in large systems, *J. Chem. Phys.*, **98**, 10089 – 10092.

[16] S. J. Weiner and P. A. Kollman (1986), An all atom force field for simulations of proteins and nucleic acids, *J. Comput. Chem.*, **7**, 230 – 252.

[17] Y. Duan, C. Wu, S. Chowdhury, M. C. Lee, G. Zhang, W. Xiong, R. Yang, P. Cieplak, R. Luo, T. Lee, J. Caldwell, J. Wang, P. Kollman (2003), A Point Charge Force Field for Molecular Mechanics Simulations of Proteins Based on Condensed-Phase Quantum Mechanical Calculations, *J. Comput. Chem.*, **24**, 1999 – 2012.

[18] M. Iwayama, K. Kawaguchi, H. Saito, H. Nagao (2013), Structure and hydration free energy of ketone compound in neutral and cationic state by molecular dynamics simulation, *Recent Development in Computational Science*, **4**, 59 – 69.

[19] R. H. Baker and H. Adkins (1940), Oxidation Potential of Ketones and Aldehyde, *J. Am. Chem. Soc.*, **62**, 3305 – 3314.

International Symposium on Computational Science 2015

Date: February 17, 2015 – February 18, 2015

Venue: Kanazawa University, Kakuma, Kanazawa 920-1192, Japan
Incubation Laboratory

Organized by:

Faculty of Mathematics and Physics,
Kanazawa University

Faculty of Mathematics and Natural Sciences,
Bandung Institute of Technology

Supported by:

Computational Material Science Initiative (CMSI)

Home page: http://iscs.w3.kanazawa-u.ac.jp/

Program:

Oral sessions: 17th 9:30 – 12:30, 18th 9:00 – 10:30, 18th 15:00 – 16:30

DDP sessions: 17th 13:30 – 17:45

Special session: 18th 13:30 – 14:45

Poster session: 18th 10:30 – 12:00

Organizing Committee:

Kanazawa University: F. Ishii, H. Iwasaki, K. Kawaguchi, M. Kimura, S. Miura, H. Nagao (Chair), T. Oda, S. Omata, H. Saito, M. Saito, K. Svadlenka

Bandung Institute of Technology: Acep Purqon, Finny Oktariani, Triati Dewi Kencana Wungu

Chulalongkorn University: Khamron Mekchay

International Advisory Board:

E. T. Baskoro (Bandung), M. A. Martoprawiro (Bandung), Suprijadi (Bandung), M. Saito (Kanazawa)

Symposium Program

February 17 (Tuesday)

Morning session 1 — Chair: Mineo Saito

9:30-10:00 **Hakim L. Malasan** (Bandung Institute of Technology)
South-East Asia Astronomy Network on High Performance Computing and Data Analysis

10:00-10:30 **Tatsuki Oda** (Kanazawa University)
Implementation of first-principles logarithmic mean force dynamics and strategy to the high performance computing

Coffee break

Morning session 2 — Chair: Fumiyuki Ishii

10:50-11:10 **Masashi Iwayama** (Kanazawa University)
Computation of redox potential of molecules by energy representation method

11:10-11:30 **Moh Adhib Ulil Absor** (Kanazawa University)
Persistent spin helix on ZnO (10-10) surface: First-principles study

11:30-11:50 **Sholihun** (Kanazawa University)
Density-functional-theory Calculations of the Germanium Multivacancies

11:50-12:10 **Masao Obata** (Kanazawa University)
Non-empirical Study on Oxygen Molecular and Crystal Systems Using Van der Waals Density Functional Approach

12:10-12:30 **Daiki Yoshikawa** (Kanazawa University)
Structural and electronic properties and electric field variations of magnetic anisotropy in Fe/MgO interface

Lunch break

DDP session 1

13:30–13:45 **Weerasak Dee-Am** (Kanazawa University, CU, Chair: Seiro Omata)
Simulation of the motion of a droplet on a plane by the discrete Morse flow

13:45-14:00 **Ullul Azmy** (Kanazawa University, ITB, Chair: Seiro Omata)
Simulation of a Rising Oil Droplet using an Interface-Fluid Coupling

14:00-14:15 **Herlan Setiadi** (Kanazawa University, ITB, Chair: Seiro Omata)

A Particle Based Solver for the Three Dimensional Fluid Flow through an Elastic Porous Medium

14:15-14:30 **Pornchanit Supvilai** (Kanazawa University, CU, Chair: Seiro Omata)

Simulation of A Soap Film Catenoid

14:30-14:45 **Reza Fahrul Arifin** (Kanazawa University, ITB, Chair: Seiro Omata)

Triple Junction Simulation using the Acceleration Dependent BMO method

Coffee break

DDP session 2

15:00-15:15 **Armanda Ikhsan** (Kanazawa University, ITB, Chair: Masato Kimura)

Finite Element Simulation of Crack Propagation- Exact Solution and Phase Field Model

15:15-15:30 **Maharan**i **Ahsani Ummi** (Kanazawa University, ITB, Chair: Masato Kimura)

Shape Optimization Approach to an Inverse Free Boundary Problem

15:30-15:45 **Iryanto** (Kanazawa University, ITB, Chair: Karel Svadlenka)

Shallow Water - Navier-Stokes Coupling Method in Ocean Wave Simulation

15:45-16:00 **Fuad Yasin** (Kanazawa University, ITB, Chair: Kenichi Kawagoe)

Non-vanishing Terms of the Jones Polynomial

16:00-16:15 **Prihardono Ariyanto** (Kanazawa University, ITB, Chair: Kenichi Kawagoe)

The 5-Puzzle and 8-Puzzle with the Neighbors Swap Motion

Coffee break

DDP session 3

16:30-16:45 **Muhammad Zaki Almuzakki** (Kanazawa University, ITB, Chair: Katsuyoshi Ohara)

Computing general error locator polynomials of 3-error-correcting BCH codes via syndrome varieties using minimal polynomials

16:45-17:00 **Dinan Andiwijayakusuma** (Kanazawa University, ITB, Chair: Mineo Saito)

First Principle Study of Hydrogen Impurity in GaN

17:00-17:15 **Muhammad Rifqi Al Fauzan** (Kanazawa University, ITB, Chair: Mineo Saito)

Multiferroic BiFeO3 for Photovoltaics Application : A First Principle Study

17:15-17:30	**Sri Rahayu Natasia** (Kanazawa University, ITB, Chair: Hidemi Nagao) *Prediction of Solvation Free Energy of Proteins: Molecular Dynamics Simulation and QSPR Model Approach*
17:30-17:45	**Kazuma Tamura** (ITB, Kanazawa University, Chair: Muhamad A. Martoprawiro) *Computing reduction potential of Glucose Oxidase enzyme*
18:30-	Banquet at University Canteen ("Minami-Fukuri Frepo")

February 18 (Wednesday)

Morning session — Chair: Karel Svadlenka

9:00-9:30 **Petr Pauš[1), 2)], Michal Beneš[1)], and Jan Kratochvíl[1)]** (Czech Technical University in Prague[1)], Meiji University[2)])

Numerical simulation of dislocation cross-slip in non-symmetric configurations

9:30-10:00 **Krung Sinapiromsaran** (Chulalongkorn University)

Simplex improvement without artificial variables

10:00-10:30 **Muhamad A. Martoprawiro** (Bandung Institute of Technology)

Computational study of structure and stability of $[Fe_n(L_1)_p(L_2)_q]^{x+}$ *and* $[Fe_n(L_1)_r]^{y+}$ *polymeric complexes with n = 2, 4, and 6,* L_1 *= 1,2,4-4H-triazole,* L_2 *= 1,2,4-triazolato, p = 4, 8, and 12, q = 2, 4, and 6, r = 6, 12, and 18, x = 2, 4, 6, and y = 4, 8, 12*

Poster session / Business meeting

10:30-12:00 See below for poster session program

12:00 Group Photo

Lunch break

Special session — **Universities Introduction for Studying Abroad** Chair: Masato Kimura

This is a special session for Japanese students in Kanazawa University to study abroad. Some universities with which Faculty of Mathematics and Physics, Kanazawa University has (or is planning to have) student exchange programs are introduced. This session is performed in Japanese and English.

13:30-13:40 **Masato Kimura** (Kanazawa University)

An encouragement of studying abroad

13:40-13:50 **Muhamad A. Martoprawiro** (Bandung Institute of Technology)

Introduction of Bandung Institute of Technology (Bandung, Indonesia)

13:50-14:00 **Krung Sinapiromsaran** (Chulalongkorn University)

Introduction of Chulalongkorn University (Bangkok, Thailand)

14:00-14:10 Question time

14:10-14:20 **Koichi Matsumoto** (Kanazawa University)

Introduction of Kazan Federal University (Kazan, Russia)

14:20-14:30 **Masato Kimura** (Kanazawa University)

Introduction of Eindhoven University of Technology (Eindhoven, Netherlands)

14:30-14:40	**Petr Pauš** (Czech Technical University, Meiji University)
	Introduction of Czech Technical University (Prague, Czech Republic)
14:40-14:45	Question time

Coffee break

Afternoon session	Chair: Shinichi Miura
15:00-15:30	**Tsutomu Kawatsu** (The University of Tokyo, Yokohama City University)
	Application of Ab initio Path Integral Molecular Dynamics to Molecular Systems
15:30-16:00	**Takashi Uneyama** (Kanazawa University)
	Modelling and Simulations of Polymeric Systems under Static and Dynamic Constraints
16:00-16:30	**Tomoaki Niiyama** (Kanazawa University)
	The molecular dynamics study on non-equilibrium critical behaviors in crystalline plasticity

Poster session (10:30 – 12:00 February 18)

1. **Weerasak Dee-Am** (Kanazawa University, CU)

Simulation of the motion of a droplet on a plane by the discrete Morse flow

2. **Ullul Azmy** (Kanazawa University, ITB)

Simulation of a Rising Oil Droplet using an Interface-Fluid Coupling

3. **Herlan Setiadi** (Kanazawa University, ITB)

A Particle Based Solver for the Three Dimensional Fluid Flow through an Elastic Porous Medium

4. **Pornchanit Supvilai** (Kanazawa University, CU)

Simulation of A Soap Film Catenoid

5. **Reza Fahrul Arifin** (Kanazawa University, ITB)

Triple Junction Simulation using the Acceleration Dependent BMO method

6. **Armanda Ikhsan** (Kanazawa University, ITB)

Finite Element Simulation of Crack Propagation- Exact Solution and Phase Field Model

7. **Maharani Ahsani Ummi** (Kanazawa University, ITB)

Shape Optimization Approach to an Inverse Free Boundary Problem

8. **Iryanto** (Kanazawa University, ITB)

Shallow Water - Navier-Stokes Coupling Method in Ocean Wave Simulation

9. **Fuad Yasin** (Kanazawa University, ITB)

Non-vanishing Terms of the Jones Polynomial

10. **Prihardono Ariyanto** (Kanazawa University, ITB)

The 5-Puzzle and 8-Puzzle with the Neighbors Swap Motion

11. **Muhammad Zaki Almuzakki** (Kanazawa University, ITB)

Computing general error locator polynomials of 3-error-correcting BCH codes via syndrome varieties using minimal polynomials

12. **Dinan Andiwijayakusuma** (Kanazawa University, ITB)

First Principle Study of Hydrogen Impurity in GaN

13. **Muhammad Rifqi Al Fauzan** (Kanazawa University, ITB)

Multiferroic BiFeO3 for Photovoltaics Application : A First Principle Study

14. **Sri Rahayu Natasia** (Kanazawa University, ITB)

Prediction of Solvation Free Energy of Proteins: Molecular Dynamics Simulation and QSPR Model Approach

15. **Kazuma Tamura** (ITB, Kanazawa University)

Computing reduction potential of Glucose Oxidase enzyme

16. **Takahiro Ito** (Kanazawa University)

Analysis of numerical oscillation of Crank-Nicolson method for the heat equation

17. **Takayuki Noda** (Kanazawa University)

Wave simulation using Navier-Stokes Equation and Shallow Water Equation Models

18. **Daiki Yoshikawa** (Kanazawa University)

Structural and electronic properties and electric field variations of magnetic anisotropy in Fe/MgO interface

List of participants

Seiro Omata	Kanazawa University
	omata@se.kanazawa-u.ac.jp
Masato Kimura	Kanazawa University
	mkimura@se.kanazawa-u.ac.jp
Manabu Oura	Kanazawa University
	oura@se.kanazawa-u.ac.jp
Osamu Ogurisu	Kanazawa University
	ogurisu@staff.kanazawa-u.ac.jp
Karel Svadlenka	Kyoto University
	karel@math.kyoto-u.ac.jp
Katsuyoshi Ohara	Kanazawa University
	ohara@se.kanazawa-u.ac.jp
Norbert Pozar	Kanazawa University
	npozar@se.kanazawa-u.ac.jp
Mineo Saito	Kanazawa University
	m-saito@cphys.s.kanazawa-u.ac.jp
Hidemi Nagao	Kanazawa University
	nagao@wriron1.s.kanazawa-u.ac.jp
Tatsuki Oda	Kanazawa University
	oda@cphys.s.kanazawa-u.ac.jp
Shinichi Miura	Kanazawa University
	smiura@mail.kanazawa-u.ac.jp
Hiroshi Iwasaki	Kanazawa University
	iwasaki@cs.s.kanazawa-u.ac.jp
Fumiyuki Ishii	Kanazawa University
	ishii@cphys.s.kanazawa-u.ac.jp
Hiroaki Saito	Kanazawa University
	saito@wriron1.s.kanazawa-u.ac.jp
Kazutomo Kawaguchi	Kanazawa University
	kkawa@wriron1.s.kanazawa-u.ac.jp
Hakim L. Malasan	Bandung Institute of Technology
	hakim@as.itb.ac.id

Muhamad A. Martoprawiro	Bandung Institute of Technology muhamad@chem.itb.ac.id
Masashi Iwayama	Kanazawa University iwayama@wriron1.s.kanazawa-u.ac.jp
Moh Adhib Ulil Absor	Kanazawa University adhib@cphys.s.kanazawa-u.ac.jp
Sholihun	Kanazawa University sholihun@cphys.s.kanazawa-u.ac.jp
Masao Obata	Kanazawa University obata@cphys.s.kanazawa-u.ac.jp
Daiki Yoshikawa	Kanazawa University yoshikawa@cphys.s.kanazawa-u.ac.jp
Petr Pauš	Czech Technical University in Prague prasatko55@gmail.com
Krung Sinapiromsaran	Chulalongkorn University krung.s@gmail.com
Tsutomu Kawatsu	The University of Tokyo, Yokohama City University kawatsu@fukui.kyoto-u.ac.jp
Takashi Uneyama	Kanazawa University uneyama@se.kanazawa-u.ac.jp
Tomoaki Niiyama	Kanazawa University niyama@se.kanazawa-u.ac.jp
Takahiro Ito	Kanazawa University ituuuti@gmail.com
Takayuki Noda	Kanazawa University t.noda1031@gmail.com
* Weerasak Dee-Am	Kanazawa University, Chulalongkorn University uueerasak@gmail.com
* Ullul Azmy	Kanazawa University, Bandung Institute of Technology ullul.azmy@hotmail.com
* Herlan Setiadi	Kanazawa University, Bandung Institute of Technology hsd.the.explorer@gmail.com
* Pornchanit Supvilai	Kanazawa University, Chulalongkorn University hippoarale@gmail.com

* Reza Fahrul Arifin Kanazawa University, Bandung Institute of Technology
mxt.reza@gmail.com
* Armanda Ikhsan Kanazawa University, Bandung Institute of Technology
armandaikhsan@gmail.com
* Maharani Ahsani Ummi Kanazawa University, Bandung Institute of Technology
maharaniahsani@gmail.com
* Iryanto Kanazawa University, Bandung Institute of Technology
iryanto.math@yahoo.com
* Fuad Yasin Kanazawa University, Bandung Institute of Technology
yasin.fuad@hotmail.com
* Prihardono Ariyanto Kanazawa University, Bandung Institute of Technology
prihardono@gmail.com
* Muhammad Zaki Almuzakki Kanazawa University, Bandung Institute of Technology
muhammad.almuzakki@gmail.com
* Dinan Andiwijayakusuma Kanazawa University, Bandung Institute of Technology
dandiwijaya@gmail.com
* Muhammad Rifqi Al Fauzan Kanazawa University, Bandung Institute of Technology
alfauzan.rifqi@gmail.com
* Sri Rahayu Natasia Kanazawa University, Bandung Institute of Technology
ayu@wriron1.s.kanazawa-u.ac.jp
* Kazuma Tamura Bandung Institute of Technology, Kanazawa University
tamura@wriron1.s.kanazawa-u.ac.jp

* This Double-Degree program is an educational program based on the agreement of cooperation between Kanazawa University and Bandung Institute of Technology and between Kanazawa University and Chulalongkorn University. Therefore, the affiliation of students participating in this program is as follows:

Graduate School of Natural Science and Technology, Kanazawa University, Japan &
Faculty of Mathematics and Natural Sciences, Bandung Instituted of Technology, Indonesia
or
Graduate School of Natural Science and Technology, Kanazawa University, Japan &
Department of Mathematics and Computer Science, Faculty of Science, Chulalongkorn University, Thailand